ANALYSIS AND APPLICATIONS OF MELT EXPULSION DURING ULTRASONIC VIBRATION-ASSISTED LASER SURFACE PROCESSING

By

SEYYED HABIB ALAVI

Bachelor of Science in Materials Science and Engineering
Imam Khomeini International University
Qazvin, Iran
2006

Master of Science in Materials Engineering and Metallurgy
University of Tehran
Tehran, Iran
2009

Submitted to the Faculty of the
Graduate College of
Oklahoma State University
in partial fulfillment of
the requirements for
the Degree of
DOCTOR OF PHILOSOPHY
May, 2018

ANALYSIS AND APPLICATIONS OF MELT EXPULSION DURING ULTRASONIC VIBRATION-ASSISTED LASER SURFACE PROCESSING

Committee Members:

Dr. Sandip P. Harimkar

Dissertation Advisor

Dr. A. Kaan Kalkan

Dr. James M. Manimala

Dr. Ranji Vaidyanathan

ACKNOWLEDGMENTS

I would like to express my sincere gratitude to my advisor Dr. Sandip Harimkar, who has given me continuous support during my Ph.D. research. Without his guidance and persistent help this dissertation would not have been possible. I also want to thank Dr. Kaan Kalkan, Dr. James Manimala, and Dr. Ranji Vaidyanathan for serving in my committee and sharing their comments and suggestion throughout my research work. I am thankful to Dr. Jim Puckette who has allowed me to use his lab equipment for my research. I would also like to thank Dr. Narendra Dahotre for allowing me to use his research lab to conduct our first laser experiments. I also acknowledge the support from the U.S. National Science Foundation (NSF CAREER Award No.: CMMI-1149079). I also thank Elsevier and Taylor & Francis for permission to include Chapter 4 of my dissertation, which was originally published in Ultrasonics, Manufacturing letters, Journal of Materials Processing Technology, and Materials and Manufacturing Processes. All of my success is possible because of the endless love and support of my mother, my sisters Zohreh and Nahid, and my brother Ali. I would like to acknowledge my colleagues, Ashish Singh, Sourabh Biswas, Tanaji Paul, Bindu Kasturi, Arezoo Zare, Seyyed Ali Shojaee, Hamid Mortazavian for helping me performing experiments, gathering the data, and analyzing the results. Finally I would like to thank my amazing friends Mehrnoush Salarian and Mohammadreza Tahriri for their unconditional support and motivation.

Acknowledgements reflect the views of the author and are not endorsed by committee members or Oklahoma State University

Name: Seyyed Habib Alavi Date of Degree: May, 2018

Institution: Oklahoma State University Location: Stillwater, Oklahoma

Title of Study: ANALYSIS AND APPLICATIONS OF MELT EXPULSION DURING ULTRASONIC VIBRATION-ASSISTED LASER SURFACE PROCESSING

Candidate for the Degree of Doctor of Philosophy

Major Field: Mechanical and Aerospace Engineering

Simultaneous application of ultrasonic vibrations during conventional material processing is recently gaining widespread attention due to enhancement of material removal mechanism and improvement in metallurgical quality. In addition, application of the high energy ultrasonic vibrations also presents a great potential to facilitate the melt expulsion in the form of sideways melt flow and droplet ejection during the laser melting of material. Such melt expulsion is likely to improve material removal efficiency and surface quality during laser machining of materials. The efficient melt expulsion is also likely to expand the application range of continuous wave CO_2 laser into processes such as laser drilling, laser atomization, laser surface texturing, and laser cutting. In this work, the ultrasonic vibration-assisted laser surface processing is proposed in which the effect of simultaneous application of ultrasonic vibration on melt expulsion characteristics during continuous wave CO_2 laser surface melting of metallic alloys (AISI 316 stainless steel and Ti6Al4V) is investigated. The application of ultrasonic vibrations during laser surface processing appears to suppress the surface melting due to increasing air flow above the surface and consequent enhancement of surface convection. Moreover, the application of ultrasonic vibrations at higher laser energy densities or longer irradiation times creates well defined craters/holes having resolidified surface films. The geometric features such as hole diameter/depth and aspect ratio of the laser drilled holes are greatly influenced by ultrasonic vibration parameters (frequency and displacement), laser parameters (irradiation time and working distance) and thermo-physical properties of the substrate. The high speed camera (HSC) images of the proposed process indicate that the melt expulsion under the influence of ultrasonic vibrations initiates after the laser melted pool reaches a critical size/volume. In addition, HSC images also reveal that increasing the ultrasonic frequency from 20 kHz to 40 kHz significantly decreases the first droplet ejection time. A multi-step finite element analysis, taking into account the observations of melt expulsion from HSC images, is developed for the prediction of hole volume. Expelled droplets exhibit narrow range of particle size and good circularity which is likely to be used in powder metallurgy applications.

ADVISOR'S APPROVAL: _____

TABLE OF CONTENTS

LIST OF TABLES

LIST OF FIGURES

Figure Page

CHAPTER 1

REVIEW OF THE LITREATURE

1.1 Laser processing

Laser processing offers interesting possibilities to modify the microstructure, phases, composition, residual stresses, and topography of the surfaces of materials through a range of laser-material interactions such as heating, melting, surface vaporization, ablation, and shock peening [1–5]. Among these laser-material interactions, surface melting is by far the most important regime for the practical applications of lasers in materials processing. The laser surface melting has been extensively used for microstructural refinement, surface alloying, and composite surfacing [6–9]. The laser surface melting is also very important in laser material removal (machining) and joining processes [10, 11]. For example, melt expulsion from the drilling or cutting surfaces is a dominant mechanism of material removal at lower power laser machining while surface evaporation becomes dominant at higher laser powers [12]. Various laser-material interactions, such as surface heating, surface melting, surface vaporization, plasma formation and surface ablation are schematically illustrated in Fig. 1.1. Laser intensity and laser irradiation time plays a key role in determining the nature of laser-material interaction. Fig. 1.2 presents various laser-material interactions and their application at different laser intensity and irradiation time.

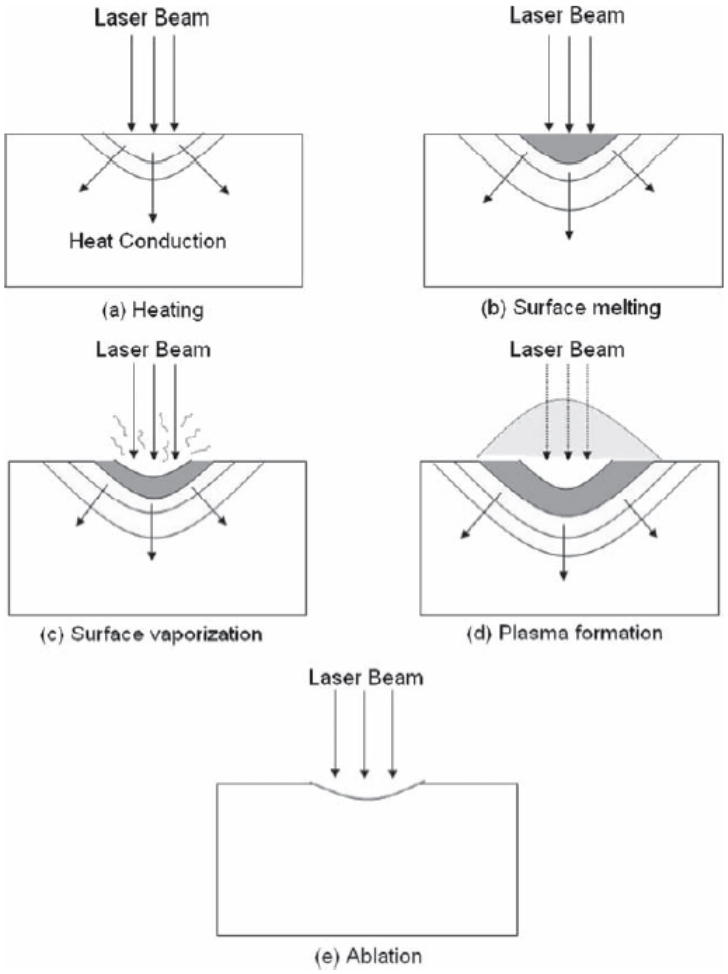

Figure 1.1: Different types of laser–material interactions: (a) heating, (b) surface melting, (c) surface vaporization, (d) plasma formation, and (e) ablation [9]

1.2 Laser drilling

Lasers are at the forefront of materials surface modification (heat treatment, melting, cladding, and coatings), machining (drilling, cutting, and milling) and forming (welding and joining) technologies [9]. Among these technologies, laser drilling of materials such as diamond wire-drawing dies and stainless steel is probably one of the earliest commercial applications of lasers in materials processing [13]. Laser drilling is also one of the most commonly used micromachining processes for creating high quality and high aspect-ratio holes in a range of materials including high performance alloys,

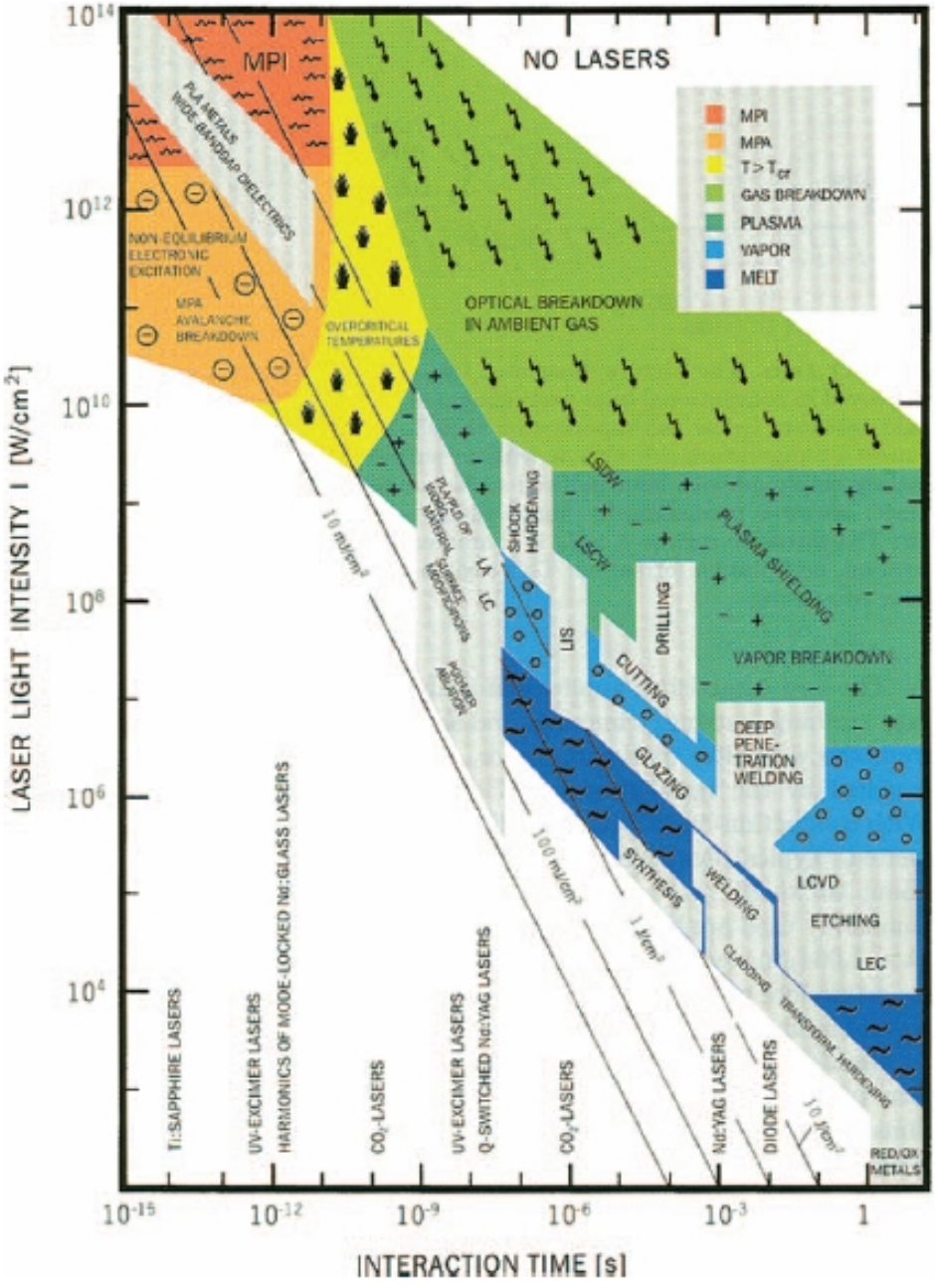

Figure 1.2: Processing map of various laser-material interactions at different laser intensities and interaction times [9]

ceramics, and composites [9, 14]. The laser drilling process offers several advantages such as non-contact processing, excellent reproducibility, and high production rates (up to 100 holes/s). It is worth mentioning that drilling rate in conventional mechanical drilling is 60 s/hole and has a limitation on high angle drilling [9]. Most of the laser drilling approaches such as single pulse drilling and percussion drilling involve pulsed laser irradiation of the material substrates. Fig. 1.3 schematically presents the various laser drilling techniques, including single pulse, percussion, trepanning [15]. In laser percussion drilling, a number of laser pulses (in the pulse duration range of ms to fs) are irradiated to the surface of the target material. This technique is normally used for micro-drilling of aerospace component and turbine blades. Laser percussion drilling potentially fabricates 1.3 mm holes through a relatively thick substrate (∼25 mm) [9, 16].

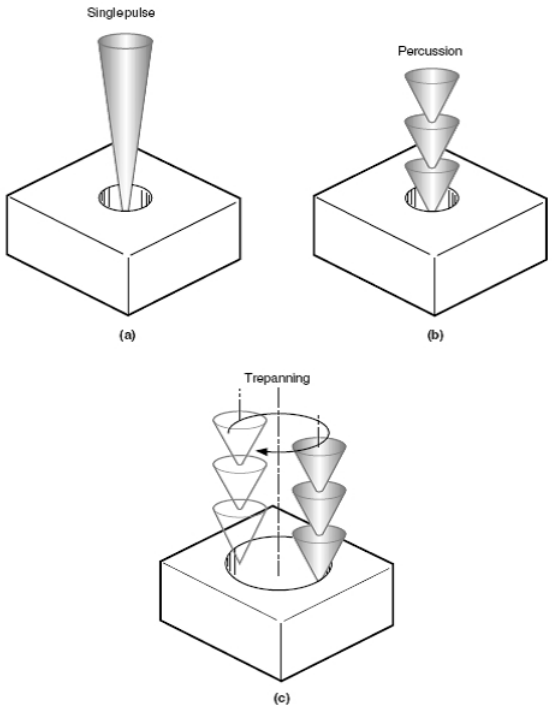

Figure 1.3: Various laser drilling techniques: (a) single pulse, (b) percussion, and (c) trepanning [9]

Laser drilling is generally performed with pulsed laser output in two distinct

regimes of laser-material interactions: direct surface ablation (pulse width<100 ns) and surface melting (pulse width in the range of 0.5 μs-10 ms). The laser drilling with direct surface ablation has been extensively used in micromachining; it is now possible to drill sub-10 μm diameter holes using state-of-the-art picosecond and femtosecond lasers [17–20]. Fig. 1.4 shows 10 μm holes in a 1.5 to 50 μm thick Aluminum foil drilled using fs laser drilling technique.

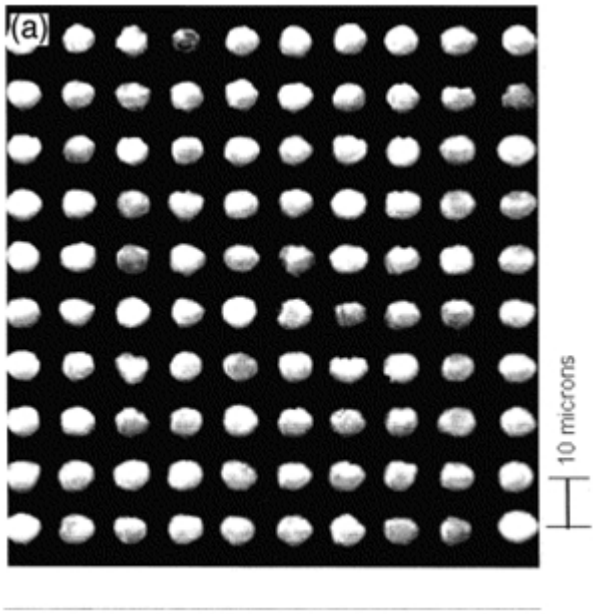

Figure 1.4: Optical microscopic images of sub-10 μm hole array drilled at 18 pulses/hole in an 18-μm thick aluminum foil (60 fs, 3.3 μJ pulses) [20]

In the laser drilling with surface melting, relatively longer pulses are used to melt and expel the molten materials from the drilling front [21, 22]. The laser drilling involving melt expulsion often results in asymmetric hole shape and recast layer formation (due to incomplete melt expulsion) [23]. Significant efforts have been made to improve the efficiency of material removal and quality of holes during laser drilling. Most of the low power laser drilling processes use coaxial assist gas to accelerate the melt expulsion to increase drilling rates, minimize the surface oxidation, and protect the optical components of the laser from ejected spatter [15, 24]. Coaxial assist gas

jets (inert gases in fusion cutting and oxygen in reactive fusion cutting) are generally used to expel thin melt films from the drilling and cutting kerfs. The melt expulsion occurs when momentum transferred to the thin melt films exceeds the surface tension forces. The rate/speed of machining and quality of the machined surfaces during laser drilling and cutting are influenced by the rate of melt expulsion and dynamics of melt flow [25]. For example, recast layer on the hole walls, spatter around the periphery of the laser drilled holes, and low hole aspect ratios are primarily due to incomplete or inefficient expulsion of the melt during laser drilling [26, 27]. While significant efforts have been made to optimize the design of the assist gas nozzles, gas pressures, and gas compositions, it is challenging to improve the machining speed and quality of laser machined surfaces especially in the surface melting regime of laser drilling/machining. Contrary to intuition, however, the increase in assist gas pressures actually increases the laser drilling time at all laser power levels [28, 29]. It has been reported that the high gas pressures form the density gradient fields and change the refractive index of the medium, resulting in defocusing of the laser beam (and hence lower energy density). The laser drilling time actually increases and then remains essentially constant with increasing assist gas pressure for a range of laser powers [28, 29]. Fig. 1.5 shows the variation of the drilling time (ms) versus the assist gas pressure (psig) for different laser powers in Al6061 and Cu specimens. The role of assist gas type in material removal laser drilling has also been extensively investigated. The inert gas assist during laser drilling minimizes the surface oxidation and related undesirable effects [29]. Oxygen gas assist lowers the overall energy requirement for material removal due to exothermic oxidation reactions. In some materials, the oxides serve as flux and reduce the viscosity of the melt, enhancing melt expulsion. The laser beam diameter and laser beam focus conditions also influence the material removal and quality of holes [21, 30, 31]. Fig. 1.6 presents the effect of assist gas on drilling time of various metal specimens.

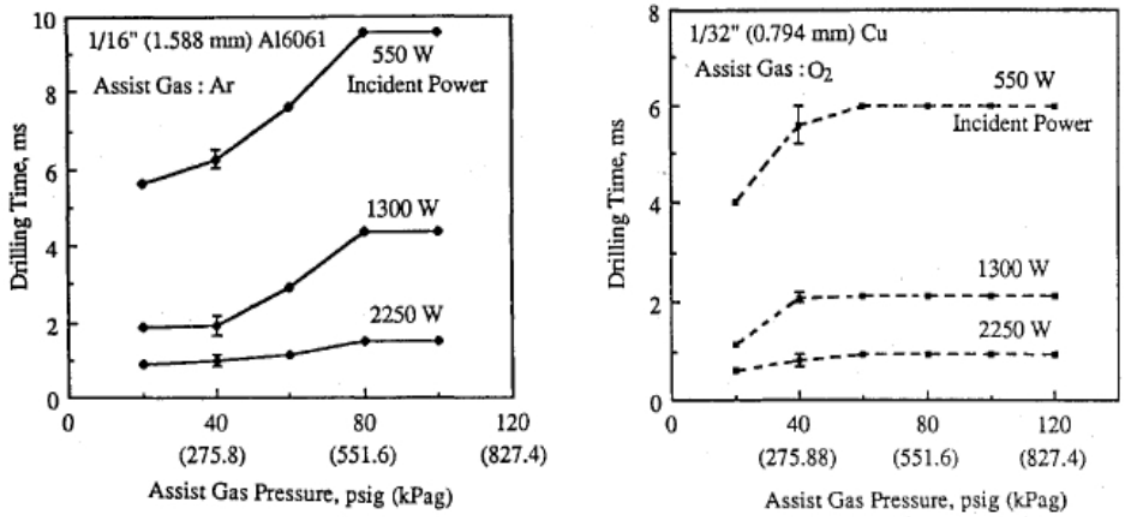

Figure 1.5: Variation of the drilling time (ms) with the assist gas pressure (psig) for different laser powers in Al6061 and Cu specimens [29]

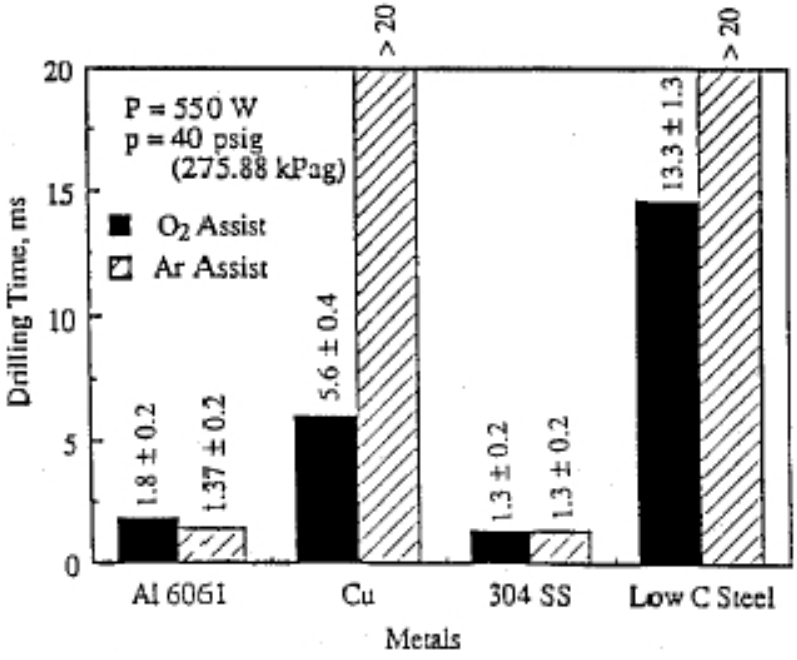

Figure 1.6: Effect of assist gas on drilling time of various metal specimens [29]

1.2.1 Quality of the laser drilled holes

In addition the high efficiency of materials removal (ablation or melt expulsion), it is important that the laser drilled holes have excellent metallurgical and geometric quality. For example, the laser drilled holes are often associated with taper, and the taper angle depends on the thickness of the work-piece [32]. Significant efforts have been made to optimize the laser focusing conditions to minimize taper of the drilled holes. It has been reported that best quality holes in terms of straightness can be obtained by positioning the laser beam waist just below the surface of the workpiece [21]. Fig. 1.7 schematically presents the effect of focusing condition on the hole geometry. However, the defocusing of the laser beam decreases the energy density and efficiency of laser melting/melt expulsion. Also, the laser drilling is often associated with formation of resolidified deoplets (spatter) or redeposition of ablated particles on the machined substrate surfaces.

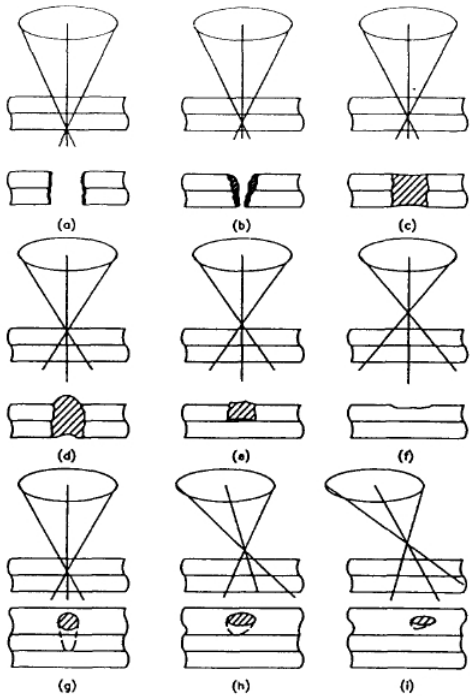

Figure 1.7: Effect of focusing conditions on the hole geometry in laser drilling [21]

As Low *et al.* [33] discussed, the efficiency of material removal (drilling rate) and the quality of drilled holes depend on the dynamics of the melt flow during laser drilling. Significant efforts have been made to improve the material removal rates and quality of holes during laser drilling. Chen *et al.* [34] studied the effect of the peak power and the pulse format on the quality of the laser drilled holes. In another study, Low *et al.* [35] investigated the effect of assist gas (O_2, Ar, N_2, and Air) on the thickness and geometry of the surface spatter formed during laser drilling and reported a significant reduction in spatter thickness in the case of O_2 assist gas. It has also been demonstrated by Low *et al.* [36] that the material ejection processes during laser drilling can be effectively controlled by temporal pulse train modulation for improving the material removal rate and quality of laser drilled holes.

1.2.2 Melt expulsion phenomena during laser processing

Irradiation of the surface of the materials with high intensity lasers (Laser power density $>10^5$-10^8 W/cm^2) can result in vaporization of the substrate. Surface vaporization eventually forms the recoil pressure (P_s) with intensity of:

$$\frac{P_s}{Q_d} = \frac{1.69}{\sqrt{L_v}} \times (\frac{b}{1+2.2b^2}) \tag{1.1}$$

where Q_d is the laser power density; and $b^2 = K_B T_s/m_v L_v$, where K_B is the Boltzmann constant, T_s is surface temperature,m is the mass of the vapor molecule, and $L_v$is the latent heat of vaporization. In typical laser machining processes (e.g. laser drilling), the recoil pressure increases and exceeds the surface tension of the melt pool and results in surface material removal. Fig. 1.8 shows the schematic of the material removal where the surface evaporation and recoil pressure are present. Fig. 1.9 presents the contribution of two main material removal mechanisms (melt expulsion and surface evaporation) to the overall material removal rate.

It can be seen that at low laser powers the dominant mechanism is melt expulsion.However, by increasing the laser power, the dominant mechanism shifts to the

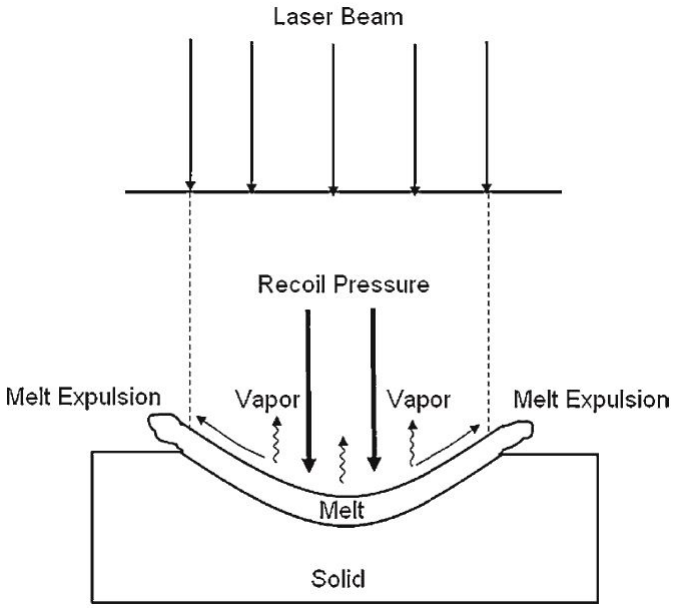

Figure 1.8: The schematic of surface evaporation and melt expulsion during laser surface irradiation [9]

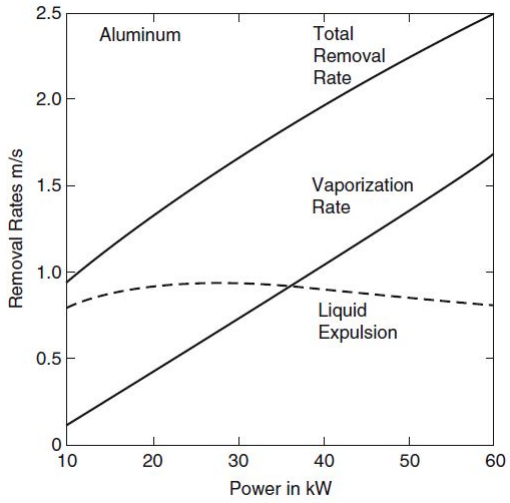

Figure 1.9: Material removal rates due to melt expulsion and vaporization for aluminum as a function of laser power [12]

surface evaporation. It has to be noted that the removal rate by melt expulsion increases with laser power and reaches to its maximum at around 20-30 kW of laser power, and then decreases by further increase of laser power. However, the material removal rate by surface evaporation shows continuous increases with laser power. As discussed earlier, melt expulsion plays an important role in material removal during laser drilling and many efforts have been devoted to mathematically model the material removal process incorporating the melt expulsion contribution in existing pure evaporation models. In one study, Von Allmen [37] developed a theoretical model that includes expulsion of liquid material and calculated the drilling velocity and drilling efficiency as a function of the absorbed intensity. The results were then verified experimentally using the pulse Nd:YAG laser. He concluded that the theoretical model was found most accurate in laser power densities of 1 and 100 MW/cm^2 where reflection losses and vapor absorption can be neglected. Fig 1.10 presents the drilling velocity for copper showing fictitious drilling velocities corresponding to either pure evaporation $(\frac{1}{\rho})_{Lv}$ or pure liquefaction $(\frac{1}{\rho})_{Ll}$.

1.3 Ultrasonic vibration-assisted materials processing

Application of ultrasonic vibration in machining of materials first reported in a paper published in 1927 and a patent granted in 1945 [38]. The vibrational displacement of the USM is generally 5-50 μm at a frequency of 20 kHz or above. the ultrasonic power varies from 50-3000 W [38]. Significant efforts have been made in the past to use the desirable effects associated with the application of ultrasonic vibrations during conventional manufacturing, resulting in the emergence of a new field of ultrasonic vibration-assisted manufacturing [27,39]. The ultrasonic vibration-assisted machining is widely investigated for precision manufacturing of brittle ceramics. In this case, the repeated impacts of the vibrating tool facilitate material removal by micro-chipping. The schematic of the ultrasonic vibration-assisted cutting setup is shown in Fig.

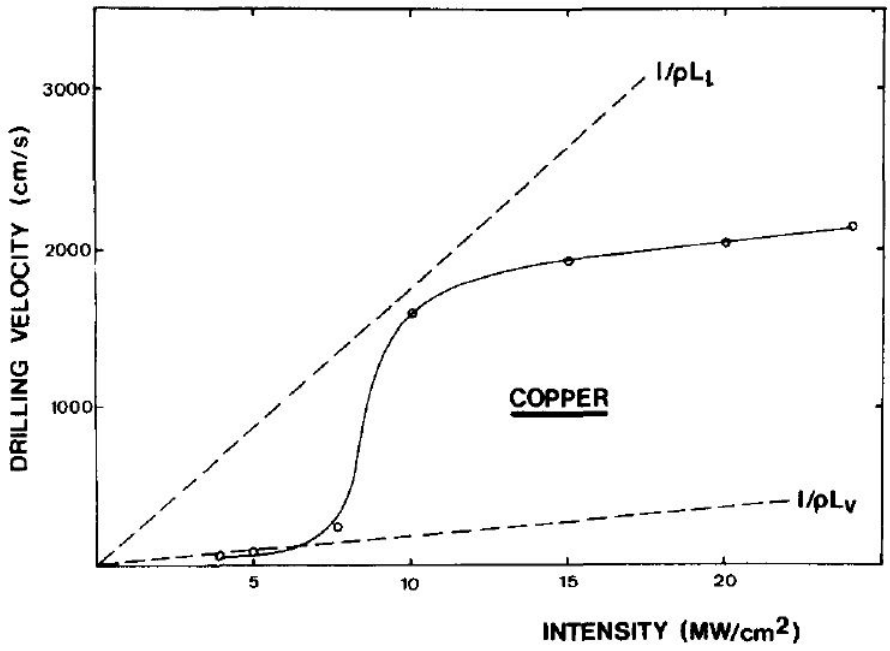

Figure 1.10: Drilling velocity for copper as a function of laser intensity including the evaporation and liquefacation contributions [37]

1.11. It has been observed that the application of ultrasonic vibrations (frequency: 40 kHz; amplitude: 3 μm) enables the machining in ductile regime for the brittle ceramics, especially at low depth of cut [40]. The process has been investigated for both traditional and non-traditional machining of materials with and without use of abrasive slurry (mechanical drilling, diamond cutting, lapping, electro-discharge machining, etc.) [38, 41].

Ultrasonic vibrations have been assisted the common machining techniques to enhance the micro hole formation. for example, it has been reported that the application of ultrasonic vibrations (frequency: 61.5 kHz) in the micro electro-discharge machining increases the aspect ratio of the microholes by 132% in stainless steel [43]. In an another study, conventional mechanical and ultrasonic assisted drilling of Inconel 738-LC were compared [44]. It has been reported that application of the ultrasonic vibrations enhanced the surface roughness and circularity of the holes by 60%. Fig.

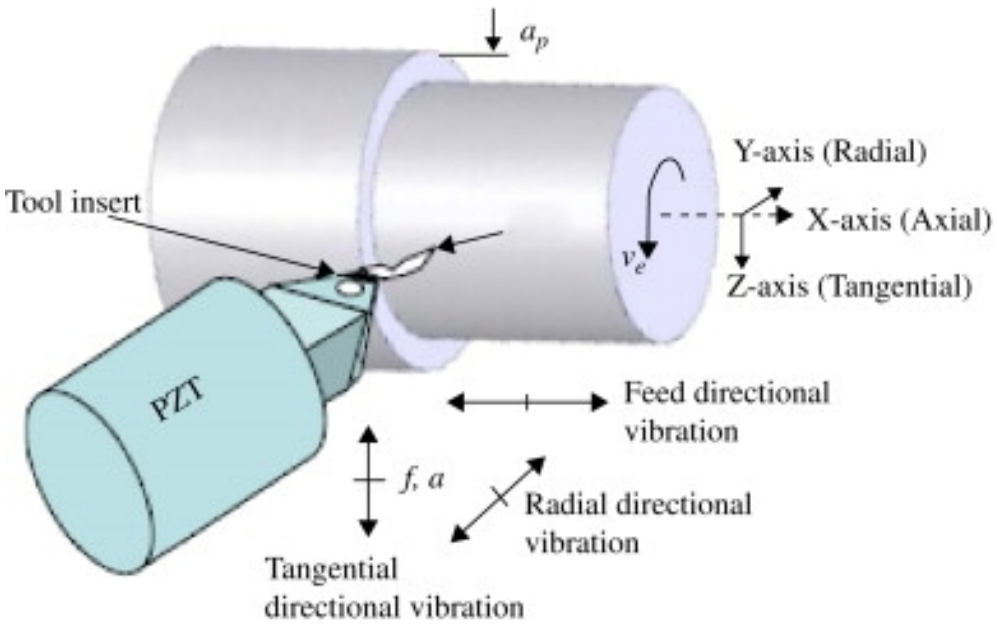

Figure 1.11: The schematic of the ultrasonic vibration-assisted cutting setup [42]

1.12 presents the surface roughness and circularity of the drilled holes with and without application of the ultrasonic vibration.

In Fig. 1.13 the optical images of the drilled holes with and without application of the ultrasonic vibration are shown. While most of the reported traditional and nontraditional machining processes utilize the desirable effects of the application of ultrasonic vibrations in the solid state (microchipping, brittle to ductile transition, and removal of ablated debris), the application of ultrasonic vibrations also offers unique effects in manufacturing that involves melting of materials. The ultrasonic vibrations have been utilized for improving the metallurgical quality and refining the grain structure of the metal/alloy castings. For example, Jian *et al.* [45] reported that the application of ultrasonic vibrations (frequency: 20 kHz; amplitude: 56.7 μm) during casting of an aluminum alloy (A356) resulted in the reduction of grain size of the eutectic silicon from 26 to 2 μm. It is well established that mechanical and electromagnetic stirring of the melt during casting facilitate the columnar to equiaxed transition (CET) of the grain structure, resulting in grain refinement [46].

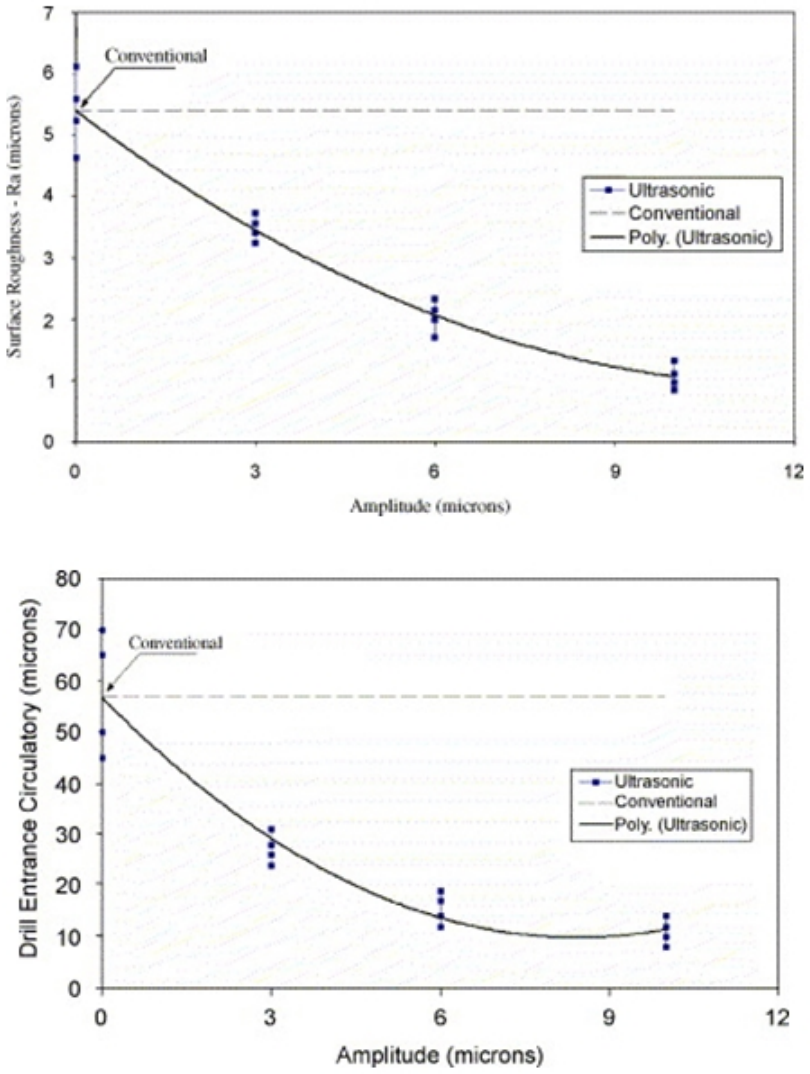

Figure 1.12: Surface roughness and circularity of the drilled holes with and without application of the ultrasonic vibration [44]

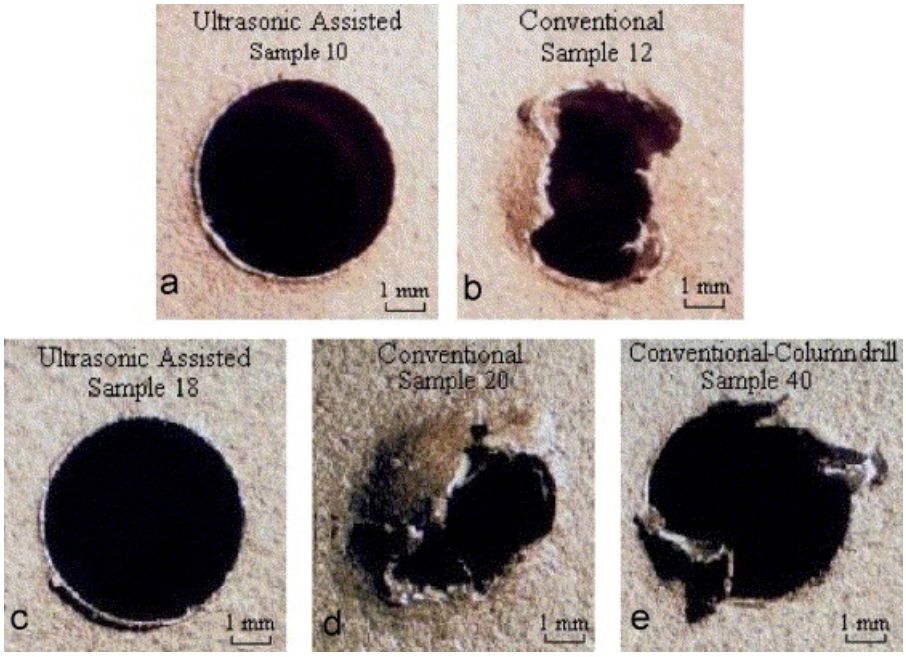

Figure 1.13: Optical images of the drilled holes with and without application of the ultrasonic vibrations [44]

The ideas have been extended for improving the microstructure of weld metal during ultrasonic vibration assisted arc welding process. For example, Cui *et al.* [47] reported the elimination of the unmixed zone in the welding of the super-austenitic stainless steel in the presence of the ultrasonic vibrations (frequency: 20 kHz). Cui *et al.* [48] also observed significant reduction in columnar dendritic microstructure with the application of ultrasonic vibrations during shielded metal arc welding (SMAW) of AISI 304 stainless steel. It was reported that the amount of columnar dendritic microstructure decreased from about 95% to 10% with increasing ultrasonic power output from 0 to 90%.

1.4 Ultrasonic vibration-assisted laser processing

Most of the processes that utilize the desired effects of ultrasonic vibrations during solidifying melt exhibit relatively slow cooling and solidification rates. The application of ultrasonic vibrations to rapidly solidifying melt is not well investigated. As

rapid melting/solidification is encountered during several laser manufacturing processes such as surface modification (laser melting, alloying, cladding, and composite surfacing), forming (laser welding/joining), and material removal (laser machining) processes, the application of ultrasonic vibrations during laser processing presents a great potential for improving the microstructure, metallurgical quality, and material removal rates of the processed materials. Recently, Zheng and Huang reported ultrasonic vibrations-assisted femtosecond machining of microholes in Nitinol substrates with an improvement in hole wall surface quality and higher hole aspect ratio [49]. They used femtosecond pulsed laser (Ti-Sapphire) in combination with ultrasonic vibrations (frequency: 40 kHz; amplitude: 2.5 μm) and reported that ultrasonic vibrations facilitates the removal of ablated particles by enhancing the heat transfer of the particles (i.e. better cooling of the particles, and hence, reduced tendency of the particles to bond to the hole wall and substrate surface) [49]. They also mentioned that the depth of the hole increased from 1.65 mm to 1.95 mm while the ultrasonic vibration was applied to the femtosecond laser drilling. Fig. 1.14 shows the schematic of the drilled holes and SEM images of the wall of the drilled holes with and without application of the ultrasonic vibration. They also reported that the aspect ratio of the drilled micro-holes was increased from 50 to 56 where the ultrasonic vibration is applied.

Chiu *et al.* [50] also investigated the ultrasonic vibration-assisted (frequency: 20 kHz; amplitude: 10 μm) pulsed excimer laser (KrF laser) machining and cleaning of the PZT materials. In these studies on ultrasonic vibration-assisted laser machining, pulsed lasers were used and the dominant material removal mechanism was ablation [48,50]. The pulsed lasers such as pulsed KrF and Ti:Sapphire lasers are traditionally used for drilling, and the application of ultrasonic vibrations in these studies was to facilitate the removal of ablated debris and particles from the surface to improve surface quality and machining rate. Lau *et al.* [51] and Yue *et al.* [52] also reported

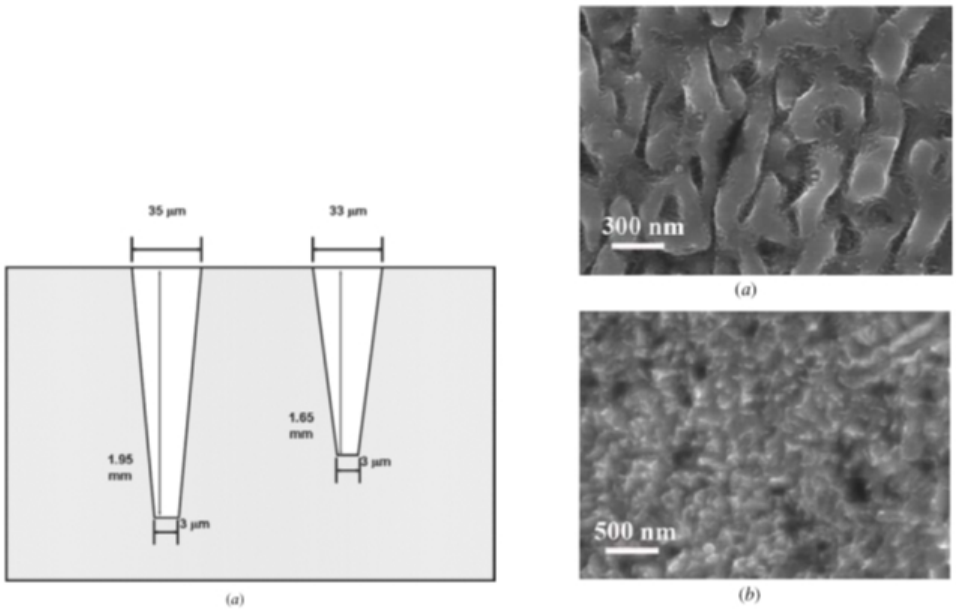

Figure 1.14: Schematic of the drilled holes and SEM images of the wall of the drilled holes with and without application of the ultrasonic vibrations [49]

that the simultaneous application of ultrasonic vibrations during pulsed laser drilling improve the material removal and quality of laser drilled holes. With this approach of ultrasonic vibrations-aided pulsed laser drilling, about 20% increase in hole depth and about 30% reduction in heat affected zone were reported by for aluminum matrix composites. However, even with these advances, laser drilling of large aspect-ratio holes with acceptable surface quality and reproducibility is still a challenge in adopting the technology for wider applications. Kang *et al.* [53] also investigated the application of ultrasonic vibration (frequency: $\sim$30 kHz; longitudinal amplitude: 3 μm) on the ns-laser (pulse width: 200 ns; max. pulse energy: 1mJ) machining. Furthermore they reported reaching a higher surface quality, reduced re-solidified layer thickness and inhibition of on oxide layer formation.

1.4.1 Enhancement of heat transfer by ultrasonic vibrations

Application of the ultrasonic vibrations agitates the fluid (e.g. air, water, molten metal) around/near the ultrasonic tip. The enhancement of surface convection, and consequent loss of energy, is expected due to the induced fluid flow during application of ultrasonic vibrations. Significant efforts have been made to study the effect of ultrasound on the heat transfer enhancement. It has been reported that ultrasonic vibration can enhance the convection heat transfer coefficient (h) up to 25 times. For example, Nomura *et al.* [54] used a 600 W ultrasonic generator with a frequency of 40 kHz to investigate the heat transfer enhancement on the narrow surface. They reported a 10-fold increase in the heat transfer coefficient in presence of ultrasound. In another study, Wong *et al.* [55] studied the natural convection enhancement with Pt wire in different liquid mediums (frequency: 20-300 kHz). They reported that applying ultrasonic vibration increases the heat transfer coefficient by a factor of 8. In one of the first studies on the effect of ultrasonic vibration on heat transfer, Fairbanks [56] reported an increase 4 times greater in heat convection from the surface of heated steel (up to 973 K) to the air. The influence of ultrasonic vibration parameters on enhancement of the convection heat transfer coefficient is summarized and presented in Fig. 1.15 [57].

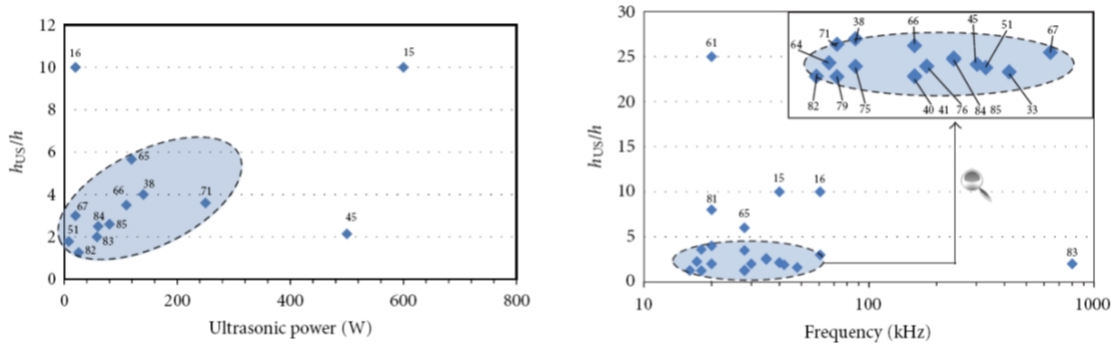

Figure 1.15: The influence of ultrasonic vibration parameters on enhancement of the convection heat transfer coefficient [57]

CHAPTER 2

HYPOTHESIS AND OBJECTIVES

While the conventional laser drilling is primarily performed using pulsed lasers, the continuous wave lasers are used in surface engineering applications. Continuous wave (CW) laser surface melting, with steady state melting conditions reached at sufficiently high laser scanning velocities, results in the formation of well-defined resolidified bead on the surface. A continuous laser irradiation at a spot (i.e. stationary irradiation without scanning) on the surface also forms a well-defined melt pool, albeit with some surface rippling in some cases. These characteristics are very useful for surface modification of materials, and hence, continuous wave lasers are most appropriate for laser surface engineering applications as described in [59]. The continuous wave lasers are also used in cutting applications where the assist gases expel the melt from the bottom of the cutting front/kerf. However, the use of continuous wave lasers, even with the presence of assist gases, in material drilling applications is limited.

Significant efforts have been made in the past to use the desirable effects associated with the application of ultrasonic vibrations during conventional manufacturing, resulting in the emergence of a new field of ultrasonic vibration-assisted manufacturing. Most of the processes that utilize the desired effects of ultrasonic vibrations during solidifying melt exhibit relatively slow cooling and solidification rates. The application of ultrasonic vibrations to rapidly solidifying melt is not well investigated. As rapid melting/solidification is encountered during several laser manufacturing processes such as surface modification (laser melting, alloying, cladding, and composite

surfacing), forming (laser welding/joining), and material removal (laser machining) processes, the application of ultrasonic vibrations during laser processing presents a great potential for improving the microstructure, metallurgical quality, and material removal rates of the processed materials. The proposed ultrasonic vibration-assisted continuous wave laser surface processing extends the energy-efficient laser melting (no drilling) regime for laser drilling applications and enables continuous (instead of discontinuous pulsed) drilling, atomization, and physical texturing of materials. With the widespread use of continuous wave CO_2 lasers in industry, the proposed laser surface processing approach is likely to expand the applications of these lasers for flexible manufacturing.

2.1 Global Hypothesis

Major hypothesis of this work is that high power ultrasonic vibrations with medium to high longitudinal amplitudes (displacements) (5-75 μm) are expected to facilitate the melt expulsion in the continuous wave (CW) laser surface melting process and extend the laser melting regime of the CW laser-material interactions for machining of materials and expand the applications of these widely used lasers for flexible manufacturing.

2.2 Primary objectives

The primary objectives of this study are to simultaneously apply the ultrasonic vibrations (20 and 40 kHz) with a wide range of amplitudes to the CW-laser surface processing of metallic alloys. Furthermore, the effects of ultrasonic vibrations on surface properties of the laser irradiated specimens and melt expulsion phenomena during the ultrasonic vibration-assisted laser surface processing is investigated. To reach the aforementioned objective, this work investigates fundamental studies below:

1. **Study 1: Ultrasonic vibration-assisted laser surface melting**: In this study larger laser working distances (50 mm) are selected to investigate the transition between surface melting and melt expulsion. The outcome of this study is used to design the experimental matrix in further studies.

2. **Study 2: Ultrasonic vibration-assisted laser surface drilling**: In this studies the higher concentration of the laser beam (by decreasing the working distance) is used to study the feasibility of the drilling and also investigate the effects of laser irradiation times, working distance, thermo-physical properties of the substrates, and ultrasonic frequencies on geometry and quality of the holes.

3. **Study 3: Ultrasonic vibration-assisted laser atomization**: In this study the melt expulsion phenomena is investigated. The expelled molten materials, as the result of melt expulsion during ultrasonic vibration-assisted laser drilling, are collected and microstructural analysis of the droplets are performed.

4. **Study 4: Ultrasonic vibration-assisted laser surface physical texturing**: In the last study, the controlled ultrasonic vibrations are simultaneously applied to the laser surface melting to form physical texturing on the surface without significant melt expulsion. Microhardness, corrosion, and surface roughness of the specimens are also measured.

CHAPTER 3

METHODOLOGY

The general information regarding the experimental setup are reported in this section. However, to clarify the details of each experiments, more information on methods and materials are reported in corresponding subsection.

The set-up for ultrasonic vibration-assisted laser surface processing is shown in Fig. 3.1. The set-up consisted of a threaded titanium alloy probes (horn) of 13 and 25

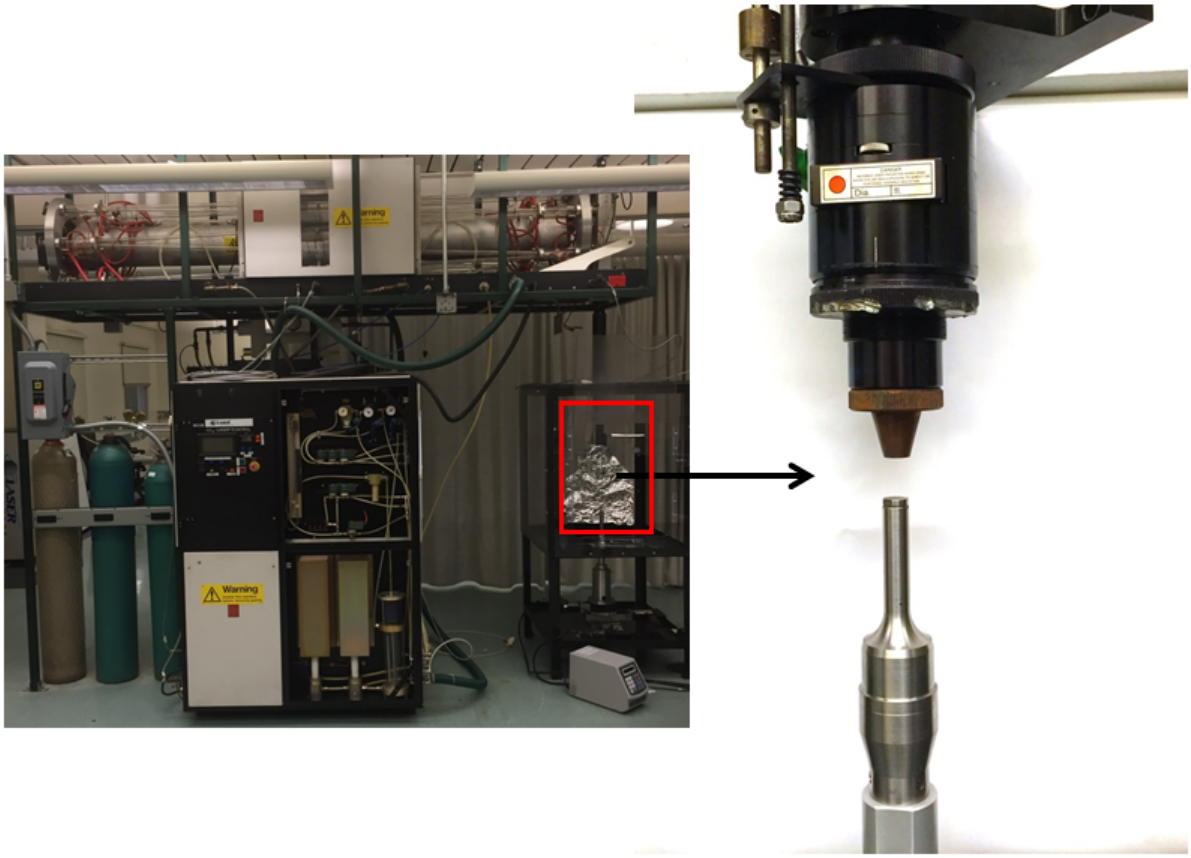

Figure 3.1: Ultrasonic vibration-assisted laser surface processing setup

mm diameter and 139 mm length. The ultrasonic power supply delivered the power output of 750 W at a fixed frequencies of 20 and 40 kHz (Sonics & Materials, Inc, Newtown, CT). AISI 316 austenitic stainless steel(17.45% Cr, 11.81% Ni, 2.5% Mo, 0.05% C, 1.35% Mn, 0.68% Si, 0.011% S, 0.047% P, and balance Fe by weight) tips of 2 mm thickness were used as specimens for ultrasonic vibration-assisted laser surface processing.

The surfaces of the specimens were polished with SiC paper (1200 grit) followed by cloth polishing with alumina powder (0.5 μm particle sizes) to render mirror finish. To increase the absorption of laser radiation, the specimen surfaces were sand blasted. The specimens were immediately washed and dried after etching. Each specimen tip was then screwed on the threaded end of the ultrasonic probe. For the ultrasonic-vibration assisted laser surface processing, a continuous wave CO_2 laser with laser power of 900 to 1000 W was irradiated on the vibrating specimens. The laser beam diameter was about 100 μm at the exit of the laser head. The laser processing was conducted with the defocused beam (in the range of 1 to 7 mm in diameter) with the distance from the laser head to the surface of the specimen of about 10 to 50 mm. The spot diameter of the CO_2 laser was calculated by equation below:

$$Spotdiameter = 1.27 \times f \times \lambda \times \frac{M^2}{D} \tag{3.1}$$

where f is lens focal point (mm), λ is wavelength of the laser (μm), M^2 is the laser beam parameter (here it is assumed 1), and D is the working distance (mm). The variation of the laser beam diameter and working distance is presented in Fig 3.2.

The laser beam energy profile was Gaussian, and the beam was irradiated perpendicular to the vibrating surface. The power output controls the amplitude of vibration at the surface of the specimen tip. A 3D optical profilometer (Nanovea, Irvine, CA) was used to measure the vibration displacement at each power output. The optical profiler detects a step corresponding to vibration displacement in the surface profile when the ultrasonic system is turned on during the measurement. The surface profiles

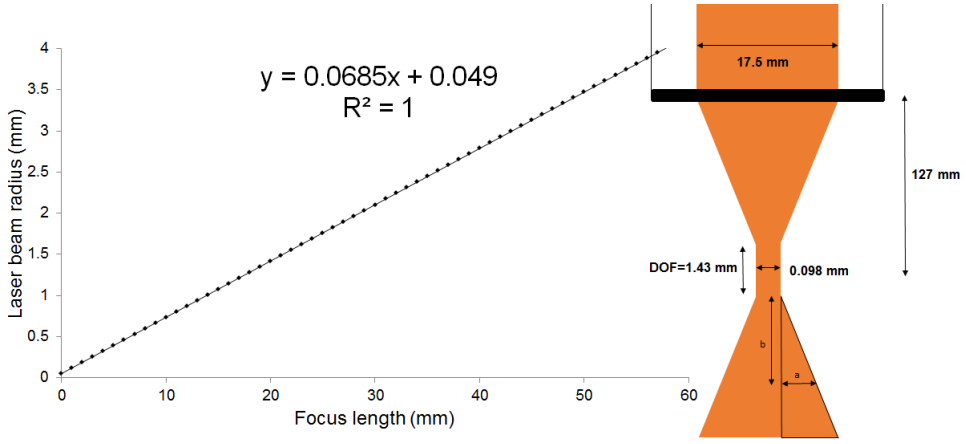

Figure 3.2: The variation of the laser beam diameter with working distance for the CO_2 laser used in this work

for the ultrasonic vibrations (at 20 kHz) at the specified power outputs are shown in Fig. 3.3. The vibration displacements of 23, 37, and 51 μm were measured for the power outputs of 20, 30, and 40%, respectively (at 20 kHz).

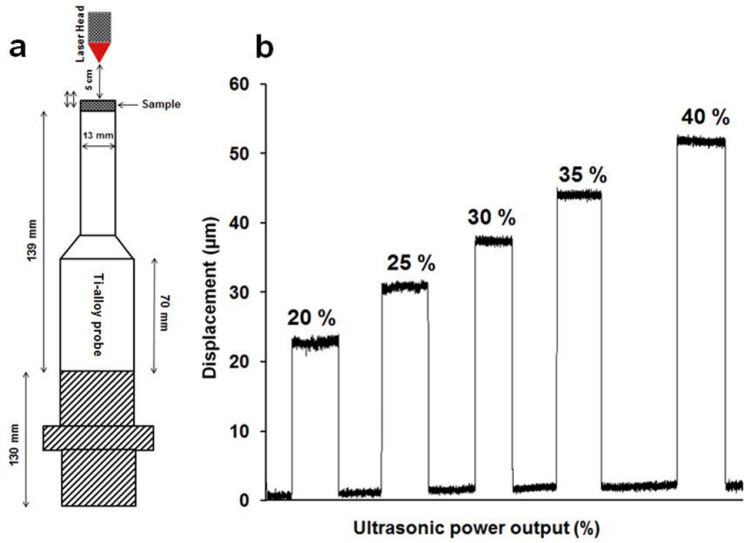

Figure 3.3: Surface profiles for the ultrasonic vibrations at the specified power outputs [63, 64]

CHAPTER 4

FINDINGS

4.1 Ultrasonic vibration-assisted laser surface melting

4.1.1 Introduction

Laser processing offers interesting possibilities to modify the microstructure, phases, composition, residual stresses, and topography of the surfaces of materials through a range of laser-material interactions such as heating, melting, surface vaporization, ablation, and shock peening [1–5, 58]. Among these laser-material interactions, surface melting is by far the most important regime for the practical applications of lasers in materials processing. The laser surface melting has been extensively used for microstructural refinement, surface alloying, and composite surfacing [6–9]. The laser surface melting is also very important in laser material removal (machining) and joining processes [10, 11]. For example, melt expulsion from the drilling or cutting surfaces is a dominant mechanism of material removal at lower power laser machining while surface evaporation becomes dominant at higher laser powers [12]. Coaxial assist gas jets (inert gases in fusion cutting and oxygen in reactive fusion cutting) are generally used to expel thin melt films from the drilling and cutting kerfs. The melt expulsion occurs when momentum transferred to the thin melt films exceeds the surface tension forces. The rate/speed of machining and quality of the machined surfaces during laser drilling and cutting are influenced by the rate of melt expulsion and dynamics of melt flow [25]. For example, recast layer on the hole walls, spatter around the periphery of the laser drilled holes, and low hole aspect ratios are primar-

ily due to incomplete or inefficient expulsion of the melt during laser drilling [26, 27]. While significant efforts have been made to optimize the design of the assist gas nozzles, gas pressures, and gas compositions, it is challenging to improve the machining speed and quality of laser machined surfaces especially in the surface melting regime of laser drilling/machining. Significant efforts have been made in the past to use the desirable effects associated with the application of ultrasonic vibrations during conventional manufacturing, resulting in the emergence of a new field of ultrasonic vibration-assisted manufacturing [39,40]. The ultrasonic vibration-assisted machining is widely investigated for precision manufacturing of brittle ceramics. In this case, the repeated impacts of the vibrating tool facilitate material removal by micro-chipping. It has also been observed that the application of ultrasonic vibrations (frequency: 40 kHz; amplitude: 3 μm) enables the machining in ductile regime for the brittle ceramics, especially at low depth of cut [40]. The process has been investigated for both traditional and non-traditional machining of materials with and without use of abrasive slurry (mechanical drilling, diamond cutting, lapping, electro-discharge machining, etc.) [38, 41]. It has been reported that the application of ultrasonic vibrations (frequency: 61.5 kHz) in the micro electro-discharge machining increases the aspect ratio of the microholes by 132% in stainless steel [43]. A few attempts have also been made to use the desirable effects of ultrasonic vibrations during laser machining (drilling) of materials. For example, Zheng and Huang reported application of ultrasonic vibrations (frequency: 40 kHz; amplitude: 2.5 μm) during femtosecond pulsed laser (Ti-Sapphire laser) micro-drilling of the Nitinol samples with an improvement in hole wall surface quality and higher hole aspect ratio [49]. Chiu *et al.* also investigated the ultrasonic vibration (frequency: 20 kHz; amplitude: 10 μm) assisted pulsed excimer laser (KrF laser) machining and cleaning of the PZT materials [50]. In these studies on ultrasonic vibration-assisted laser machining [49, 50], pulsed lasers were used and the dominant material removal mechanism was ablation. The pulsed lasers

such as pulsed KrF and Ti:Sapphire lasers are traditionally used for drilling, and the application of ultrasonic vibrations in these studies was to facilitate the removal of ablated debris and particles from the surface to improve surface quality and machining rate. While most of the reported traditional and non-traditional machining processes utilize the desirable effects of the application of ultrasonic vibrations in the solid state (micro-chipping, brittle-ductile transition, and removal of ablated debris), the application of ultrasonic vibrations also offers unique effects in manufacturing that involves melting of materials. The ultrasonic vibrations have been utilized for improving the metallurgical quality and refining the grain structure of the metal/alloy castings. For example, Jian *et al.* reported that the application of ultrasonic vibrations (frequency: 20 kHz; amplitude: 56.7 μm) during casting of an aluminum alloy (A356) resulted in the reduction of grain size of the eutectic silicon from 26 to 2 μm [45]. It is well established that mechanical and electromagnetic stirring of the melt during casting facilitate the columnar to equiaxed transition (CET) of the grain structure, resulting in grain refinement [46]. The ideas have been extended for improving the microstructure of weld metal during ultrasonic vibration-assisted arc welding process. For example, Cui *et al.* reported the elimination of the unmixed zone in the welding of the super-austenitic stainless steel in the presence of the ultrasonic vibrations (frequency: 20 kHz) [47]. Cui *et al.* also observed significant reduction in columnar dendritic microstructure with the application of ultrasonic vibrations during shielded metal arc welding (SMAW) of AISI 304 stainless steel. It was reported that the amount of columnar dendritic microstructure decreased from about 95% to 10% with increasing ultrasonic power output from 0 to 90% [48]. Most of the processes that utilize the desired effects of ultrasonic vibrations during solidifying melt exhibit relatively slow cooling and solidification rates. The application of ultrasonic vibrations to rapidly solidifying melt is not well investigated. As rapid melting/solidification is encountered during several laser manufacturing processes such as surface modi-

fication (laser melting, alloying, cladding, and composite surfacing), forming (laser welding/joining), and material removal (laser machining) processes, the application of ultrasonic vibrations during laser processing presents a great potential for improving the microstructure, metallurgical quality, and material removal rates of the processed materials. In this paper, a new ultrasonic vibration-assisted laser surface processing approach is presented for surface melting of AISI 316 stainless steel. The laser processing was conducted with simultaneous application of ultrasonic vibrations (20 kHz) in the surface melting regime, and the effect of ultrasonic vibrations on the development of microstructure in the resolidified melt pool is analyzed.

4.1.2 Materials and Methods

The set-up consisted of a threaded titanium alloy probe (horn) of 13 mm diameter and 139 mm length. The ultrasonic power supply delivered the power output of 750 W at a fixed frequency of 20 kHz (Sonics & Materials, Inc, Newtown, CT). AISI 316 austenitic stainless steel tips of 2 mm thickness were used as specimens for ultrasonic vibration-assisted laser surface processing. The surfaces of the steel specimens were polished with SiC paper (1200 grit) followed by cloth polishing with alumina powder (0.5 4μm particle sizes) to render mirror finish. To increase the absorption of laser radiation, the specimen surfaces were etched for 20 s using a common etchant for 300 series stainless steels (Carpenters stainless steel etch; 6 mL HNO3, 122 mL HCl, 122 mL Ethanol, 8.5 g FeCl3, and 2.4 g CuCl2). The specimens were immediately washed and dried after etching. Each specimen tip was then screwed on the threaded end of the ultrasonic probe. For the ultrasonic-vibration assisted laser surface processing, a continuous wave CO_2 laser with laser power of 900 W was irradiated on the vibrating specimens. The laser beam diameter was about 100 μm at the exit of the laser head. The laser processing was conducted with the defocused beam (about 7 mm in diameter) with the distance from the laser head to the surface of the specimen of

about 5 cm. The laser beam energy profile was Gaussian, and the beam was irradiated perpendicular to the vibrating surface (i.e. vibration amplitude parallel to the beam). The laser processing was conducted for three irradiation times: 0.30, 0.35, and 0.45 s. For each laser irradiation time, the processing was conducted with three ultrasonic vibration power outputs: 20, 30, and 40%. The power output controls the amplitude of vibration at the surface of the specimen tip. A 3D optical profilometer (Nanovea, Irvine, CA) was used to measure the vibration displacement at each power output. The optical profiler detects a step corresponding to vibration displacement in the surface profile when the ultrasonic system is turned on during the measurement. The vibration displacements of 23, 37, and 51 μm were measured for the power outputs of 20, 30, and 40%, respectively. The laser irradiation times and ultrasonic power outputs used in this investigation were the optimum parameters that resulted in the laser-material interaction (heating/melting), and showed transition in the melt flow behavior for the case of surface melting. The laser processing and ultrasonic vibration parameters for the three sets of experiments are summarized in 4.1. The phase identification of the laser processed specimens was performed using an x-ray diffractometer (BRUKER AXS, Inc, Madison, WI) operating with Cu K radiation. The diffraction angle (2θ) was varied between 20 and 100$\circ$. The surface profiles of the laser processed specimens were also recorded using 3D optical profilometer (Nanovea, Irvine, CA). A scanning electron microscope (JEOL Ltd, Tokyo, Japan) was used to characterize the microstructures at the surface and in the polished cross sections of the laser processed specimens. ImageJ software was used for the measurement of melt film thickness, and at least 9 measurements were taken for each sample on the crater walls from the cross-sectional SEM micrographs.

4.1.3 Results and Discussion

Laser surface processing for irradiation time of 0.30 s

The surface and cross sectional SEM micrographs of the steel samples laser irradiated for 0.30 s with and without the simultaneous application of ultrasonic vibrations are presented in Fig.5.1. The sample laser irradiated without application of ultrasonic vibrations exhibited a well-defined central melted region with surrounding heat affected zone (HAZ) as shown in Fig.5.1(a). From the surface micrographs, the diameter of the affected region in this sample is about 1.5 mm. The corresponding cross sectional image shows a well-defined melt pool characteristic of laser surface melting of materials [59]. The width and depth of the melt pool was 988 and 157 μm, respectively. However, for the similar laser processing parameters (laser power of 900 W and interaction time of 0.30 s), the laser interaction with the surface was very weak with the application of ultrasonic vibrations. The surfaces of the samples processed with ultrasonic-assisted laser surface processing showed only darker contrast due to surface heating, and no melting was observed for these samples (Fig.5.1(b-c)). While the diameter of the heat affected zones remained at about 1.5 mm, the contrast of the laser irradiated regions became progressively weaker with increasing ultrasonic vibration output power (corresponding to increasing vibration amplitude). The corresponding cross sectional SEM micrographs also showed only HAZ without any surface melting. The depth of the HAZ decreased from 220 μm to 185 μm with increasing ultrasonic power output from 20 to 30%. At about 40% power output, the contrast of the laser irradiated region was almost completely faded (not shown in the figure). The cross sectional SEM micrograph also did not show any contrast for this condition. Clearly, the ultrasonic vibrations weaken the laser interaction with the steel samples, eliminating the possibility of surface melting as observed for the samples laser irradiated without the application of vibrations. Also, the laser interaction (formation

of HAZ at the irradiated regions) progressively diminishes with increasing ultrasonic power output. The figure also shows deformation/flow lines (wavy patterns) in the substrate regions unaffected by laser irradiation. The appearance of such flow lines post deformation processing such as extrusion, forging, and rolling is very common. When a laser beam is irradiated on a metallic surface, an absorbed energy results in the excitation of electrons generating heat [9]. Various heat transfer processes such as conduction into the material and convection and radiation from the surface cause the dissipation of heat generated at the surface. Most of the laser-material interaction effects such as heating and melting are due to the conduction of heat into the material. An overall conduction flux in the material based on energy balance is given by [9]:

$$-k[(\frac{\partial T}{\partial x}) + (\frac{\partial T}{\partial y}) + (\frac{\partial T}{\partial z}) = AI_0 - \epsilon\sigma[T^4 - T_0^4] - h[T - T_0] \tag{4.1}$$

where k is the thermal conductivity, A is the absorptivity, I_0 is the incident laser intensity, ϵ is the emissivity, σ is the Stefan-Boltzmann constant, and h is the convective heat transfer coefficient.

It appears that, during laser irradiation for 0.30 s, the ultrasonic vibrations accelerate the heat dissipation by convection from the surface of the sample. This causes the samples to heat relatively slowly, and the surface temperature does not reach the melting point ($\sim$ 1375 °C) of the steel within the laser irradiation time of 0.30 s. For the given ultrasonic vibration frequency (20 kHz), the convective heat dissipation becomes increasingly severe with increasing ultrasonic power output (corresponding to increasing vibration amplitude). This results in progressive disappearance of HAZ with increasing ultrasonic power output. The effects of ultrasonic vibrations on the enhancement of convective heat transfer in fluid and air are well reported in the literature [57]. For example, Loh *et al.* investigated acoustic streaming and associated convection enhancement due to ultrasonic flexural vibrations [60]. The authors ex-

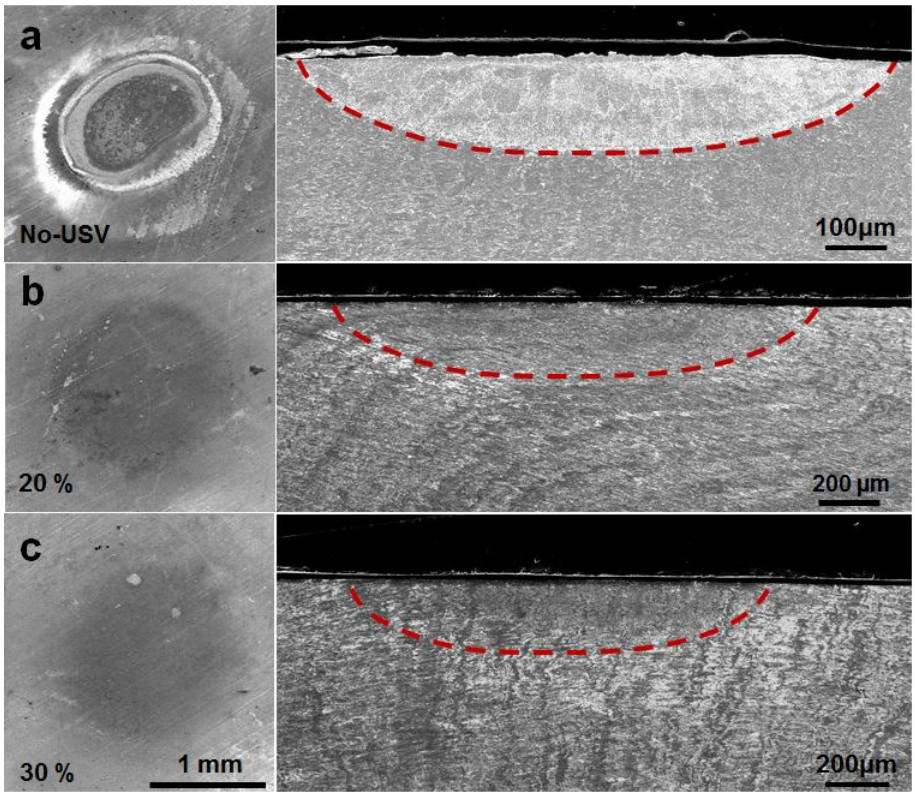

Figure 4.1: Surface and cross-sectional micrographs of steel samples laser irradiated for 0.30 s: (a) without ultrasonic vibrations, (b) with ultrasonic vibrations at power output of 20 %, and (c) with ultrasonic vibrations at power output of 30 %

perimentally observed the acoustic streaming patterns that corresponded well with the predictions based on Nyborg's theory of acoustic streaming. A notable drop in temperature of about 40 °C in 4 min. (for an aluminum plate heated to 98 °C) was observed with vibration amplitude of 25 μm at the vibration frequency of 28.4 kHz [60]. The investigation further demonstrated that the maximum acoustic streaming velocity increases with increasing vibration amplitude at a given vibration frequency [60]. It appears that similar convection enhancement due to ultrasonic vibrations during laser surface irradiation slows the heating of the specimen, precluding the possibility of surface melting within the laser irradiation time of 0.30 s. For the given frequency of 20 kHz, the convection enhancement is expected to be increasingly larger by increasing the vibration power output from 20% through 40%. The laser processing is often used for surface heat treatment of materials; the potential application of ultrasonic vibrations during such heat treatments must take into account the changes in overall heat transfer and resultant microstructural or phase transformations.

Laser surface processing for irradiation time of 0.45 s

To investigate the possibility of laser surface melting with the application of ultrasonic vibrations, the experiments were conducted with laser irradiation time of 0.35 s and 0.45 s. It was considered that, even with the enhanced surface convection, these laser irradiation times would be sufficiently longer to raise the surface temperature above melting point ($\sim$1375 ° C) of the steel samples. Detailed discussion on the development of surface microstructure with and without application of ultrasonic vibrations for the laser irradiation time of 0.45 s is presented here.

Microstructure development without ultrasonic vibrations

The surface and cross sectional SEM micrographs for the laser irradiated steel sample without the application of ultrasonic vibrations are presented in Fig.5.2. As with the

previous case (irradiation time of 0.30 s), the sample irradiated with 0.45 s shows a distinct heat affected region with a diameter of about 2 mm with surface melting at the center and HAZ around the laser melted surface (Fig.5.2(a)). The width and depth of the melting increased significantly with increasing laser irradiation time from 0.30 to 0.45 s. The width and depth of the laser melted region for the samples laser irradiated for 0.45 s were about 1700 μm and 270 μm, respectively (Fig.5.2(b)). The high magnification cross sectional SEM micrographs of the sample laser irradiated for 0.45 s without the application of ultrasonic vibrations are presented in Fig.5.3. The base material exhibited well defined austenite grains with average grain size of 7-9 μm typical of AISI 316 stainless steel.

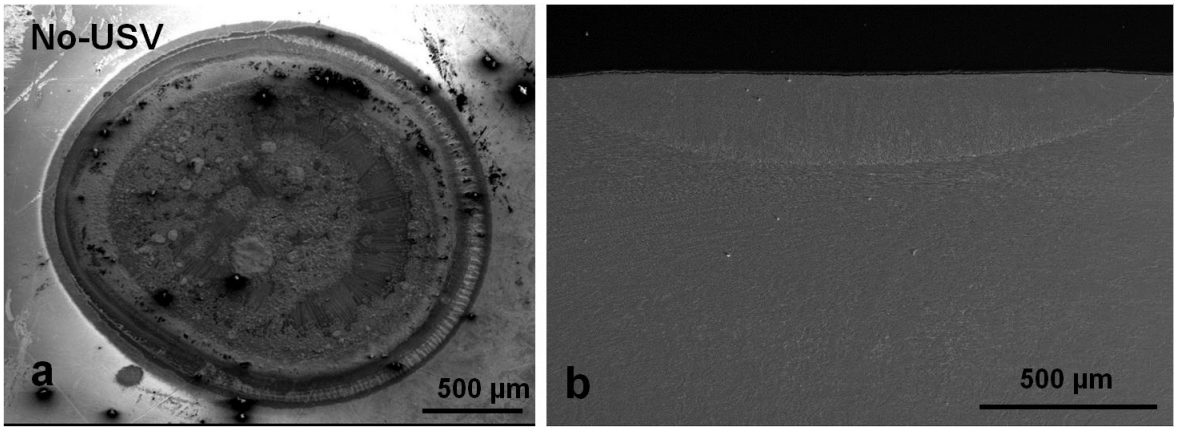

Figure 4.2: (a) Surface and (b) cross-sectional micrographs of steel sample laser irradiated for 0.45 s without ultrasonic vibrations

The laser melted (fusion) region showed two distinct zones: the columnar dendritic grains growing perpendicular to the interface towards the center of the resolidified melt pool and the equiaxed dendritic grains at the center of the resolidified melt pool (Fig.5.3(a)). The columnar dendritic grains appear to be growing from the partially melted austenite grains of the substrate (Fig.5.3(b)). The packets of columnar dendrites growing in same direction form grains with characteristic substructure (Fig.5.3(c)). The average dendritic arm spacing in these grains was about

2.2 μm. The equiaxed dendritic grains at the center of the resolidified melt pool had the average grain size of about 3-5 μm (Fig.5.3(d)). Several mechanisms such as grain detachment, dendrite fragmentation, and heterogeneous nucleation are cited for the formation of equiaxed grains during solidification of castings. During rapid directional solidification encountered in stationary (not moving) laser processing of multi-component alloys, solute pile up ahead of the solid-liquid interface and results in sufficient constitutional undercooling. The observed equiaxed dendritic grains seems to have been formed by homogeneous nucleation in the undercooled melt, and these nuclei grow in different directions taking well defined grain-like morphology. Clearly, there was an indication of columnar dendritic to equiaxed dendritic transition towards the center of the resolidified melt pool. The evolution of dendritic grain morphology is governed by local solidification conditions defined by temperature gradient and solidification or growth rate. The transition from columnar dendritic to equiaxed dendritic towards the center of the resolidified melt pool is widely reported for the laser processing of materials [61]. It has also been observed that the region extending about 50 μm into the base material near the fusion interface exhibited typical ditch structure indicative of sensitization of the steel in the HAZ (Fig.5.3(b)). The ditch structure is characterized by the presence of darker grain boundaries due to intergranular corrosion associated with the precipitation of chromium-rich carbides at the grain boundaries and the depletion of chromium in the adjacent regions [62, 63]. Fig.5.4 presents the XRD patterns for the base material and laser surface melted samples with and without the application of ultrasonic vibrations. The base material shows characteristic peaks of austenite phase. The sample laser melted without the application of ultrasonic vibrations also shows similar peaks, but the (220) peak emerges as the strongest peak indicating development of crystallographic texture consistent with the dendritic grain structure observed in the SEM micrographs.

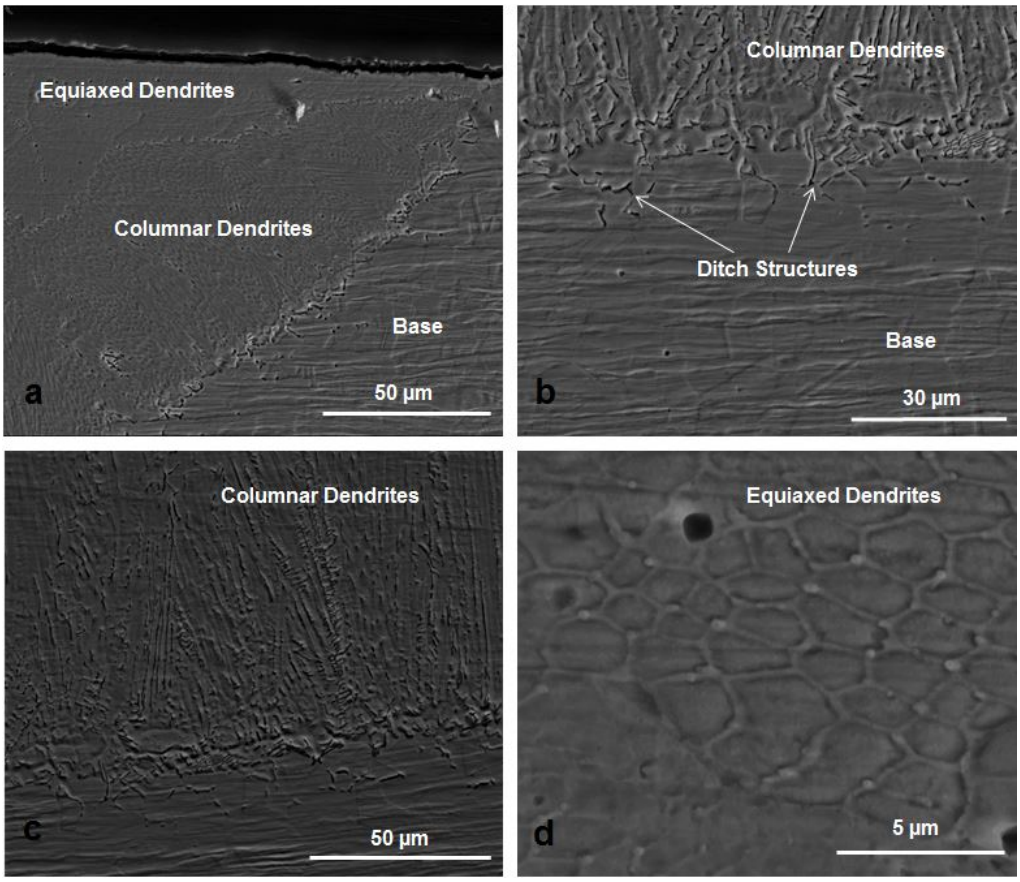

Figure 4.3: Cross sectional SEM micrographs of steel sample laser irradiated for 0.45 s without ultrasonic vibrations: (a) base, columnar dendritic, and equiaxed dendritic regions in fusion zone, (b) high magnification columnar dendritic grains and ditch structure near interface, (c) columnar dendritic grains, and (d) high magnification equiaxed dendritic grains

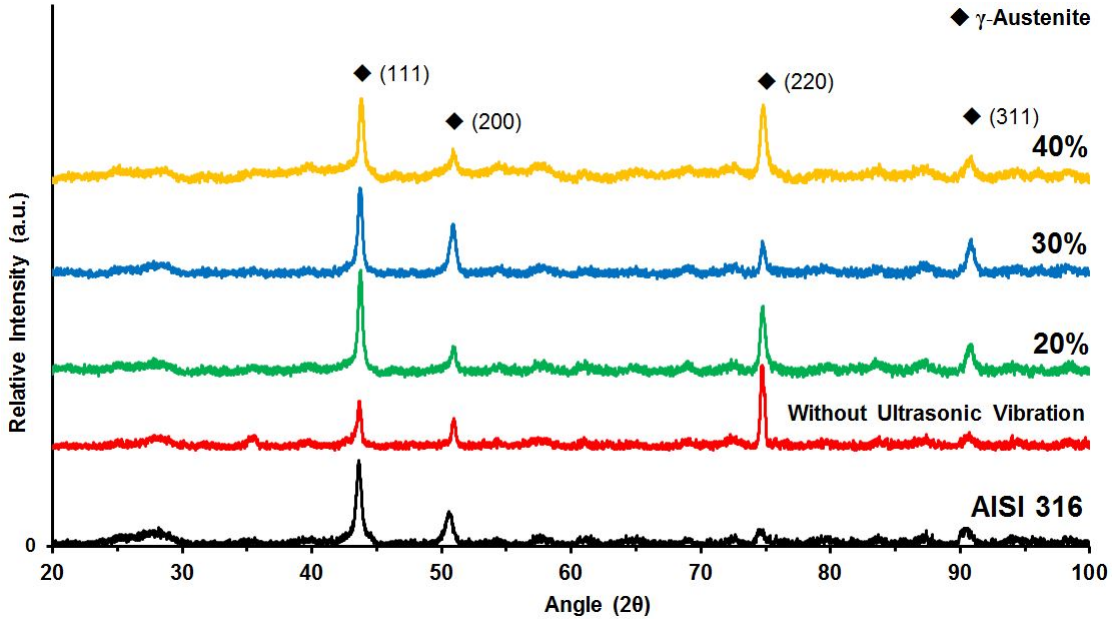

Figure 4.4: XRD patterns of untreated/base AISI 316 steel sample, and samples laser melted without and with ultrasonic vibrations for power outputs of 20 %, 30%, and 40% (laser irradiation time of 0.45 s)

Microstructure development with ultrasonic vibrations

The surface melting was observed for the laser irradiation time of 0.45 s with the simultaneous application of ultrasonic vibrations. However, the morphology and microstructure of the solidified surface layer was significantly modified when compared to the case where no vibrations were applied. Fig.5.5 presents the SEM surface and cross-sectional SEM micrographs for the samples laser irradiated for 0.45 s with the application of ultrasonic vibrations of given power output levels. All the samples showed deep craters (blind holes) of resolidified material with a build-up of material around the rims of the craters (Fig.5.6(a-b)). It appears that once the surface is melted, the ultrasonic vibrations quickly displace the molten film forming the deep crater at the laser irradiated surface. As discussed earlier, the ultrasonic vibrations enhance the surface convection and delay surface heating due to laser irradiation. No melting was observed for the laser irradiation time of 0.30 s with the application of

ultrasonic vibrations. Hence, it appears that the surface melting and rapid displacement of the melt happen in the last 0.15 s of 0.45 s irradiation time. It is important to note that the absorption of laser radiation after surface melting is significantly influenced by the dynamics of the melt film at the surface [64]. In the case of laser melting with ultrasonic vibrations, the displacement of melt film creates a favorable situation for laser absorption. The mechanisms of enhanced laser absorption are similar to the internal reflections in the keyhole during laser welding [65]. The enhanced absorption of laser radiation in the crater is likely the reason for rapid surface melting and displacement of molten film in the later stage of the irradiations time of 0.45 s. The surface micrographs (Fig.5.5) also show resolidified droplets (spatter) due to ejection of melt with the application of ultrasonic vibrations. For the given laser irradiation time (0.45 s), the diameter of the surface craters was not significantly varied with increasing ultrasonic power output and remained at about 1.3-1.5 mm. Fig.5.5 also shows images from the surfaces of the craters observed with the various ultrasonic power outputs. All the samples showed thin resolidified film in the craters (Fig.5.5).

The variation of resolidified melt film thickness with ultrasonic power output is shown in Fig.5.6. It can be observed that the resolidified melt film thickness decreases with increasing ultrasonic power output. Clearly, the ultrasonic vibrations of higher amplitude for a given frequency are more effective in displacing the laser melted surface film. A cross sectional SEM image of a crater and high magnification images of the resolidified film in the crater observed for the ultrasonic power output of 20% are shown in Fig.5.7. The cross sectional image shows the tapered crater with the depth of about 320 μm. The build-up of the material around the rim of the crater is also visible in the cross sectional image (Fig.5.7(a)). The high magnification images show that the thin film is also resolidified on the surface of the crater. The thickness of the resolidified film varies with the position on the crater. The film is thinnest (about 16 μm) at the bottom surface (at highest depth) and thickest (about 25 μm)

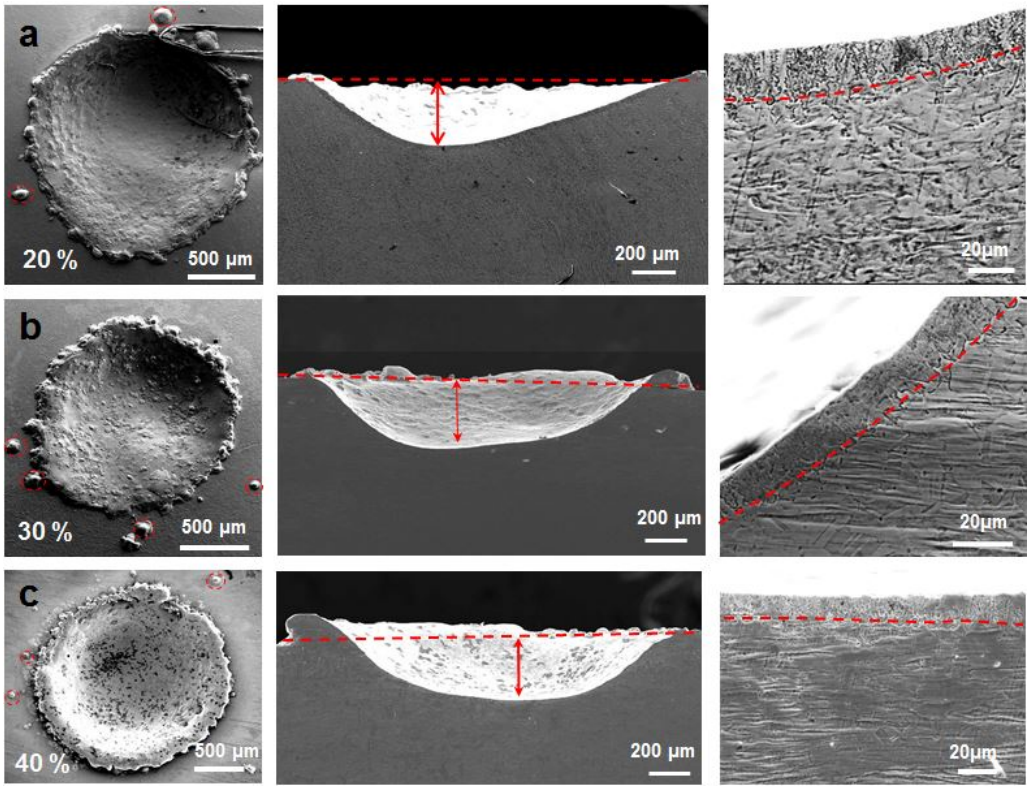

Figure 4.5: SEM images showing surfaces of craters, depths of craters, and resolidified films on the crater surfaces for ultrasonic vibration-assisted laser surface melted steel samples at ultrasonic power outputs of: (a) 20 %, (b) 30%, and (c) 40% (laser irradiation of 0.45 s)

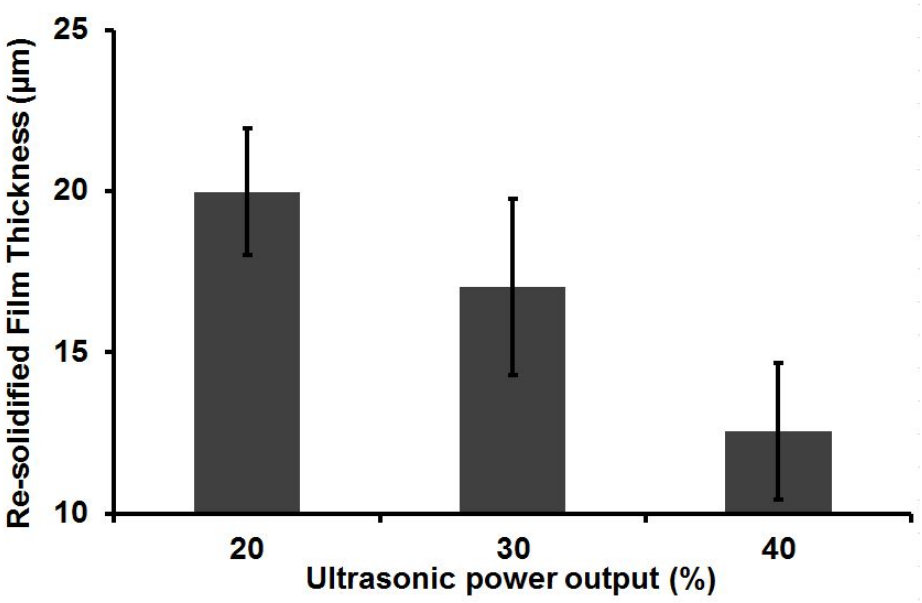

Figure 4.6: Variation of resolidified melt film thickness with ultrasonic power output (laser irradiation time of 0.45 s)

at the tapered walls of the crater, indicating vertical flow of molten material during laser melting with the assistance of ultrasonic vibrations (Fig.5.7(b-d)). The flow of molten material modifies the grain structure in the resolidified film (Fig.5.7). The solidification appears to start with the partial melting of grains in substrate.

However, the predominantly columnar dendritic structure similar to that as observed for laser surface melting without ultrasonic vibrations is absent in the resolidified melt film of the crater. The microstructure in the resolidified melt film consists of predominantly equiaxed dendritic or short fragmented grains with grain size of 1.6 μm. It is important to note that ultrasonic vibrations and mechanical stirring have long been used in the casting technologies for the grain refinement in the fusion zone [66]. It is often proposed that the mechanical forces fragment the tips of columnar dendritic grains and the convection brings them in undercooled melt where they grow as equiaxed dendritic grains [67]. It appears that formation of predominantly equiaxed grains in the resolidified film during ultrasonic vibration-assisted laser sur-

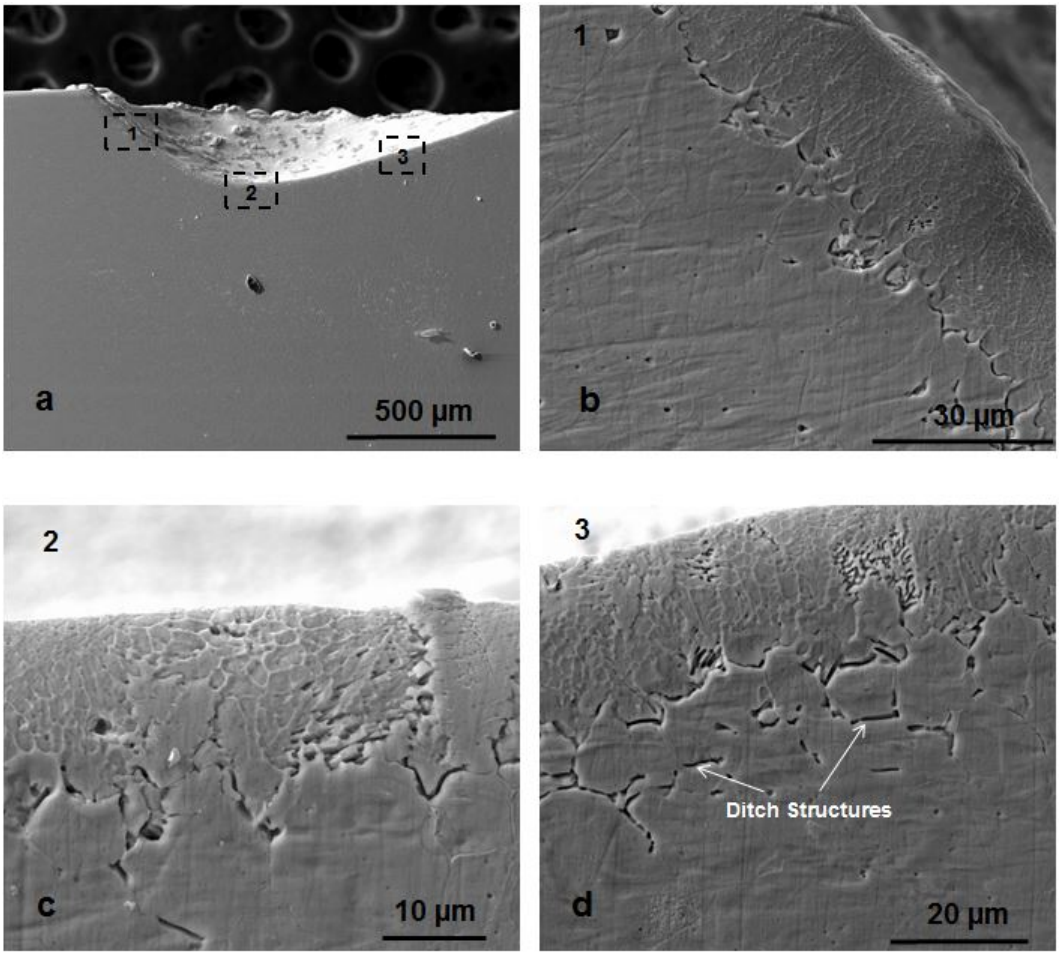

Figure 4.7: High magnification SEM micrographs showing the microstructure of resolidified melt film at different locations on the crater formed by ultrasonic vibration-assisted laser surface melting of steel sample at ultrasonic power output of 20% (laser irradiation time of 0.45 s)

face melting is most likely due to rapid dendritic fragmentation. The XRD patterns of the samples laser melted with simultaneous application of ultrasonic vibrations are also presented in Fig.5.4. These XRD patterns show stronger (220) peak compared to the base material, indicating the development of crystallographic texture due to formation of dendritic grains. However, this crystallographic texture is relatively weaker compared to the samples laser melted without the application of ultrasonic vibrations strengthening the argument that the ultrasonic vibrations cause the fragmentation of dendritic grains. The samples laser surface melted with the application of ultrasonic vibrations also show the characteristic ditch structure in the HAZ observed for the case without ultrasonic vibration assistance. Similar observations of the formation of crater and resolidified film, and the development of equiaxed grain structure in the film were made for the ultrasonic vibration-assisted laser surface melting with the irradiation time of 0.35 s.

The variations of diameter and depth of craters observed for ultrasonic vibration-assisted laser surface melting with the ultrasonic power output for the laser irradiation times of 0.35 and 0.45 s are presented in Fig.5.8. For the irradiation time of 0.45 s, the diameter of crater was in the range of about 1.3-1.5 mm and not much change in the diameter was observed with increasing ultrasonic power output. A slight decrease in crater diameter was observed for the irradiation time of 0.35 s. The depth of crater also decreased with increasing ultrasonic power output; however, the effect was much more pronounced for the irradiation time of 0.35 s. The results of observed diameter and depth of craters for the different processing conditions are also summarized in 4.1.

As observed earlier, the ultrasonic vibrations of higher power outputs are more effective in expelling the melt film as observed from thinner resolidified surface layers (Fig.5.6). While the melt expulsion is effective at higher vibration amplitudes, the extended delay in surface heating and melting associated with the enhanced surface

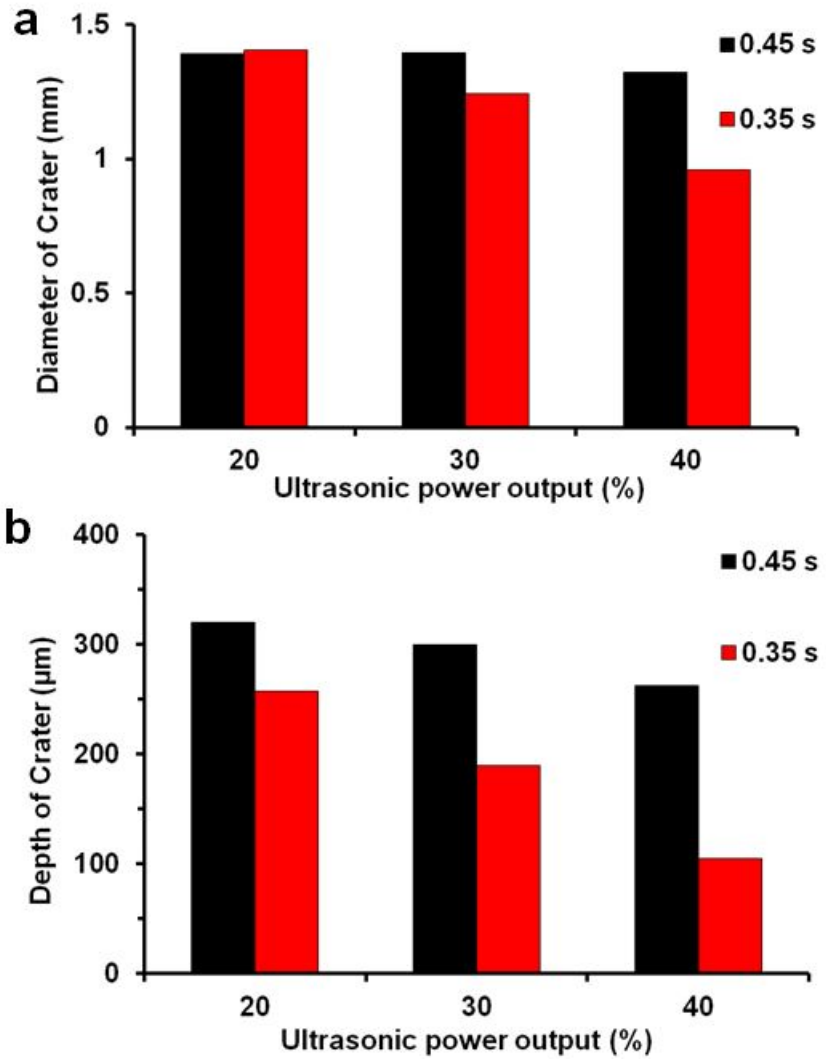

Figure 4.8: Variation of (a) diameter and (b) depth of craters for ultrasonic vibration-assisted laser surface melting with ultrasonic power output for irradiation times of 0.35 and 0.45 s

Table 4.1: Processing parameters and observed crater dimensions for ultrasonic vibration-assisted laser surface processing.

Exp.	Laser power (W)	Vibration frequency (kHz)	Irradiation time (s)	Power output (%) /Displacement (μm)	Diameter of the crater (mm)	Depth of the crater (μm)
Set 1	900	20	0.45	20/23	1.393	320
				30/37	1.396	300
				40/51	1.324	262
Set 2			0.35	20/23	1.406	257
				30/37	1.242	190
				40/51	0.960	105
Set 3			0.3	20/23	-	-
				30/37	-	-
				40/51	-	-

convection effects results in smaller depth of craters for the given laser irradiation time and ultrasonic vibration frequency. The schematic of the evolution of depth of melting (without ultrasonic vibrations) and crater (with ultrasonic vibrations) as a function of laser irradiation time is presented in Fig.5.9. The figure shows the formation of undistorted melt pool even for short laser irradiation time during laser surface melting without ultrasonic vibrations (Fig.5.9(a)). For the similar irradiation time, the convection enhancement due to ultrasonic vibrations slows the surface heating and precludes the possibility of surface melting (Fig.5.9(b)). The surface melting can be initiated in the ultrasonic vibrations case for longer laser irradiation time (Fig.5.9(c)). This laser irradiation time is sufficient to initiate surface melting even with slow heating rate. The molten layer is expelled due to ultrasonic vibrations forming a crater with a resolidified surface film. An increase in ultrasonic power out-

put for these conditions (longer irradiation time) further delays surface heating and melting forming a smaller crater even though the melt expulsion is more effective at higher vibration amplitude. While the exact mechanisms of melt expulsion during the ultrasonic vibration-assisted laser surface melting are not clear, it appears that the mechanisms are similar to those observed during early stages of ultrasonic atomization. In ultrasonic atomization, a uniform thickness layer of low viscosity liquids (water, oil etc.) is vibrated on the surfaces of the ultrasonic probes [68]. When sufficient ultrasonic energy is imparted to the fluid, capillary waves are formed on the liquid surface leading to eventual breaking (ejection) of droplets from the tips of these waves.

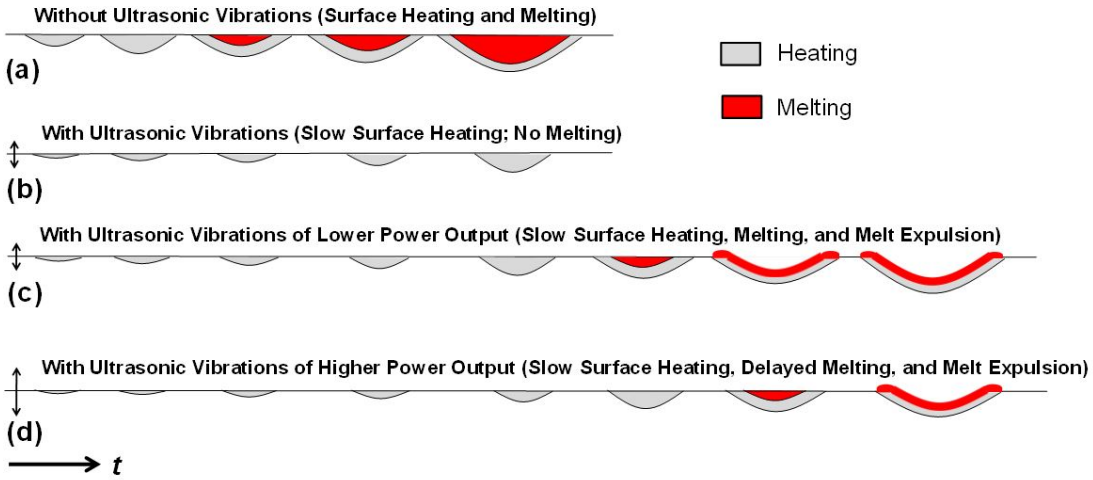

Figure 4.9: Schematics showing: (a) evolution of depth of laser melted pool without ultrasonic vibrations for shorter irradiation time; (b) laser surface heating with ultrasonic vibrations for shorter irradiation time; (c) laser surface melting and melt expulsion with ultrasonic vibrations for longer irradiation time; and (d) laser surface melting and melt expulsion with ultrasonic vibrations of higher amplitude for longer irradiation time

Significant progress has been made towards predicting the wavelength of capillary waves and the droplet size based on thickness of liquid layer, liquid material thermo-

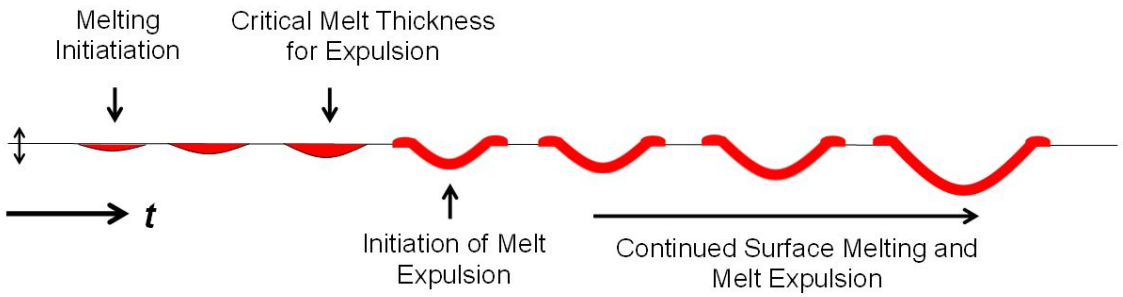

Figure 4.10: Schematics showing stages leading to formation of a crater during ultrasonic vibration-assisted laser surface melting [63]

physical properties, and ultrasonic vibration parameters [69]. The shape of the melt pool in case of laser surface melting is semi-elliptical below the surface level of the substrate in contrast to the uniform liquid layer above the substrate surface in case of ultrasonic atomization. Furthermore, the viscosity (0.005 N.s.m^{-2}) and surface tension (1.6 N.m^{-1}) (restoring force acting against capillary forces) of liquid steel are significantly greater than for the liquids typically atomized using ultrasonic methods [70, 71]. The highly constrained physical shape of the melt pool and the limited physical properties of the molten steel appear to make nearly complete/full ejection of liquid metal highly unlikely in the case of laser surface melting with moderate ultrasonic vibration frequency used in this investigation. However, the observation of distributed spatter (resolidified droplets) on the surface of the samples indicates the existence of such a mechanism, though very weak. Instead of melt ejection, the molten material is expelled vertically outside the laser irradiated region forming surface craters. In the case of ultrasonic atomization, the thickness of liquid film determines the minimum amount of ultrasonic energy required to cause the melt ejection. For a given liquid, higher ultrasonic energy is required to eject thinner liquid film [72]. Similarly, the thickness of the resolidified film on the surfaces of the craters represents the critical thickness of the liquid metal below which it will not be possible to expel the material at the given ultrasonic power output. The observed trend

of decreasing resolidified film thickness with increasing ultrasonic output power thus indicates that thinner melt film is expelled at higher ultrasonic power output. Based on these observations, important stages in the development of crater can be outlined (Fig.5.10). During ultrasonic vibration-assisted surface processing, the melting initiates at the surface of the material and extends deeper with continued irradiation. The melt film is likely to be stable until it reaches the critical thickness for vibration induced melt expulsion. Once the melt expulsion is initiated, the surface melting and melt expulsion are expected to continue with continued laser irradiation to maintain the melt film thickness corresponding to critical thickness for melt expulsion. Clearly, the simultaneous application of ultrasonic vibrations during laser surface melting resulted in expulsion of melt (forming craters) and modification of microstructure of the resolidified surface film (columnar to equiaxed dendritic transition). The melt expulsion is the important mechanism during most of the laser machining processes, while the equiaxed microstructure is often a desirable microstructure for the laser surface modification processes. The results presented in this study suggest that application of ultrasonic vibrations during laser processing presents a great potential for improving material removal during laser machining processes and for improving the microstructure during laser surface melting processes. However, the application of ultrasonic vibrations delays the interaction of laser with material due to enhancement of surface convection effects. The potential utilization of such ultrasonic vibration-assisted laser processes will require longer laser irradiation time than that is needed for conventional laser processing. Also, further investigations are needed to design the ultrasonic systems for scalable processing (i.e. application of ultrasonic vibrations to the larger substrates) at the desired vibration frequency and amplitudes.

4.1.4 Conclusion

In this study ultrasonic vibration-assisted laser surface melting of austenitic stainless steel (AISI 316) is reported. The simultaneous application of ultrasonic vibrations (20 kHz) during laser surface processing appears to delay the interaction of laser with material due to enhancement of surface convection effects. For shorter laser irradiation time (0.3 s), only heating was observed for the ultrasonic vibration-assisted laser surface processing, while the samples showed well defined resolidified melt pool without the application of ultrasonic vibrations. For the longer laser irradiation time (0.35-0.45 s), surface melting was also observed for the ultrasonic vibration-assisted laser surface processing. The application of ultrasonic vibrations resulted in expulsion of melt from the laser irradiated surface, forming well defined craters having resoldified surface films. It also resulted in transition from columnar to equiaxed dendritic grain structure and breaking of stronger crystallographic texture in the resolidified melt films. For the given ultrasonic vibration frequency (20 kHz) and laser irradiation time (0.35-0.45 s), increasing ultrasonic power output from 20 to 40% (corresponding to increasing ultrasonic vibration amplitude) resulted in further delay in laser surface melting, forming shallower and smaller surface craters. However, the melt expulsion appears to be more effective at higher ultrasonic power outputs as observed from thinner resolidified melt films. These results are likely to be useful in designing ultrasonic vibration-assisted laser processing for efficient material removal (laser machining) and improved equiaxed microstructure (laser surface modifications).

4.2 Ultrasonic vibration-assisted laser surface drilling

4.2.1 Preliminary study on ultrasonic vibration-assisted laser surface drilling

Introduction

Laser drilling is one of the most commonly used micromachining processes for creating high quality and high aspect-ratio holes in a range of materials including high performance alloys, ceramics, and composites [9, 14]. The laser drilling process offers several advantages such as non-contact processing, excellent reproducibility, and high production rates (up to 100 holes/s). Most of the laser drilling approaches such as single pulse drilling and percussion drilling involve pulsed laser irradiation of the material substrates. The laser irradiation causes substrate melting and evaporation at the melt surface [12]. The resultant evaporation-induced recoil pressure expels the melt radially outside the hole. The melt expulsion is recognized as the most efficient material removal mechanism at the lower laser powers [73, 74]. In most of the laser drilling applications, coaxial assist gases are used to facilitate the melt expulsion, protect the surface oxidation, and shield the focusing lens [24]. Contrary to intuition, however, the increase in assist gas pressures actually increases the laser drilling time at all laser power levels [28, 29]. It has been reported that the high gas pressures form the density gradient fields and change the refractive index of the medium, resulting in defocusing of the laser beam (and hence lower energy density). In addition the high efficiency of materials removal (ablation or melt expulsion), it is important that the laser drilled holes have excellent metallurgical and geometric quality. For example, the laser drilled holes are often associated with taper, and the taper angle depends on the thickness of the work-piece [32]. Significant efforts have been made to optimize the laser focusing conditions to minimize taper of the drilled holes. It has been reported that best quality holes in terms of straightness can be obtained by positioning the laser beam waist just below the surface of the workpiece [21]. However,

the defocusing of the laser beam decreases the energy density and efficiency of laser melting/melt expulsion. Also, the laser drilling is often associated with formation of resolidified deoplets (spatter) or redeposition of ablated particles on the machined substrate surfaces. Recently, Zheng and Huang reported ultrasonic vibrations-assisted femtosecond machining of microholes in Nitinol substrates with an improvement in hole wall surface quality and higher hole aspect ratio [49]. They used femtosecond pulsed laser (Ti-Sapphire) in combination with ultrasonic vibrations (frequency: 40 kHz; amplitude: 2.5 μm) and reported that ultrasonic vibrations facilitates the removal of ablated particles by enhancing the heat transfer of the particles (i.e. better cooling of the particles, and hence, reduced tendancy of the particles to bond to the hole wall and substrate surface) [49]. In this letter, we are presenting a novel ultrasonic vibration-assisted continuous wave CO_2 laser surface drilling of austenitic stainless steel. The continuous wave laser was operated in the surface melting regime, and the ultrasonic vibrations with frequency of 20 kHz and amplitude of 20-50 μm were applied during laser surface melting to facilitate melt expulsion creating holes. Preliminary results on the effect of ultrasonic vibration amplitude on the geometric features of the holes (hole diameter/depth, aspect ratio, and taper) are presented for the ultrasonic vibration-assisted laser drilling of austenitic stainless steels.

Methods

The ultrasonic vibration-assisted laser drilling set-up consisted of a continuous wave (cw) CO_2 laser, an ultrasonic power generator, and a 13-mm diameter titanium alloy probe (horn). The laser drilling was performed on 2 mm thick AISI 316 austenitic stainless steel . The surfaces of the steel specimens were polished using SiC papers (1200 grit) followed by microcloth polishing with alumina slurry (0.5 μm particle size) to render mirror finish to the surface. The surfaces of the specimens were etched using Carpenters etchant (etching time of 20 s) to improve laser absorption. The prepared

steel samples were screwed on the horn. The laser irradiation was conducted at the laser power of 900 W (Ferranti, Manchester, UK). The 750 W ultrasonic generator created the vibrations of fixed frequency of 20 kHz at the sample surface (Sonics & Materials, Inc, Newtown, CT). The vibration displacements of 23, 37, and 51 μm were measured for the power outputs of 20, 30, and 40%, respectively. During ultrasonic assisted laser drilling, the vibrations were maintained during the entire duration of laser irradiation. A protective gas was used to prevent surface oxidation during laser drilling. A scanning electron microscope (JEOL Ltd, Tokyo, Japan) was used to characterize the microstructural features of the ultrasonic vibration-assisted laser drilled specimens.

Results and Discussion

The cross sectional SEM micrographs of the steel samples laser irradiated (irradiation time of 0.45 s) with and without simultaneous application of ultrasonic vibrations are presented in Fig.5.11. The distance from the laser head to the sample surface was 5 cm in these initial experiments. It can be seen that the laser irradiation without the application of ultrasonic vibrations results in the surface melting and formation of well defined resolidified region with depth of about 270 μm and width of about 1700 μm (Fig.5.11(a)). The laser irradiation conditions do not cause any expulsion of the melt from the surface. These conditions are generally used for laser surface modifications involving melting of the substrates. For the similar laser irradiation conditions, the simultaneous application of ultrasonic vibrations results in the formation of deep craters (blind holes) on the surface (Fig.5.11(b-c)). Clearly, the application ultrasonic vibrations during laser surface melting facilitate the melt expulsion from the surface. The build-up of expelled material around the rim of the blind holes can be clearly seen in the SEM micrographs. The height of the build-up material increases with increasing ultrasonic power output. The depths of blind holes (measured from the base surface of

the sample) were about 320 μm, 310 μm, and 270 μm for the ultrasonic power outputs of 20%, 30%, and 40%, respectively. While the depth of surface holes decreases with increasing ultrasonic power output corresponding to increasing vibration amplitudes, the holes become increasingly wider.

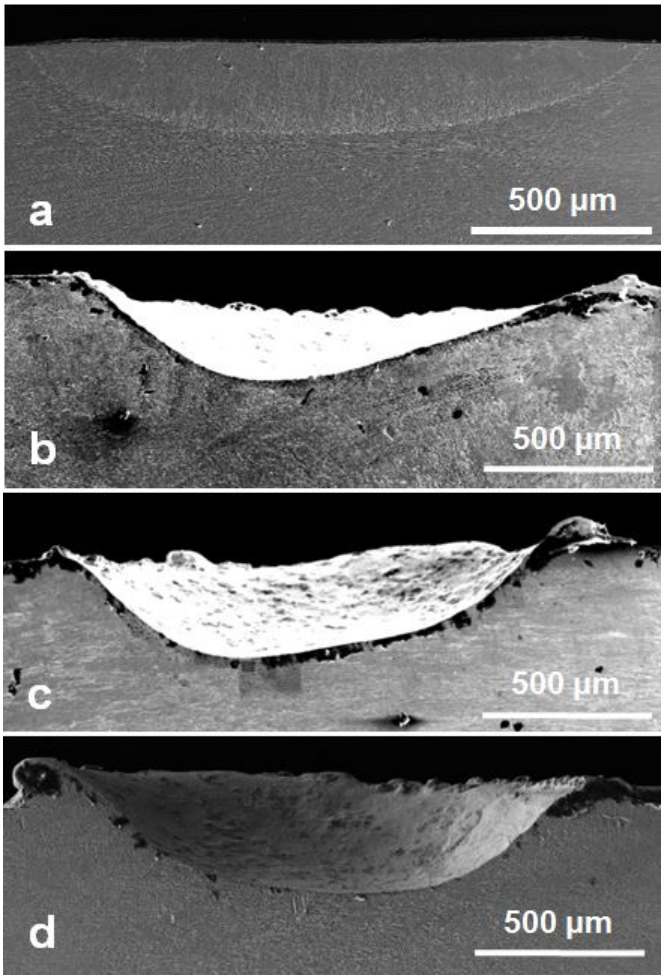

Figure 4.11: Cross-sectional micrographs of steel specimens laser irradiated for 0.45 s: (a) without application of ultrasonic vibrations; (b, c, and d) with simultaneous application of ultrasonic vibrations at power outputs of 20%, 30%, and 40%, respectively (laser power: 900 W; laser head to sample distance: 5 cm)

The observation of heavy material build-up and wider (but shallower) holes indicate efficient expulsion of the melt at higher ultrasonic power outputs. It has been widely reported that ultrasonic vibrations enhance the convective heat transfer at

the surface [57]. For the given frequency (20 kHz), the convective heat loss at the laser irradiated surface is likely to be higher for higher ultrasonic power output (and vibration amplitudes), resulting is delayed surface melting. It appears that while the ultrasonic vibrations of higher amplitudes are more efficient in expulsion of the melt, the delayed surface melting results in overall decrease in hole depth with increasing ultrasonic vibration amplitudes. It was observed that the higher aspect ratio holes could be drilled by perfoming the processing at lower laser head to sample distance. Fig.5.12 shows the surface and corresponding cross sectional images of the ultrasonic vibration-assisted laser drilled holes in steel for the laser irradiation time of 0.4 s (distance between laser head and surface of the sample was reduced to 1.5 cm).

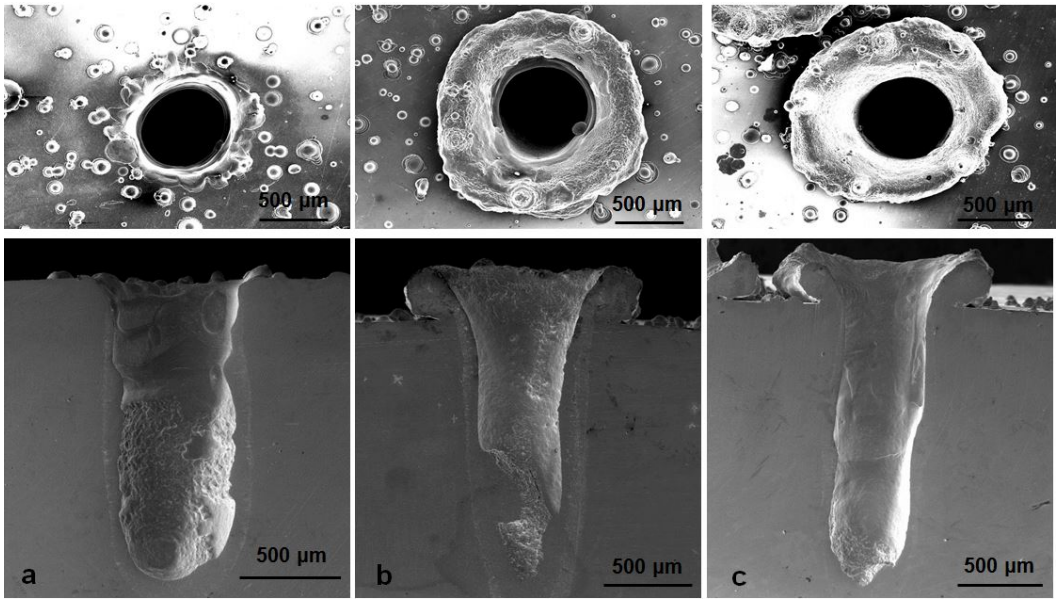

Figure 4.12: Surface and corresponding cross sectional micrographs of ultrasonic vibration-assisted laser drilled steel samples for ultrasonic power outputs of: (a) 20%, (b) 30%, and (c) 40% (laser power: 900 W; laser irradiation time: 0.4 s; laser head to sample distance: 1.5 cm)

It can be clearly seen that the ultrasonic vibration-assisted laser drilling produces well defined straighter holes (taper angles less than 2.5° up to 1 mm below the base surface). At lower ultrasonic power output (20%), the surface of the drilled samples

exhibited significant spatter without much material build-up at the rim. The drilled holes showed very heavy material build-up at higher ultrasonic power outputs (30% and 40%). Clearly, the application of ultrasonic vibrations during laser surface melting destabilized the melt film. It appears that the melt expulsion in the form of ejected droplets is dominant in the early stages of laser drilling followed by upward melt flow on the walls of the drilled holes. In general, the depth of the hole increased and diameter of the hole decreased (i.e. hole aspect ratio increased) with increasing ultrasonic power output (Fig.5.13). It appears that as the depth of laser drilled hole increases with increasing ultrasonic vibration amplitudes, the expelled melt resolidifies on the walls of the hole, forming high aspect ratio holes. The preliminary results presented here indicate that relatively lower power continuous wave lasers could potentially be used in combination with simultaneous application of ultrasonic vibrations for the laser drilling applications. While the ultrasonic vibration-assisted femtosecond laser machining results in cleaner surfaces due to removal of ablated debris, the materials removal mechanism during ultrasonic vibration-assisted continuous wave drilling is melt expulsion and results in formation of resolidifed droplets on the machined surfaces. The detailed analysis of the melt dynamics, drilling rates, and evolution of microstructure/defects during such ultrasonic vibration-assisted continuous wave drilling is currently under investigation.

Conclusions

A novel approach for a continuous wave CO_2 laser drilling with the simultaneous application of ultrasonic vibrations is demonstrated for the austenitic stainless steel. The ultrasonic vibrations of frequency 20 kHz and amplitudes in the range of about 20-50 μm facilitate the material removal/melt expulsion by droplet ejection and vertical flow of melt from the laser melted region, creating holes. The geometric features such as hole diameter/depth and aspect ratio of the laser drilled holes are greatly

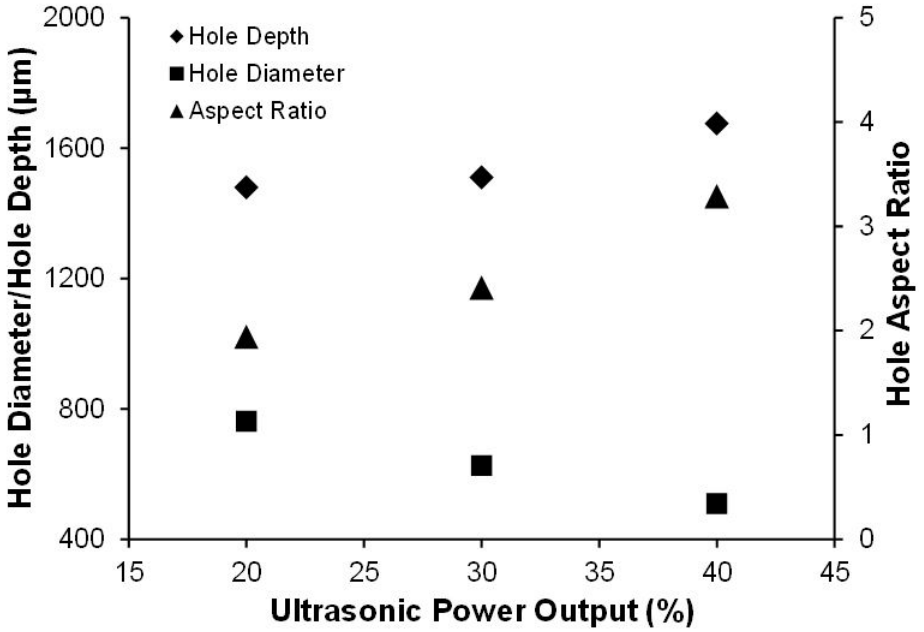

Figure 4.13: Variation of hole diameter, depth, and aspect ratio with ultrasonic power output (laser power: 900 W; laser irradiation time: 0.4 s; laser head to sample distance: 1.5 cm)

influenced by the power output (vibration amplitude) of the applied ultrasonic vibrations. For the similar laser processing parameters (power, irradiation time, and focusing distance), higher ultrasonic power outputs form higher aspect ratio holes.

4.2.2 Effect of irradiation time on hole quality and geometry in ultrasonic vibration-assisted laser surface drilling

Introduction

Pulsed laser drilling, in the laser-material interaction regime of surface melting, is commonly used for machining of 0.5-3 mm holes in a range of applications, as described in Dahotre and Harimkar [9]. The drilling of sub-1mm cooling holes in the aerospace components is one of the most of important applications of the pulsed laser drilling and is discussed by French *et al.* [75]. The laser drilling process involves irradiation of high intensity pulses that cause surface melting and evaporation at the surface of the melt film. Zhang and Faghri [76] described that while some material removal occurs by surface evaporation, the dominant mechanism of material removal remains the melt expulsion during laser drilling. Wagner [77] reported that the melt expulsion is a direct result of evaporation induced recoil pressure on the surface of the melt. When the pressure on the surface of the melt film exceeds the surface tension forces, the melt is pushed radially out, creating a hole by melt expulsion. Assist gases are often used to facilitate the melt expulsion during laser drilling. As Low *et al.* [33] discussed, the efficiency of material removal (drilling rate) and the quality of drilled holes depend on the dynamics of the melt flow during laser drilling . Significant efforts have been made to improve the material removal rates and quality of holes during laser drilling. Chen *et al.* [34] studied the effect of the peak power and the pulse format on the quality of the laser drilled holes. Low *et al.* [35] investigated the effect of assist gas (O_2, Ar, N_2, and Air) on the thickness and geometry of the surface spatter formed during laser drilling and reported a significant reduction in spatter thickness in the case of O_2 assist gas. It has also been demonstrated by Low *et al.* [36] that the material ejection processes during laser drilling can be effectively controlled by temporal pulse train modulation for improving the material removal

rate and quality of laser drilled holes. Lau *et al.* [51] and Yue *et al.* [52] also reported that the simultaneous application of ultrasonic vibrations during pulsed laser drilling improve the material removal and quality of laser drilled holes. With this approach of ultrasonic vibrations-aided pulsed laser drilling, about 20% increase in hole depth and about 30% reduction in heat affected zone were reported by Lau *et al.* [51] for aluminum matrix composites. However, even with these advances, laser drilling of large aspect-ratio holes with acceptable surface quality and reproducibility is still a challenge in adopting the technology for wider applications. Continuous wave (CW) laser surface melting, with steady state melting conditions reached at sufficiently high laser scanning velocities, results in the formation of well-defined resolidified bead on the surface. A continuous laser irradiation at a spot (i.e. stationary irradiation without scanning) on the surface also forms a well-defined melt pool, albeit with some surface rippling in some cases. These characteristics are very useful for surface modification of materials, and hence, continuous wave lasers are most appropriate for laser surface engineering applications as described in Ion [78]. The continuous wave lasers are also used in cutting applications where the assist gases expel the melt from the bottom of the cutting front/kerf. However, the use of continuous wave lasers, even with the presence of assist gases, in material drilling applications is limited. Recently, it has been observed by Alavi and Harimkar [79] that the simultaneous application of ultrasonic vibrations (20 kHz) during continuous wave CO_2 laser surface melting of stainless steel destabilizes the melt film and facilitates the melt expulsion. The melt expulsion resulted in the formation of well-defined craters with resolidified surface films. The laser surface melting experiments under the influence of ultrasonic vibrations were conducted for the laser power of 900 W, laser irradiation times in the range of 0.35-0.45 s, and the working distance (i.e. the distance between the laser head and the surface of the sample) of about 50 mm. It has also been shown that the melt expulsion, in the form of sideways melt flow and droplet ejection, initiates

when the critical melt film thickness is reached. The observation of melt expulsion during laser surface melting under the influence of ultrasonic vibrations presents a unique possibility of laser drilling with a continuous wave laser. The schematic showing the melt expulsion and hole formation during the ultrasonic vibrations-assisted continuous wave laser surface drilling is shown in Fig.5.14.

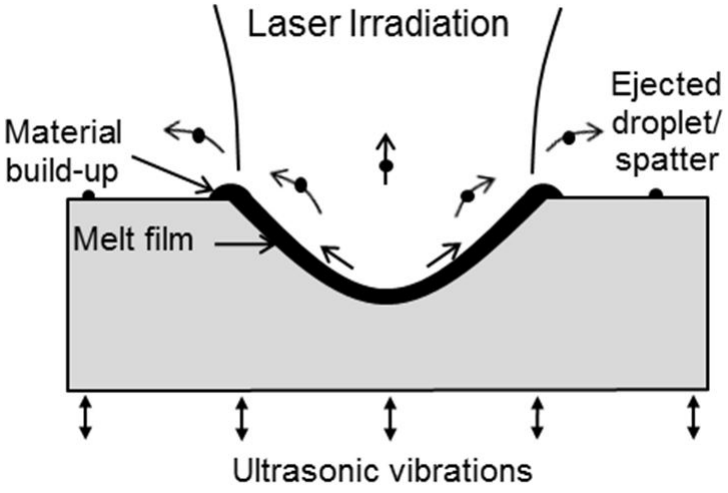

Figure 4.14: Schematic of the melt expulsion in the form of upward melt flow and droplet ejection leading to hole formation during ultrasonic vibration-assisted laser surface melting

The preliminary laser drilling experiments, reported by Alavi and Harimkar [80], have shown that the high aspect ratio holes can be drilled by reducing the working distance to about 15 mm for the similar laser processing and ultrasonic vibration parameters . It has also been observed that the ultrasonic vibration parameter, especially the vibration displacement, for the given ultrasonic frequency (20 kHz) influences the geometric parameters of the laser drilled holes. In contrast to earlier investigations by Lau *et al.* [51] and Yue *et al.* [52] where ultrasonic vibrations were simultaneous applied during pulsed laser drilling (a well-established laser drilling process in itself), the proposed ultrasonic vibration-assisted continuous wave laser drilling extends the energy-efficient laser melting (no drilling) regime for laser drilling applications and

enables continuous (instead of discontinuous pulsed) drilling of materials. Since continuous and pulsed wave laser outputs result in different laser-material interactions (primarily surface melting for continuous wave lasers; melting with extensive surface evaporation, generation of recoil pressure, and use of assist gas for pulsed lasers), direct comparison between continuous wave and pulsed laser machining/drilling is difficult. However, performing laser drilling in CW mode offers benefits related to energy/process efficiency and quality of machined surfaces. The pulsed laser drilling is performed with a very high peak power (up to 20 kW) but low pulse repetition rates with long pulse off times as described in Roos [81]. The material surface cools very fast during this pulse off time, i.e. the surface needs to reheated/remelted again during each subsequent pulse to create melt expulsion as reported by Dahotre and Harimkar [9]. In continuous wave laser drilling under the influence of ultrasonic vibrations, the material removal is primarily in melting regime and sufficiently low power (950 W in this case) continuous output is enough to facilitate melt expulsion. Furthermore, there are no off times in continuous wave laser drilling, so the melting is continuous (i.e. no intermittent cooling as in case of pulsed laser drilling) and performed in much shorter time. With efficient material removal under the influence of ultrasonic vibrations, the proposed continuous wave laser drilling is likely to offer benefits related to material removal rate and machined surface quality compared to conventional pulsed laser drilling. With the widespread use of continuous wave CO_2 lasers in industry, the proposed laser drilling approach is likely to expand the applications of these lasers for flexible manufacturing. While the preliminary studies have established the possibility of laser drilling with the proposed ultrasonic vibrations assisted-laser surface melting, it becomes important to establish the mechanisms of laser drilling under the influence of ultrasonic vibrations and investigate the evolution of geometric and quality aspects of the laser drilled holes with the laser irradiation time. In this paper, high speed photography is used to trace the sequence of pro-

cesses, leading to formation of hole with the laser surface melting under the influence of ultrasonic vibrations (laser power of 950 W, working distance of 15 mm, ultrasonic vibration frequency of 20 kHz, and vibration displacement of 23 μm). Also, the results of detailed and systematic investigations on the evolution of geometric parameters (hole diameter, depth, aspect ratio, taper angle, and material removal rate) and quality parameters (build-up material at the hole rim, recast layer thickness on the hole walls, microstructure in recast layer, and heat affected zones) with the laser irradiation time in the range of 0.05-1.25 s (for the given specific laser processing and ultrasonic vibration parameters) are presented. A two-dimensional finite element model (heat transfer) based on critical time of melt expulsion observed from high speed photography is proposed for the prediction of material removal volume during laser drilling under the influence of ultrasonic vibrations. The predictions of the laser drilled hole volumes from the heat transfer model were compared with the experimental results for the investigated laser irradiation times.

Methods

The ultrasonic vibration-assisted laser surface drilling setup consisted of a continuous wave (cw) CO_2 laser (Ferranti, Manchester, UK), a ultrasonic power supply, and a 13-mm diameter threaded titanium alloy probe/horn (Sonics & Materials, Inc, Newtown, CT). The experiments were performed on 3.5 mm thick AISI 316 stainless steel specimens. Each steel specimen, surface finished by polishing using 400 grit SiC papers followed by sand blasting, was screwed on the threaded ultrasonic probe.

The laser surface melting was performed with a laser power of 950 W and working distance of 15 mm for a range of laser irradiation times: 0.05, 0.10, 0.20, 0.25, 0.35, 0.75, and 1.25 s. The ultrasonic probe was vibrated (vibrations perpendicular to the specimen surface) with a vibration frequency of 20 kHz and vibration displacement of 23 μm (corresponding to ultrasonic power output of 20%) during laser surface

melting. The ultrasonic vibrations for this system are generated by piezoelectric lead zirconate titanate (PZT) crystals. A three-dimensional optical surface profiler (Nanovea, Irvine, CA) was used to measure the build-up volume of the material around the laser drilled hole periphery. A scanning electron microscope was used (JEOL Ltd, Tokyo, Japan) to characterize the surface and cross-sectional features of the laser drilled specimens. An image processing software, Image J, was used to measure the geometric and quality features of the laser drilled holes from the SEM micrographs. A high speed camera (X-StreamVISION; XS-4, IDT) was used to image the processes in early stages of laser drilling. To capture the illuminated droplets and melt pool (due to laser light irradiation), the exposure time was set at 22 μs, and the images were recorded with 8000 frames/s and image size of 480×320 pixels.

High speed camera photography

The preliminary studies reported earlier showed that continuous wave laser surface melting with a stationary beam resulted in the formation of well-defined resolidified regions on the surface of stainless steel samples. The simultaneous application of ultrasonic vibrations (of frequency 20 kHz) during laser surface melting resulted in the melt expulsion in the form of lateral/sideways melt flow and droplet ejection from the laser irradiated surface, forming well-defined hole. To investigate the underlying mechanisms of material removal and hole formation due to ultrasonic vibrations assisted laser melting, high speed photography images during the process were captured. The sequence of frames captured during laser surface melting with the given laser processing (950 W, 15 mm working distance) and ultrasonic vibration parameters (20 kHz, 23 μm vibration displacement) are presented in Fig.5.15. The first three frames in this figure (Fig.5.15a-c) are the adjoining frames separated by time 0.125 ms; these frames, showing the appearance of brighter spot on the surface, indicate the first signs of laser interaction with the material. With the continued laser irradiation,

the surface of the material eventually melts and forms a well-defined melt pool; the size of the melt pool increases with time (Fig.5.15d). The melt pool also shows the brighter outer rim, indicating the build-up of material due to lateral/sideways flow of material in the early stages of hole formation (Fig.5.15d-e). Eventually, the melt pool gets destabilized leading to the ejection of a droplet from the center of the melt pool (Fig.5.15e). It appears that the melt pool must reach a critical size/volume before the droplet ejection starts. Based on these high speed camera images, the droplet ejection initiates at about 2-2.125 ms after the first appearance of laser interaction with the material (i.e. appearance of the brighter spot on the surface). The brighter rim is also seen in the frames adjoining the frame showing first droplet ejection, indicating continued build-up of material at the periphery of the hole. The continued laser irradiation results in the ejection of a stream of droplets, advancing the drilling front and forming a deep hole.

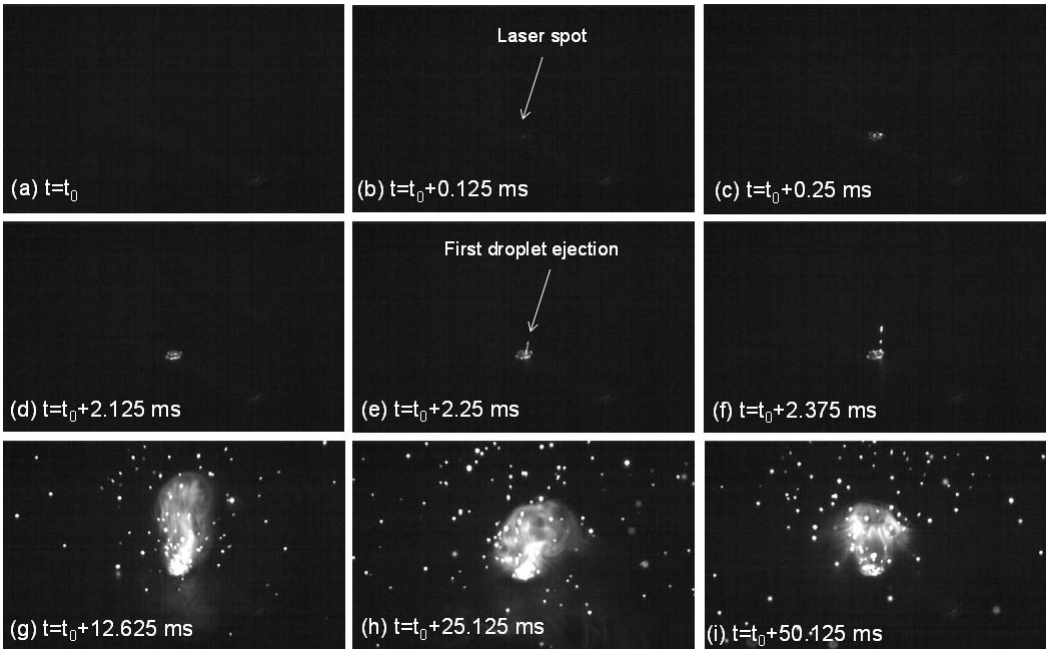

Figure 4.15: High speed camera images showing the sequence of events during hole formation with the ultrasonic vibration-assisted laser surface melting

The angular trajectory of the ejected droplets can also be traced from the high

speed camera images. In the early stages of drilling when the hole is shallow, the droplets are ejected in over a wider range of angular distribution. For the total laser irradiation time of 0.25 s, it was observed that the trajectory angles of the ejected droplets were 57°, 20°, 7.5°, and 6.5° at times of 12.5, 100, 196.75, and 250 ms, respectively.

Geometric aspects

SEM micrographs from the surface and cross-sections of the holes laser drilled with increasing laser irradiation time (0.05 to 1.25 s) using the ultrasonic vibration-assisted laser surface melting are presented in Fig.5.16. For the laser irradiation times up to 0.35 s, it can be seen that the laser drilled holes are well defined with very good circularity and straightness (Fig.5.16(a-e)). It appears that the material removal by droplet ejection is much more uniform for shorter irradiation times. To investigate the possibilities of drilling deeper holes, the experiments were also conducted for longer irradiation times of 0.75 and 1.25 s. The SEM images from the surfaces of the holes drilled using these laser irradiation times also showed very good circularity at the surface (Fig.5.16(f-g)). The cross sectional images indicate that deeper holes were actually formed with longer irradiation times, but the resolidification of the ejected droplets closes the holes giving lower effective depths. The SEM micrograph from 0.75 s shows that the hole is first closed just above the bottom of the hole (Fig.5.16(f)). The continued laser irradiation causes further droplet ejection (probably from the resolidified region above the bottom of the hole) and solidification on the walls giving non-uniform hole diameter along the depth of the hole. The narrowing of the hole due to resolidification of droplets on the wall can be clearly seen for the sample with laser irradiated with 0.75 s. The hole closing at multiple locations along the depth can happen for longer laser irradiation times, as shown in Fig.5.16(g) for the laser irradiation time of 1.25 s. It has been reported that in the conventional laser drilling

also the molten material can be expelled out effectively in some cases and results in closed hole formation. It has been proposed that an extra assist gas pressure at the final stage of the drilling ejects the remaining molten material out of the hole, as described by [24]. The variation of diameter (at the surface) and depth of the laser drilled holes with laser irradiation time is presented in Fig.5.17(a). The hole diameter at the surface increases slowly, but nearly linearly, with increasing laser irradiation time.

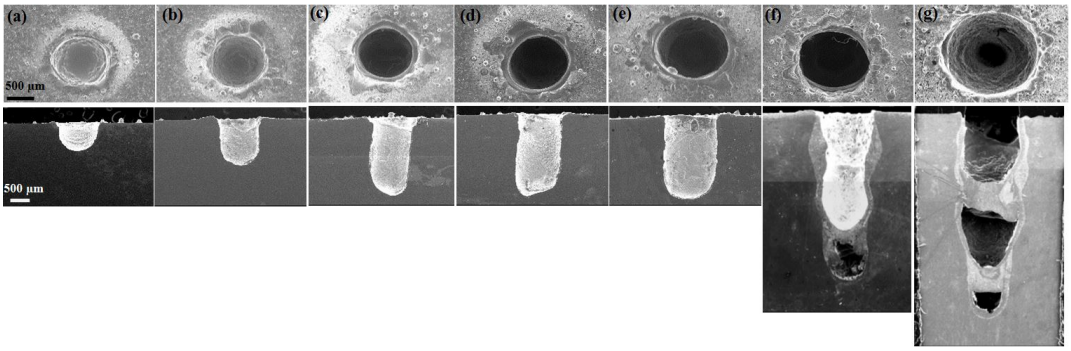

Figure 4.16: SEM images from the surface and cross-sections of the laser drilled holes for laser irradiation times of: (a) 0.05 s, (b) 0.1 s, (c) 0.2 s, (d) 0.25 s, (e) 0.35 s, (f) 0.75 s, and (g) 1.25 s. (laser processing parameters: 950 W power and 15 mm working distance; ultrasonic vibration parameters: 20 kHz frequency and 23 μm vibration displacement)

The initial diameter of the hole is determined by the critical volume of melt for the droplet ejection under the influence of ultrasonic vibrations. After the initiation of droplet ejection, the melt front will continue to advance down the hole with continued laser irradiation. The sides of the holes can still melt due to irradiation with trailing edges of energy distribution in the laser beam, increasing the hole diameter with increasing laser irradiation time. For the investigated laser processing and ultrasonic vibration parameters, the hole diameter in the range of about 1.25-1.75 mm was observed. The depth of the laser drilled hole increases with increasing laser irradiation time. Note that the shortest laser irradiation time investigated in this study was 0.05

s. The high speed camera images showed that the melt pool remains stable for 2.125 ms, indicating that the no hole condition exists for the shorter duration of laser irradiation time. The hole depth increases nearly linearly at a very high rate (drilling rate in mm/s) up to the laser irradiation time of about 0.2-0.25 s. The drilling rate then progressively slows down with further increase in laser irradiation time. Similar trend was also observed for the mass loss, which corresponds to the material removed in the laser drilling process (Fig.5.17(b)). The calculated volumetric material removal rate as a function of laser irradiation time is also plotted in Fig.5.17(b). Clearly, the material removal rate decreases almost linearly with increasing laser irradiation time. The drilling rate or the material removal rate during laser surface melting under the simultaneous influence of ultrasonic vibrations is directly linked with the droplet ejection during the process. It appears that, for shallow holes formed with shorter laser irradiation times, the droplets are ejected in all the directions. The high speed camera images showed that the angular trajectory of the droplet ejection extends over a large angle. As the hole depth increases, the distribution of the angular trajectory of the droplets ejected from the bottom of the hole is limited by the geometry of the deep holes. For deeper holes, only the droplets ejected nearly vertically escape from the holes contributing to the material removal. The droplets ejected at an angle impinge on the side walls and resolidify, causing local narrowing of the hole along the depth as observed from the SEM images. The sideways ejection of the droplets does not contribute to the material removal, slowing down the drilling rate. With the investigated laser processing and ultrasonic vibration parameters, straight holes with diameter of 1.25-1.75 mm and depth up to about 2-2.5 mm can be easily drilled in stainless steel. The deeper holes with the depth of about 4-5 mm drilled with the similar processing parameters, but longer laser irradiation times, were associated with closed cavities along the hole depth due to resolidification of expelled melt. It seems that higher intensity ultrasonic vibrations (higher vibration displacement and

frequency) are likely to facilitate efficient vertical ejection of the melt droplets for drilling deeper holes. It is worth mentioning that the maximum material removal rate in ultrasonic vibration-assisted laser drilling (∼450 mm^3/min) is significantly higher than that observed with conventional laser drilling (100 mm^3/min) as mentioned by Ion [78].

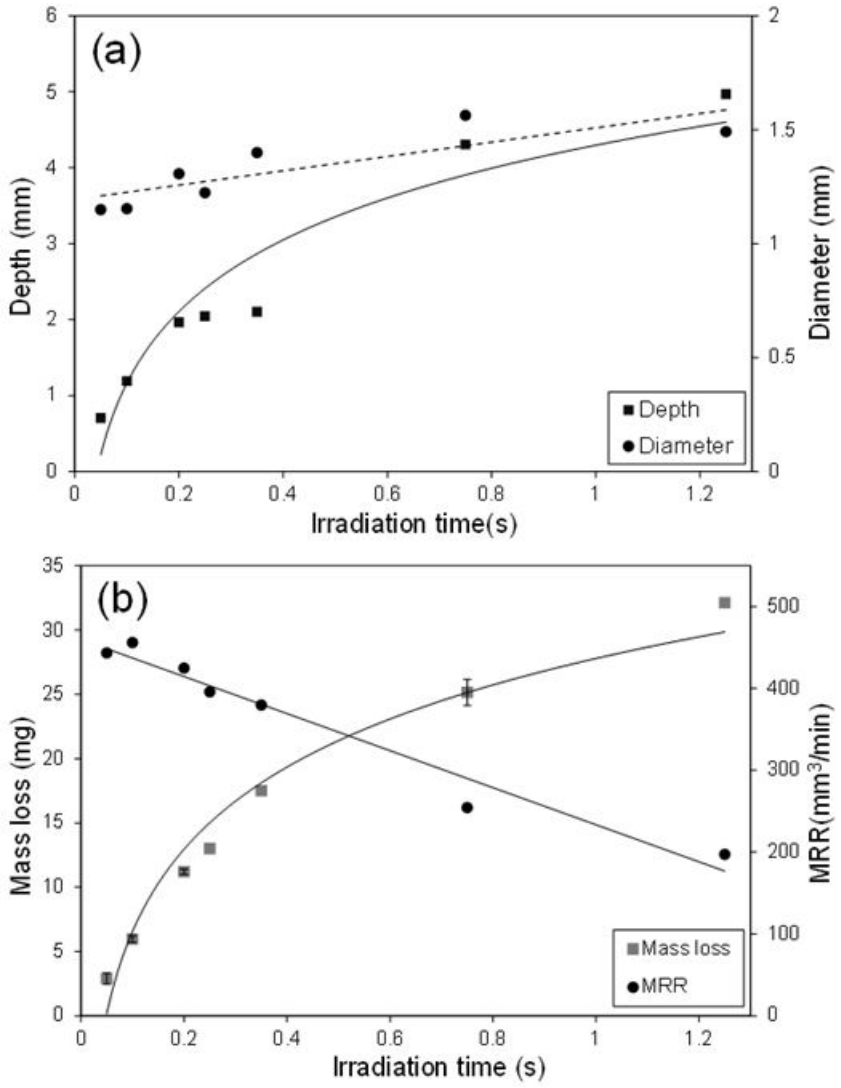

Figure 4.17: (a)Variation of depth and diameter of the laser drilled holes, and (b) variation of mass loss and material removal rate (MRR) with laser irradiation time for the ultrasonic vibration-assisted laser drilling

The variation of hole aspect ratio and taper angle with laser irradiation time is

plotted in Fig.5.18(a). The hole aspect ratio increases with increasing laser irradiation corresponding to increasing depth of the hole. The hole aspect ratio was about 1.5 for the straight holes drilled with the laser irradiation time up to 0.35 s. The higher aspect ratio of 2.5-3.5 was observed for the deeper holes drilled with laser irradiation time of 0.75-1.25 s; note that these holes exhibited closed cavities as discussed earlier. The hole taper angle was calculated as follows:

$$Holetaperangle(degree) = \frac{d_i - d_0}{2t_h} \times \frac{180}{2\pi} \tag{4.2}$$

where d_i is the diameter of the hole at the entrance, do is the diameter of the hole at 200 μm from bottom of the hole, and t_h is the depth of the hole. The taper angle of the holes decreases with increasing laser irradiation time (i.e. with increasing depth of the holes). The taper angle is very high for shallow holes, but decreases to about 2-4° at intermediate laser irradiation time. Even though the deeper holes (drilled with laser irradiation time of 0.75-1.25 s) showed very low calculated taper angle, the hole diameter is not uniform along the depth and the holes exhibited closed cavities along the depth. The general trend of decreasing hole taper with depth/thickness is also observed for conventional pulsed laser drilling, as described by Yeo *et al.* [21].

Quality aspects

The SEM micrographs presented in Fig.5.16 also show that holes laser drilled with the ultrasonic vibration-assisted laser surface melting are associated with typical defects of laser drilling. These micrographs show distinct material build-up near the rim of the holes, spatter on the surface, heat affected zones, and recast layer on the walls of the laser drilled holes. For the given laser processing and ultrasonic vibration parameters, the quality aspects of the laser drilled holes are significantly influenced by the laser irradiation time. Fig.5.19 presents the surface profiles from the laser drilled specimens showing material build-up near hole rims and spatter around the

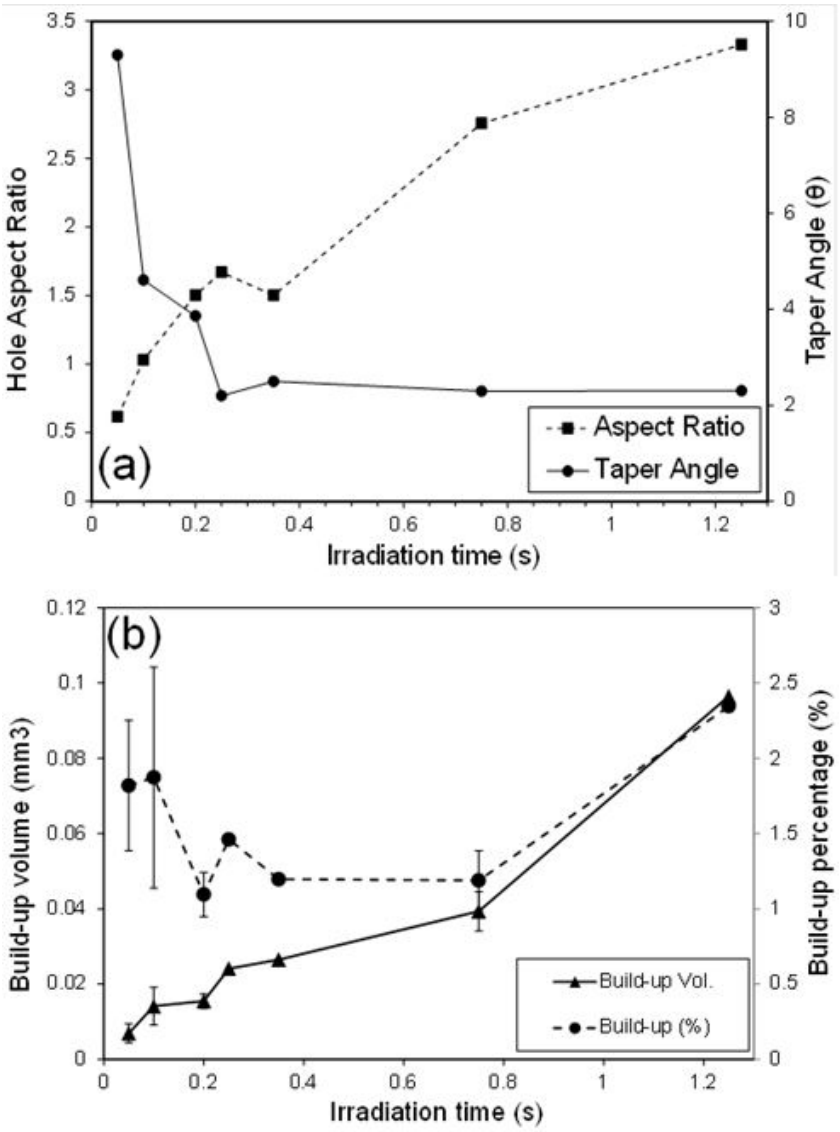

Figure 4.18: (a)Variation of hole aspect ratio and taper angle of laser drilled holes, and (b) variation of build-up volume and percentage with laser irradiation time for the ultrasonic vibration-assisted laser drilling

hole. The high speed camera images also show the appearance of brighter rim on the irradiated surface, indicating the formation of such build-up material. The material build-up near the rim of the hole is primarily due to lateral flow of melt outside the crater under the influence of ultrasonic vibrations. The material build-up is somewhat irregular, and the height of the build-up is not uniform along the rim of the hole. The measurement of the build-up volume using surface profilometry shows that the build-up material volume actually increases with increasing laser irradiation time, but the volume of build-up material in terms of percentage of total hole volume remained in the range of about 1-2.5% of the volume of the laser drilled holes at all the laser irradiation times. The observation indicates that the build-up material increases with increasing depth of the hole due to resolidification of ejected droplets on the initial build material. This is consistent with the observation based on angular trajectory of the ejected droplets. The droplets ejected nearly vertically from the bottom of the deeper holes are likely to fall and redeposit near the initial build up, increasing the amount of build-up material.

The surface SEM images (Fig.5.16) and the surface profiles (Fig. 5.19) of the laser drilled samples also show the presence of spatter on the surface due to resolidification of ejected droplets. The surfaces of the samples with shallower holes are relatively cleaner, and the amount of spatter increases with increasing the depth of hole, corresponding to the increasing laser irradiation time. It appears that the range (distance traveled) and angular distribution of the ejected melt droplets trajectory are large for shallower holes, yielding cleaner surfaces (i.e. the droplets fall and resolidify away from the hole). Most of the spatter on the surface for deeper holes is accumulated near the rim of holes, indicating that droplets ejected nearly vertically from the bottom of the deeper holes fall and resolidify closer to the hole rim and build-up material. The SEM images (Fig.5.16) from the surfaces of the laser drilled samples also show the presence of heat affected zone (regions with brighter contrast

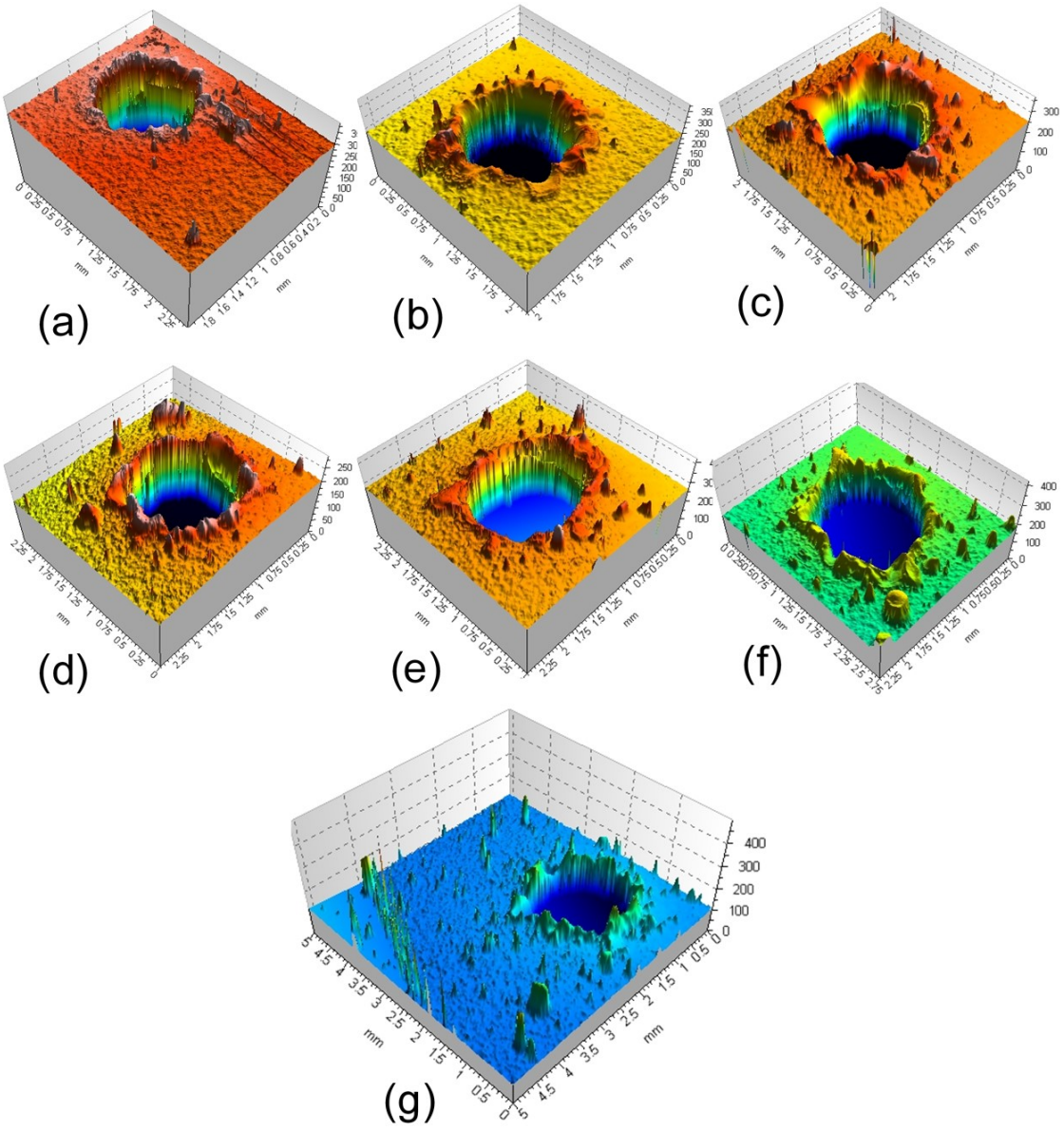

Figure 4.19: Three-dimensional profiles from the surfaces of the laser drilled specimens for laser irradiation times of: (a) 0.05 s, (b) 0.1 s, (c) 0.2 s, (d) 0.25 s, (e) 0.35 s, (f) 0.75 s, and (g) 1.25 s. (laser processing parameters: 950 W power and 15 mm working distance; ultrasonic vibration parameters: 20 kHz frequency and 23 μm vibration displacement)

around the rim of the holes). The thickness of the heat affected zone at the surface increases with increasing laser irradiation time (corresponding to increasing depth of the hole), indicative of heat accumulation with the continued laser irradiation during laser drilling (Fig.5.20). Significant recast layer was also observed on the walls of the holes drilled with all the laser irradiation times. A representative cross sectional SEM image from the etched sample (laser drilled with laser irradiation time of 0.35 s) showing distinct recast layer on the hole walls is presented in Fig.5.21(a). It can be seen that the recast layer thickness increases along the depth of the hole and is maximum at the bottom of the hole. The surface of hole walls are also rougher indicating resolidification of ejected droplets on the walls. A high magnification image of the recast layer from near the bottom of the hole is also presented in Fig.5.21(b). It can be seen that the microstructure of the recast layer consisted of primarily columnar grains (with width of grains about 3.84±0.53 μm) growing from the substrate towards center of the molten cap at the drilling front. The cellular grains with grain size of 4.37±1.46 μm are observed near the surface of the recast layer. It appears that the cellular grains are mostly formed in the recast layer near the bottom of the holes possibly due to resolidification of last remaining melt pool which could not be ejected due to very low volume.

The grain structure is primarily columnar in the recast layer formed near the top of the holes (Fig.5.21(c)). The variation of recast layer with depth of the holes drilled with laser irradiation times of 0.05, 0.35, 0.75 and 1.25 s is shown in Fig.5.22. For the straight holes drilled with shorter laser irradiation times (0.05 and 0.35 s), the recast layer is up to 65 μm at the hole entrance and about 65-240 μm at the bottom of the hole. For deeper holes drilled with laser irradiation times of 0.75 and 1.25 s, the laser drilling was unstable and resulted in build-up of material on the hole walls and formation of closed cavities along the hole depth. The recast layer was relatively thicker ($\sim$100-180 μm) for these holes along with localized build-up of about 0.5 mm

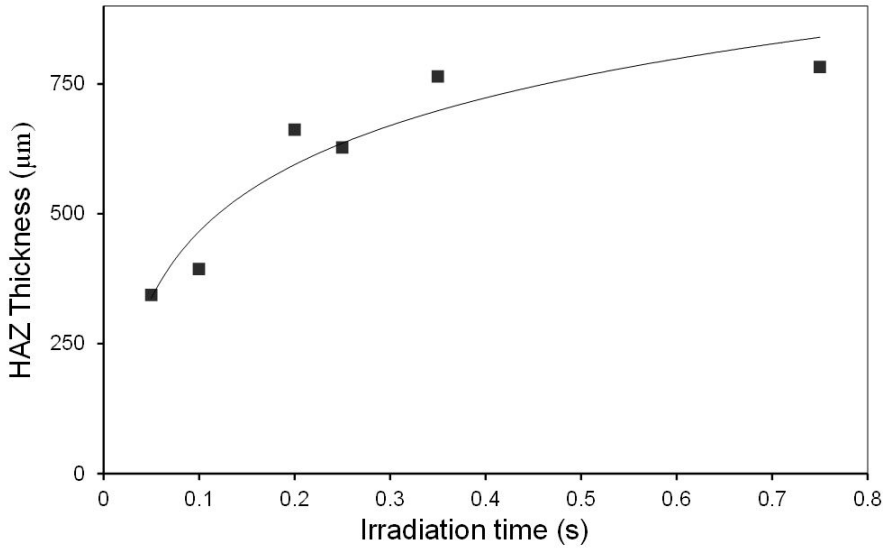

Figure 4.20: Variation of thickness of heat affected zone (HAZ) at the surface of laser drilled specimens with laser irradiation time for the ultrasonic vibration-assisted laser drilling

at some locations along the depth. The locations along the depth where hole closes due to resolidification of expelled material are also marked in the Fig.5.22.

Finite element analysis

A multi-step two-dimensional finite element modeling (FEM) approach, taking into account the observations of melt expulsion from the high speed photography, was developed to analyze temperature distributions and hole formation during the laser surface melting of the AISI 316 stainless steel specimens. Commercially available COMSOL Multiphysics® software was selected to solve the heat transfer equations. The specimen geometry was rectangular with dimensions of 12 mm for top and bottom surface and 3.5 mm for the two sides. The top surface of the geometry irradiated with the laser beam was subjected to heat flux, natural convection, and radiation boundary conditions. The bottom surface of the geometry was considered insulating, and the two sides were subjected to natural convection and radiation heat transfer

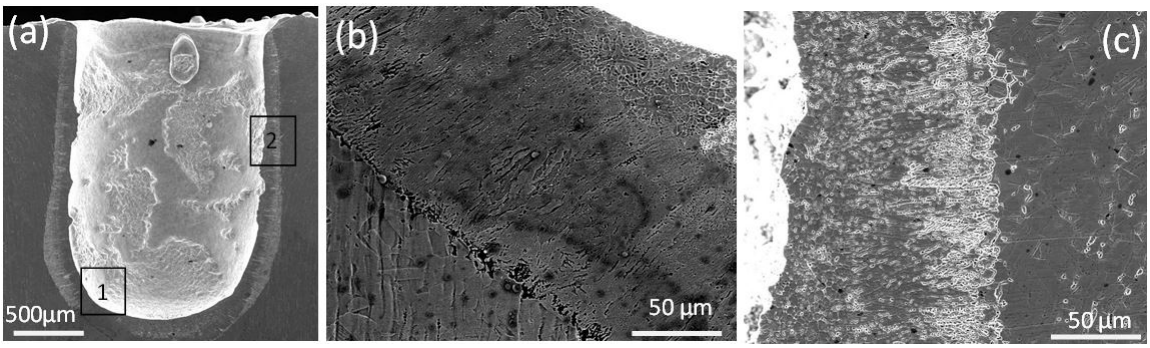

Figure 4.21: (a) SEM micrograph showing recast layer on the walls of laser drilled holes, and (b-c) higher magnification microstructures of recast layers from regions near the bottom and entrance of the holes, identified as regions 1 and 2 in (a), respectively

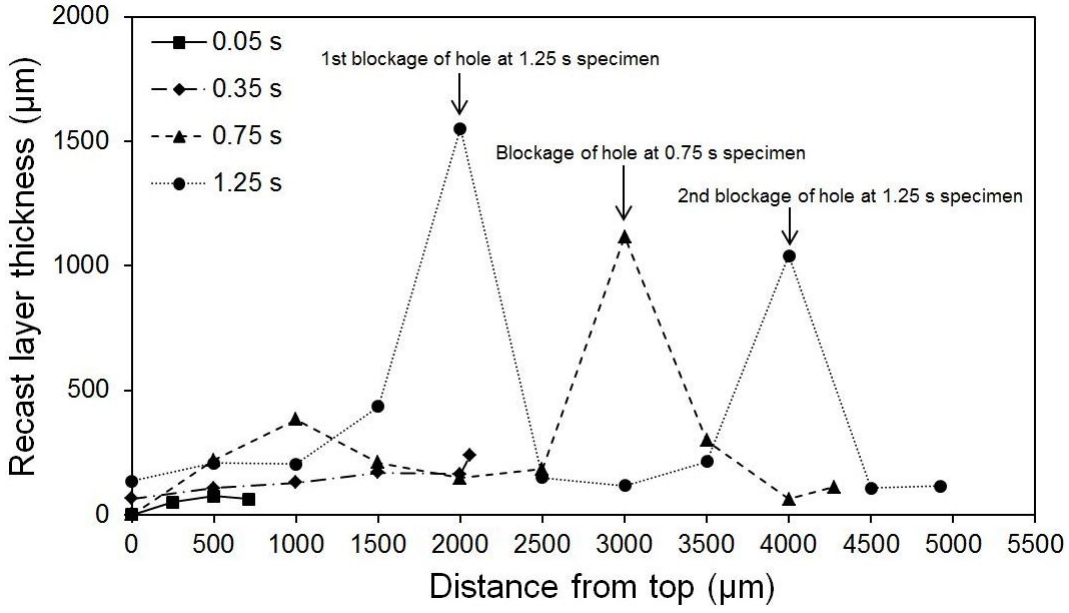

Figure 4.22: Variation of recast layer thickness on the hole walls with distance from the surface along the depth of the hole for different laser irradiation times. The locations of localized build-up of material along the hole depth are also indicated

boundary conditions. Minimum and maximum mesh size was 0.001 mm and 0.1 mm, respectively. Following assumptions were considered:

1. Laser beam has a Gaussian distribution of the energy (TEM00).

2. Material loss due to surface evaporation and recoil pressure is not involved, and the material removal during the ultrasonic vibration-assisted laser melting occurs in molten state.

3. Multiple reflections of laser beam in the drilling cavity are negligible.

The material properties and initial boundary conditions for the heat transfer model are listed in 4.2 and 4.3. The procedure for calculating volume of material removed for the formation of holes during ultrasonic-vibration assisted laser surface melting is discussed below.

Step I: In the first step, the heat transfer model was solved with the given boundary conditions to determine the temperature distribution in the sample and the laser irradiation time for the initiation of melting at the surface. Fig.5.23(a) shows the temperature distribution in the sample when the surface of the material reaches melting point corresponding to laser irradiation time of 1.53 ms. The evolution of surface temperature as a function of laser irradiation time is also in Fig.5.24.

Step II: The high speed camera images indicated that the surface melting initiates and melt pool grows before the ejection of the melt droplets, indicating that critical volume of melt is required for the droplet ejection. The droplet ejection initiates at about 2.2 ms of laser irradiation. The FEM analysis in first step showed that surface melting initiates at about 1.53 ms. The time interval of 0.67 (t_1) corresponds to the time taken for the initiation of first melt expulsion after the initiation of surface melting. Using the time for melt ejection of 2.2 ms (based on high speed camera), the FEM model was run to determine the temperature distribution and volume of molten material for droplet ejection. The Fig.5.23(b) shows the temperature distribution

Table 4.2: Materials properties and model parameters employed in 2D heat transfer finite element analysis

Parameter	Symbol	Value (AISI 316 stainless steel)	Ref
Density ($\frac{kg}{m^3}$)	ρ	$8084 - 0.4209 \times T - 3.894 \times 10^{-5} \times T^2$ $T < 1700K$ $7433 - 0.0393 \times T - 1.801 \times 10^{-4} \times T^2$ T$\geq$ 1700K	[82]
Heat capacity ($\frac{J}{kg.K}$)	C_p	462+0.134×T $T < 1700K$ 775 T$\geq$ 1750K	[82]
Thermalconductivity ($\frac{W}{m.K}$)	k	14.6-33.7 273 K<T<1753 K 120 T<1700 K	[83]
Melting temperature (K)	T_m	1753 K	
Stefan-Boltzmann constant ($\frac{W}{m^2.K^4}$)	σ	5.67×10^{-8}	[84]
Absorption coefficient	A_c	0.15	
Emissivity	ϵ	0.4	[85]
Standard deviation of laser beam (mm)	ϕ	Beam diameter/6	[86]

and melting isotherm after laser irradiation for 2.2 ms. Fig.5.24 shows that the temperature at the surface of the melt reaches to about 1835 K at the laser irradiation time of 2.2 ms. The depth and width of melting after this irradiation time are about 24 μm and 439 μm, respectively. The corresponding melt volume (V_c) at the t=2.2 ms is 1.82× 10^{-6} μm^3.

Step III: In the next step, it was considered that the ejected material corresponding to first critical volume of melt is removed from the surface, and that the laser

Table 4.3: Boundary conditions employed in 2D HT finite element analysis

Boundary Conditions	Equation	Ref
Heat flux (top boundary)	$\rho\ C_p \left[\frac{\partial T}{\partial t}\right] = k\left[\left(\frac{\partial^2 T}{\partial x^2}\right) + \left(\frac{\partial^2 T}{\partial x^2}\right)\right]$	[86]
Natural convection and radiation heat transfer (top and side boundaries)	$- k\left[\left(\frac{\partial T}{\partial x}\right) + \left(\frac{\partial T}{\partial x}\right)\right] = AP_{Gau} - \varepsilon\sigma\left[T^4 - T_0^4\right] - h\left[T - T_0\right]$	[86]
Laser power density in Gaussian distribution ($\frac{W}{m^2}$)	$P_{Gau} = \left(\frac{P}{\pi\varphi^2}\right) \times e^{\frac{-2(x-x_0)^2}{\varphi^2}}$	[87]

heating continues on the new surface (at melting point) to form the critical volume of melt for next droplet ejection. In this step, the volume of material corresponding to critical volume of melt was removed from the geometry, and new boundary conditions were applied to keep the temperature distribution developed in remaining of the specimen. Fig.5.23(c) shows the updated geometry and temperature distributions after removal of melt volume due to droplet ejection. It should be noted that the finite element analysis takes time of about 0.035 s for the stabilization of given temperature distribution in the sample and attain the domain temperature (corresponding to melting point) at the surface of updated geometry (Fig.5.24).

Step IV: In the last step, the FEM analysis was conducted with laser irradiation on the updated geometry until the critical volume of melt is formed again. In contrast to the first step where the initial temperature of the irradiated surface and sample is room temperature, the surface of the updated geometry in this step is at melting temperature with temperature distributions in the sample. Other heat transfer boundary conditions such as surface convection and surface-to-ambient radiation applied to the surface in first step were also applied to the updated geometry in this last step. Fig.5.23(d) shows the temperature distributions in the sample corresponding to the formation of critical melt volume in the updated geometry (t=2.56 ms). The critical volume of melt is formed in the updated geometry after the time interval of 0.325 ms (t_2) after the first melt expulsion. The temperature evolution at the surface in this step is also shown in Fig.5.24. The surface of the melt reaches the temperature of about 1813 K at the end of this step.

Considering that material removal continues with repeated formation of critical volume and droplet ejection, the FEM analysis can be continued by updating the geometry for each melt expulsion during the entire duration of laser irradiation. However, this computational analysis will be too time intensive due to large number of steps involved (corresponding to number of melt expulsions during the entire duration

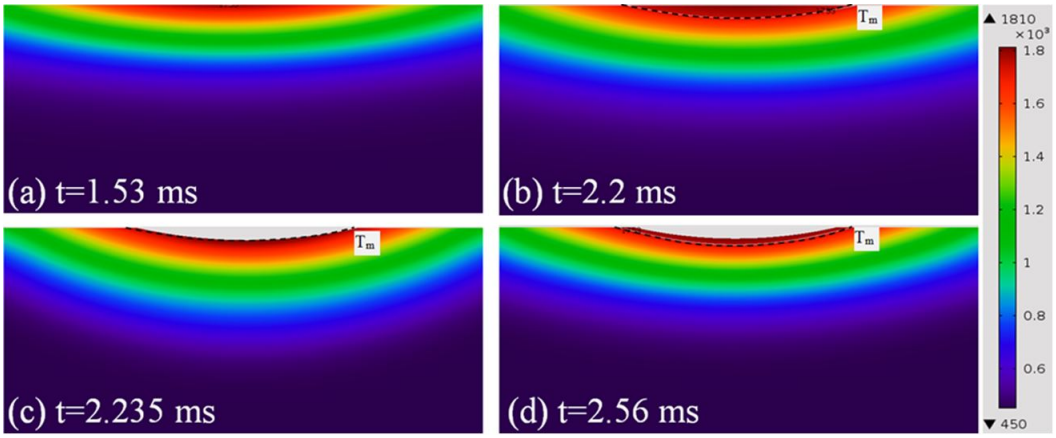

Figure 4.23: Calculated temperature distributions in the cross section of the laser irradiated specimens at: (a) initiation of surface melting at t=1.53 ms, (b) initiaton of melt ejection when the critical melt volume is formed at t=2.2 ms, (c) updated geometry after removing the volume of melt corresponding the melt ejection volume, and (d) continued laser irradiation of updated geometry to form critical volume of melt again

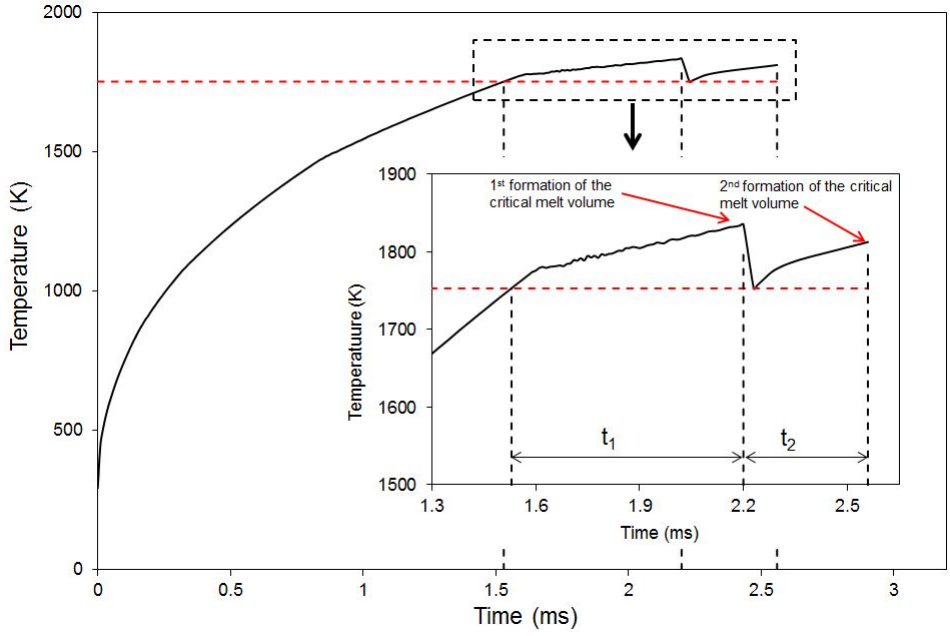

Figure 4.24: Variation of surface temperature with irradiation time; the inset shows the details of temperature distributions near melting point indicating first and second formations of the critical melt volume for melt expulsion

of laser irradiation) and also due to time taken for the stabilization of temperature distribution after each melt expulsion (accounted by removing the melted region and updating the model geometry). As the surface temperature of the updated geometry (at melting point) and temperature distribution in the sample is not likely to change much for subsequent steps, the time interval for subsequent melt expulsions is likely to remain close to that taken for the second melt expulsion (t_2=0.325 ms). The hole volume can then be given by:

$$V_h = \frac{t}{t_2} \times V_c \tag{4.3}$$

where t_2 is the time for melt expulsion (t_2=0.325 ms), t is the laser irradiation time after the first expulsion of the melt [t=total irradiation time (t)-melt initiation time (t_i=1.53 ms)], and V_c is the critical volume of melt for melt expulsion. The hole volumes predicted from the above FEM analysis were compared with experimental hole volumes for all laser irradiation times (Fig.5.25). It can be seen that the predicted hole volume increases linearly with the laser irradiation time. Note that actual amount of material removed (mass loss) and depth of the hole increase linearly only up to the laser irradiation time of 0.35 ms. Beyond this laser irradiation time (i.e. for deeper holes), the effects related to resolidification of ejected droplets on the walls of the holes and formation of closed cavities dominate and the laser drilling rate slows down. Similar trend is also observed for the variation of experimental hole volume with the laser irradiation time. The predicted hole volume shows close agreement, though with some underestimation, with the experimental value up to laser irradiation time of 0.35 s. These are the conditions that resulted in the formation of straight holes with fairly good geometric and quality parameters. The FEM analysis overestimates the hole volume for the longer irradiation time (0.75 and 1.25 s) because it doesn't account for the aforementioned effects.

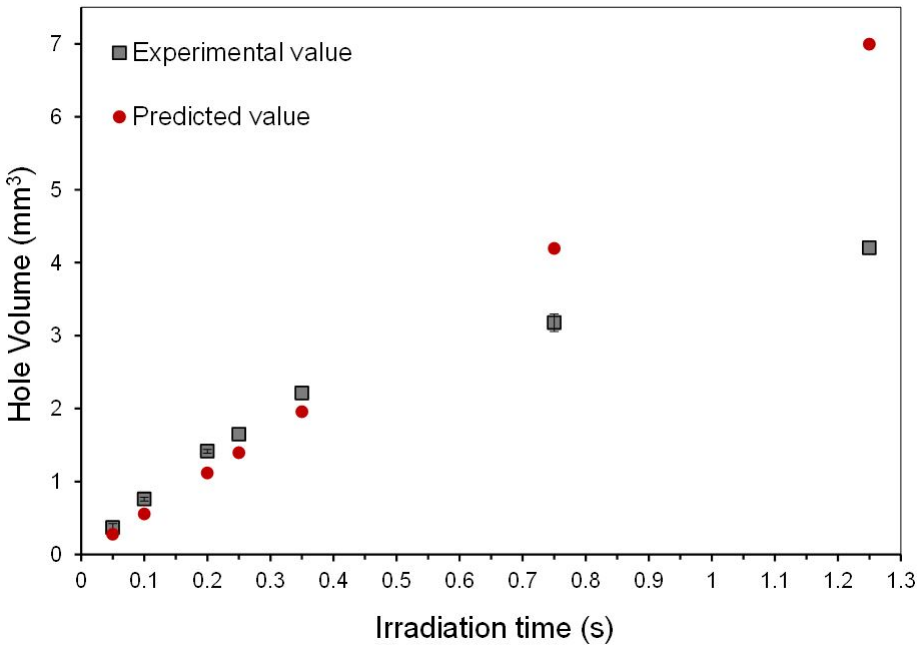

Figure 4.25: Variation of experimental and predicted hole volume with laser irradiation time for the ultrasonic vibration-assisted laser drilling

Conclusions

This study systematically investigated the evolution of geometric features (hole depth, diameter, aspect ratio, and taper) and quality parameters (material build-up, spatter, recast layer thickness, and heat affected zone) of holes with laser irradiation time for the ultrasonic vibration-assisted CW CO_2 laser surface drilling (UVLD) of AISI 316 stainless steel. The UVLD process presents a great potential for the laser drilling of straight sub-2 mm diameter holes (with depth up to 5 mm) in continuous wave laser melting regime. The depth of the laser drilled holes increases almost linearly in the early stages (irradiation time up to 0.2-0.25 s), the drilling rate then progressively decreases (irradiation time 0.25-1.25 s). Based on the analysis of angular trajectory distribution of ejected droplets, the observed trend is related to the resolidification of ejected droplets on the hole walls as the hole gets deeper (corresponding to increasing laser irradiation time). Straight holes with aspect ratio up to 3.5 and taper angle

of about 2.3° were successfully drilled with the UVLD of stainless steel. The holes drilled with ultrasonic vibration-assisted laser drilling also exhibited typical quality defects such as build-up material at the hole rims, spatter of the surface, recast layer on hole walls, and heat affected zones. The amount or extent of these quality features generally increases with increasing laser irradiation time. While the laser drilled holes exhibited good straightness and circularity up to the laser irradiation time of 0.35 s, the deeper hole holes formed with laser irradiation time of 0.75 and 1.25 s showed localized build-up of ejected droplets on the hole walls, resulting in localized narrowing and closure of the holes. For the UVLD of AISI 316 stainless steel, the high speed camera images indicated that a critical volume of melt is required for the initiation of melt expulsion and hole formation under the influence of ultrasonic vibrations. The multi-step finite element analysis, taking into account the observations of melt expulsion from high speed photography, gives close prediction of laser drilled hole volume in the early stages of laser drilling (laser irradiation time up to 0.35 s).

4.2.3 Effect of working distance on hole quality and geometry in ultrasonic vibration-assisted laser drilling

Introduction

Lasers are at the forefront of materials surface modification (heat treatment, melting, cladding, and coatings), machining (drilling, cutting, and milling) and forming (welding and joining) technologies [9]. Among these technologies, laser drilling of materials such as diamond wire-drawing dies and stainless steel is probably one of the earliest commercial applications of lasers in materials processing [13]. As the laser technology developed, the laser drilling process was also extended for the machining of an entire range of materials including metals/alloys, ceramics, polymers, and composites [88–92]. The laser drilling process offers several advantages including non-contact processing, rapid drilling of precision high aspect-ratio holes, and excellent quality (defined in terms of heat affected zone, spatter, material build up on/around hole wall, and hole taper) [9]. With the laser drilling in the surface melting regime, the high intensity pulses cause melting of thin region followed by evaporation from the surface of melt film. The evaporation-induced recoil pressure, when exceeds the surface tension forces, pushes the melt radially out, creating hole by melt expulsion [93, 94]. It has been reported that the dominant material removal mechanism shifts from surface evaporation to melt expulsion when the laser power decreases [95]. The laser drilling involving melt expulsion often results in asymmetric hole shape and recast layer formation (due to incomplete melt expulsion) [23]. Significant efforts have been made to improve the efficiency of material removal and quality of holes during laser drilling with the use of co-axial inert and reactive assist gases [15, 28, 29, 96, 97]. The laser beam diameter and laser beam focus conditions also influence the material removal and quality of holes [21, 30, 31]. It has been observed that the quality of laser drilled holes, defined in terms of hole straightness and depth, is much better when the beam

waist is positioned just below the surface of the workpiece [21]. Some efforts have also been made to improve the efficiency of laser drilling and the quality of holes by the application of ultrasonic vibrations during pulsed laser drilling [51,52]. While the conventional laser drilling is primarily performed using pulsed lasers, the continuous wave lasers are used in surface engineering applications for microstructure refinement, surface alloying, composite surfacing, and cladding [15, 98–100]. In a conventional continuous wave laser surface melting with a stationary beam (i.e. without laser scanning), the melt pool solidifies in place forming a characteristic semi-ellipsoidal re-solidified region. Recently, it has been observed that the simultaneous application of ultrasonic vibrations (frequency of 20 kHz) during continuous wave laser surface melting of stainless steel facilitates the expulsion of the melt from the laser irradiated surface, forming well defined craters [79, 80]. The laser melting using similar processing parameters without the simultaneous application of ultrasonic vibrations resulted in surface heating and melting without significant melt expulsion (i.e. no hole drilling regime). The simultaneous application of ultrasonic vibrations helps in destabilizing the surface melt film causing ejection of droplets. The effect of ultrasonic vibration displacement for the given frequency of 20 kHz on the geometric parameters (depth and diameter) of craters and microstructure of the resolidified surface film has been investigated. The preliminary results have indicated that continued laser irradiation with simultaneous application of ultrasonic vibrations can lead to the formation of straight and high aspect-ratio holes primarily due to efficient expulsion of melt from the laser irradiated surface [80].

Methods

The UVLD process was performed on 3.5 mm thick AISI 316 stainless steel specimen. Each steel specimen was mounted on a threaded 13-mm diameter Ti-alloy probe/horn. The surface of the steel specimens were sand blasted to enhance the ab-

sorption of the laser beam. The ultrasonic vibrations with vibration frequency of 20 kHz and vertical displacement of 23 μm were generated using a 750 W power supply (Sonics & Materials, Inc, Newtown, CT). For drilling, the surface of the vibrating specimen was irradiated with a continuous wave CO_2 laser operated with power of 950 W and irradiation time of 0.4 s. An argon shielding gas was used during the laser drilling process to prevent the surface oxidation of the specimen and protect the laser focusing lens. The details of the experimental set-up ultrasonic vibration-assisted laser surface processing have been reported in previous publications [79, 80]. For the ultrasonic vibration and laser processing parameters, the experiments were performed for four working distances (i.e. the distance between the laser head and surface of the specimen): 15, 25, 35, and 50 mm. For the given laser processing parameters, the working distance controls the beam diameter and laser power density at the irradiated surface. High speed camera imaging was conducted using X-StreamVISION (XS-4, IDT) with the maximum frame rate of 400,000 Hz. To enhance the captured images and preventing the oversaturation (due to the high amount of illumination from the laser light), the exposure time of 22 μs was selected. Images were captured with 8000 fps rate with image size of 480 $\times$ 320 pixels. A scanning electron microscope (JEOL Ltd, Tokyo, Japan) was used to characterize the microstructural and geometric features of holes drilled using the UVLD. An optical profilometer (Nanovea, Irvine, CA) was used to characterize 3-D surface profiles of the drilled surfaces. The measurements of hole diameter and depth were performed from the SEM images using image processing software, ImageJ.

Results and Discussion

High speed camera imaging of UVLD process To investigate the mechanisms of UVLD process, the high speed photography of the drilling process was performed. Fig.5.26 presents the sequence of frames capturing major events during the laser drilling of

steel with the working distance of 15 mm. The surface heating is observed as a bright spot on the irradiated surface (Fig.5.26b). Subsequently, the melt pool forms and the area of the melt pool increases with the irradiation time. A well-defined rim of molten material appears at the outer border of the irradiated region, indicating first signs of melt flow radially outward. (Fig.5.26c-d). When the central melt reaches a critical size/volume, the melt film destabilizes and the melt ejection starts in the form of droplets (Fig.5.26e-f). The ejection of first droplet is captured in the frames; it has been observed that it takes about 2 ms from the incident of laser-material interaction to reach the critical volume for droplet ejection. With continued laser irradiation, a stream of droplets is ejected and the melt front advances down the drilled hole. It can be seen that the bright rim observed in the earlier frames (Fig.5.26c-f) disappears after the ejection of droplet stream (Fig.5.26g-i), indicating resolidification of the expelled melt in the form of build-up material at the hole periphery. Form these images, it appears that material removal is primarily in the form of droplet ejection in the later stages of the laser drilling.

Geometric and quality aspects of holes

From the preliminary results and the high speed photography, it has been demonstrated that the application of ultrasonic vibrations during continuous wave laser surface melting results in the sideways expulsion/flow of melt and ejection of droplets, forming deep craters and holes. The surface profile and cross-sectional SEM images of the steel specimens drilled with UVLD process for four working distances (15 mm, 25 mm, 35 mm, and 50 mm) are presented in Fig.5.27.

It can be seen that the geometric and the quality aspects of the surface holes are significantly influenced by the working distance for similar laser processing and ultrasonic vibrations parameters. Well-defined cylindrical holes were obtained with the working distance of 15 mm (Fig.5.27a). The shape of the hole is more conical

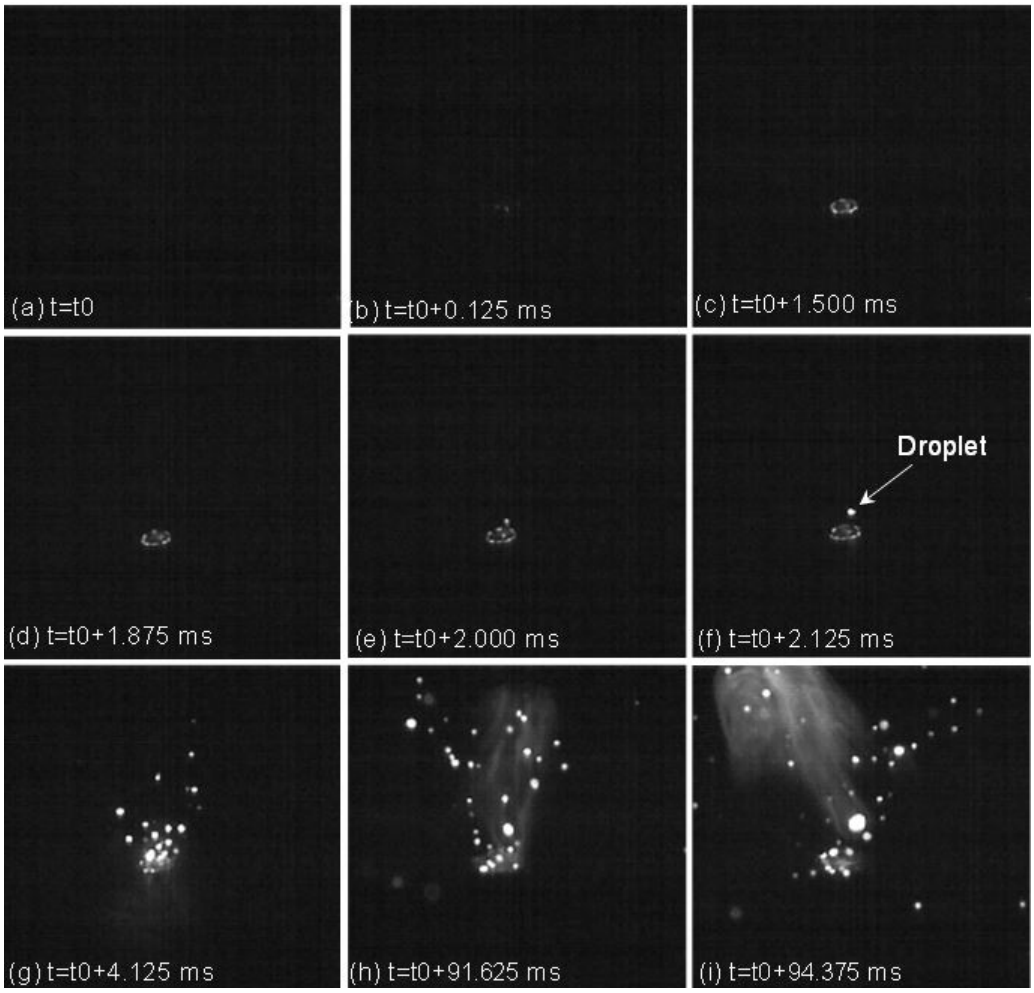

Figure 4.26: High speed camera photographs of UVLD process for the working distance of 15 mm

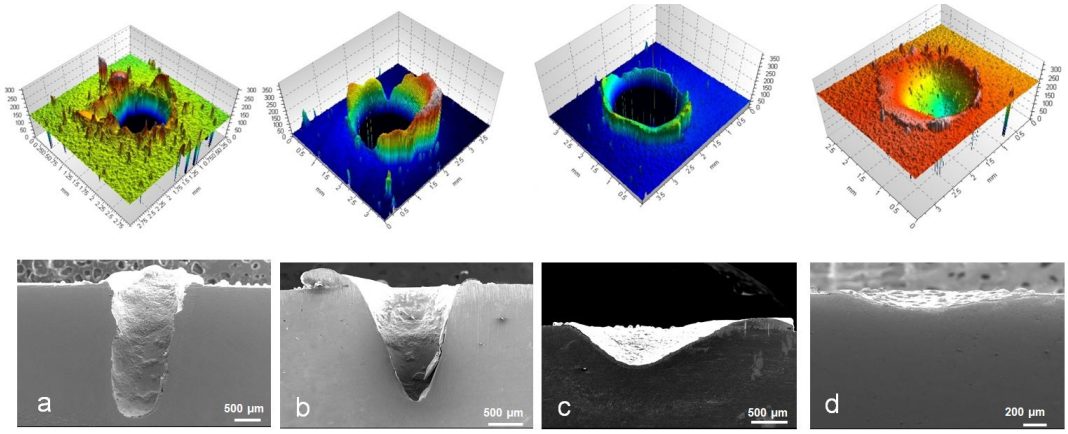

Figure 4.27: Surface profiles and cross-sectional SEM micrographs of the UVLD specimens for laser irradiation time of 0.4 s and working distances of: (a) 15 mm, (b) 25 mm, (c) 35 mm, and (d) 50 mm

for the longer working distances of 25 and 35 mm (Fig.5.27b-c). For the working distance of 50 mm, a very shallow crater of depth 133 μm was formed on the surface. Fig.5.28 presents the variation of the diameter and the depth of the UVLD holes for the studied experimental working distances. It can be seen from the figure that the hole diameter first increases with working distance up to 35 mm, followed by slight decrease when the working distance was 50 mm.

The hole diameters were about 1365, 1601, 1911, and 1602 μm with the working distance of 15, 25, 35, and 50 mm, respectively. The depth of the hole, on the other hand, decreases continuously with increasing working distance. The depths of holes were 2568, 1706, 505, and 133 μm with the working distance of 15, 25, 35, and 50 mm, respectively. The hole taper angle was calculated by equation 4.2. It should be noted that in this study, d_0 is the diameter of the hole at the hole depth of 350 μm. The variation of hole aspect ratio (ratio of hole depth to hole diameter at entrance) and taper angle with the working distance is shown in Fig.5.29. The taper angle was not calculated for the shallow holes/craters formed with the working distance of 50 mm. Clearly, the focused laser beam melting with smaller working distances results

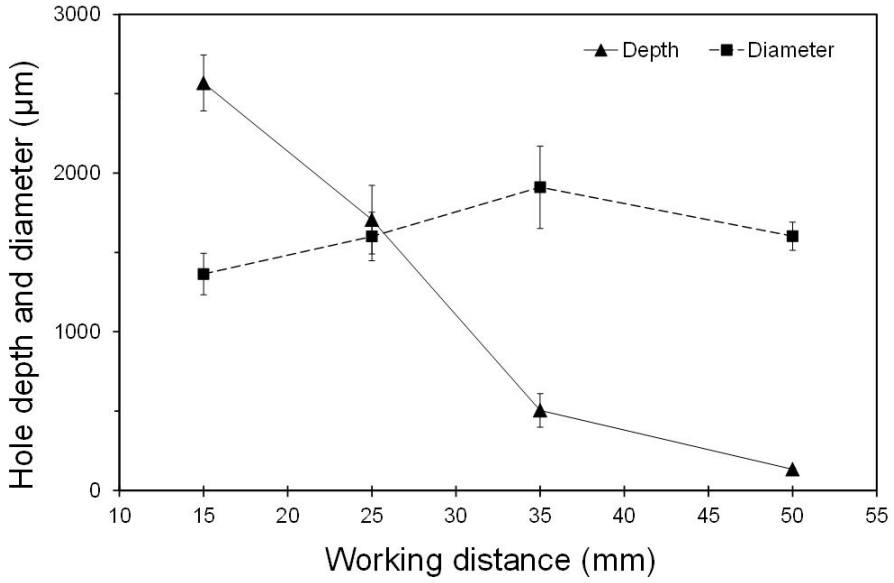

Figure 4.28: Variation of the hole depth and diameter for working distances of 15 mm, 25 mm, 35 mm, and 50 mm

in deeper, higher aspect-ratio, and straighter holes. The variation in the diameter and depth of hole with the working distance can be explained based on the energy distribution in the laser beam. Note that the hole diameter is established by the critical volume of the melt for the melt expulsion and droplet ejection. After the initiation of material removal, the energy is channeled into the hole causing further material removal without significantly affecting the hole diameter.

For the given laser power and energy distribution (Gaussian) in the beam, the melting diameter increases with increasing laser beam diameter; this also means that energy distribution spreads out over a larger area, and the area over which the power density exceeds the threshold power density for melting increases with increasing laser beam diameter. This explains the increasing diameter of the hole with increasing working distance from 15 to 35 mm. For the working distance of 50 mm, the beam diameter is so large that area over which the power density exceeds the threshold power density for melting starts decreasing, resulting in smaller hole diameter. On the other hand, the peak power density decreases continuously with increasing work-

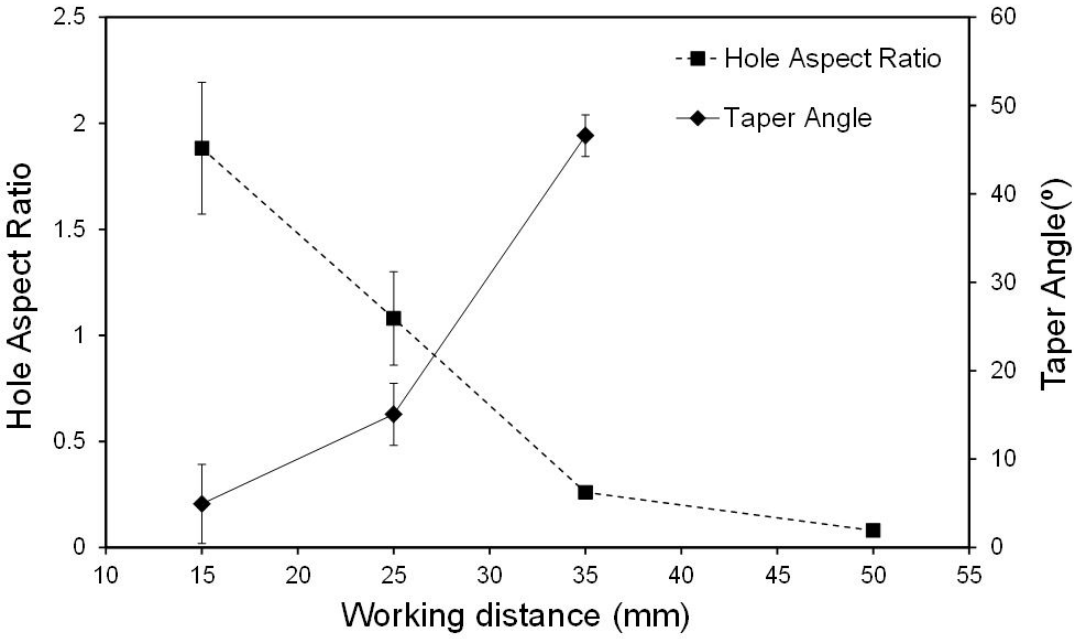

Figure 4.29: Variation of hole aspect ratio and taper angle for working distances of 15 mm, 25 mm, 35 mm, and 50 mm; taper angle was not calculated for shallow crater formed with working distance of 50 mm

ing distance (i.e. laser beam diameter). For a shorter working distance (i.e. smaller beam diameter), the peak power density is very high and melting occurs in very short time, resulting in early initiation of material removal; this translates into deeper holes due to extended time period for material removal. The hole depth decreases with increasing working distance primarily due to delay in reaching the critical melt volume for material expulsion and droplet ejection. For these longer working distances, extended time of laser irradiation is required to form deeper holes. The spatter due to resolidified droplets on the surface and the material build-up due to outward melt flow at the hole periphery are considered as defects of the laser drilling of materials. The laser drilling conditions are often optimized to produce as clean holes as possible. Post-finishing operations are often required to clean the laser drilled surfaces. The contributions of outward melt flow (material build-up) and droplet ejection (spatter) to the material removal were estimated for the UVLD process for the investigated working distances (Fig.5.30). The overall material balance for the drilling is given by:
A (Volume of hole) = B (Volume of build-up material) + C (Volume of spatter lost outside the surface) + D (Volume of spatter resolidified on the surface)
The volume of the hole (A) was calculated from the SEM images assuming symmetric holes; the volume of build-up material (B) was calculated directly from the volume of material accumulated at the periphery of the hole estimated from the surface profiles; the volume of the spatter lost outside the surface (C) was calculated from the weight loss in the drilling process; the volume of spatter resolidified of the surface (D) was estimated from the material balance. The volume percentages of material build-up (B) and total spatter (C+D) with the UVLD process for different working distances are presented in Fig.5.30. For all the working distances, it is primarily the spatter due to ejected droplets that contributes to material removal; about 73-97% of material removal is in the form of spatter. However, the volume percentage of spatter decreases and the build-up material increases with increasing working distance.

This observation is directly related with the decreasing depth of hole with increasing working distance. The build-up material is formed in the very early stages of drilling. As the depth of the hole increases, the upward melt flow becomes difficult and the material removal is mostly dominated by the droplet ejection as observed from the high speed photography images. Even with the shallow holes observed with longer working distance (50 mm), the material removal is mostly in the form of ejected droplets.

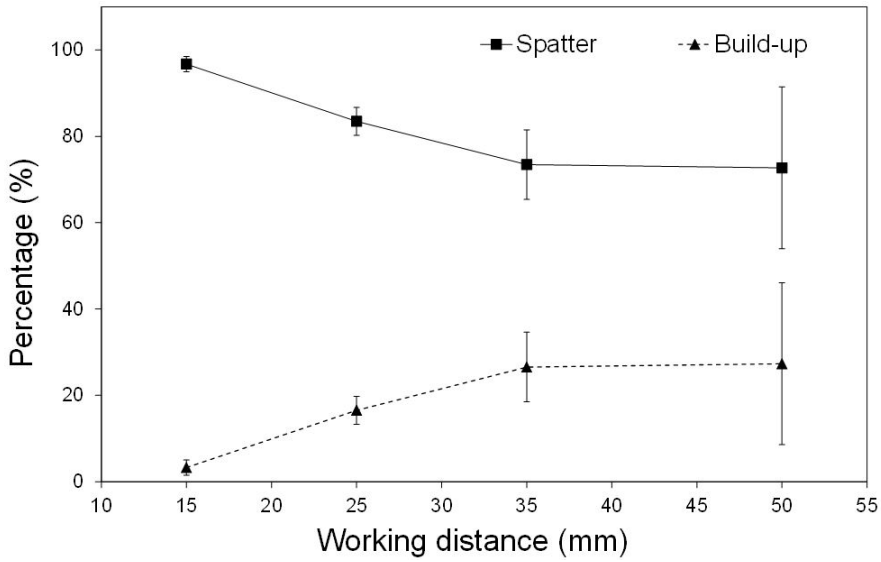

Figure 4.30: Variation of spatter and material build-up percentages for working distances of 15 mm, 25 mm, 35 mm, and 50 mm

However, the SEM images show relatively clean surfaces, indicating that most of the melt droplets from the shallow holes were ejected outside the surface of the drilled specimens. On the other hand, significant spatter is observed near the deeper holes (drilled with working distance of 15 mm) indicating that the spatter near the surface is mostly due to droplets ejected from deeper melt front. For the deep holes, it has also been observed that the ejected droplets impinge and re-solidify on the hole walls, resulting in narrower holes.

Finite element analysis of the UVLD process

The finite element model which was used for the prediction of the hole volume at investigation of time effect was used in this study. As the ultrasonic parameters were similar for all the working distances studied in the experiments, it was assumed that critical melt volume of 1.82×10^{-6} μm^3 must be reached for the expulsion of the melt in all the cases. Once the critical volume of melt is reached, it was assumed that the entire molten material is removed in the form of melt expulsion and droplet ejection from the irradiated surface. From this analysis, the volume of the hole for irradiation time 0.4 s with the working distance of 15 mm was estimated to be 2.231 mm^3.

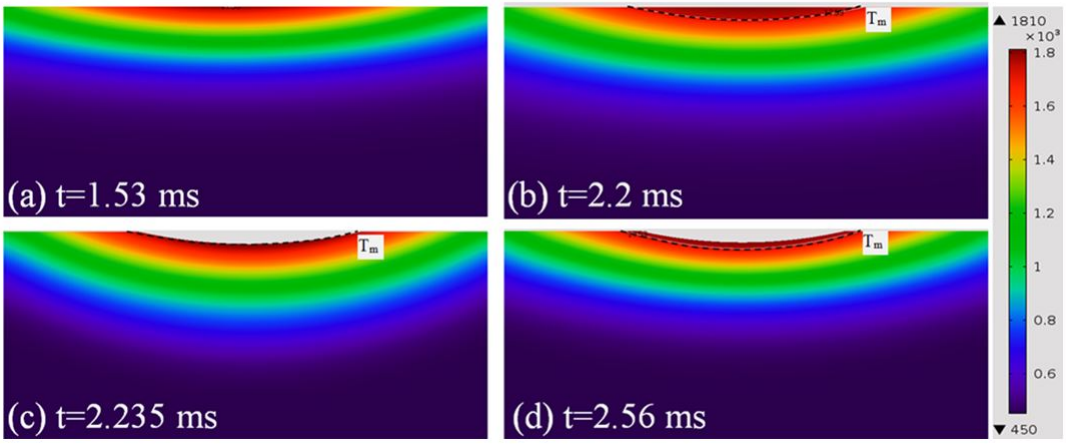

Figure 4.31: Variation of surface temperature with irradiation time showing first and second formations of the critical melt volume for melt expulsion for working distances of: (a-b)15 mm, (c-d) 25 mm, (e-f) 35 mm, and (g-h) 50 mm

The evolution of the surface temperature leading to first two steps of melt expulsion during the early stages of laser irradiation for the working distance of 15 mm is shown in Fig.5.31a-b. The irradiation time when the surface temperature reaches the melting point of the material is indicated on the temperature profiles (t=1.53 ms). The surface temperature exceeds the melting point (T_s=1835 K) for the time corresponding to initiation of first melt expulsion (t=2.2 ms); the time for melt expulsion

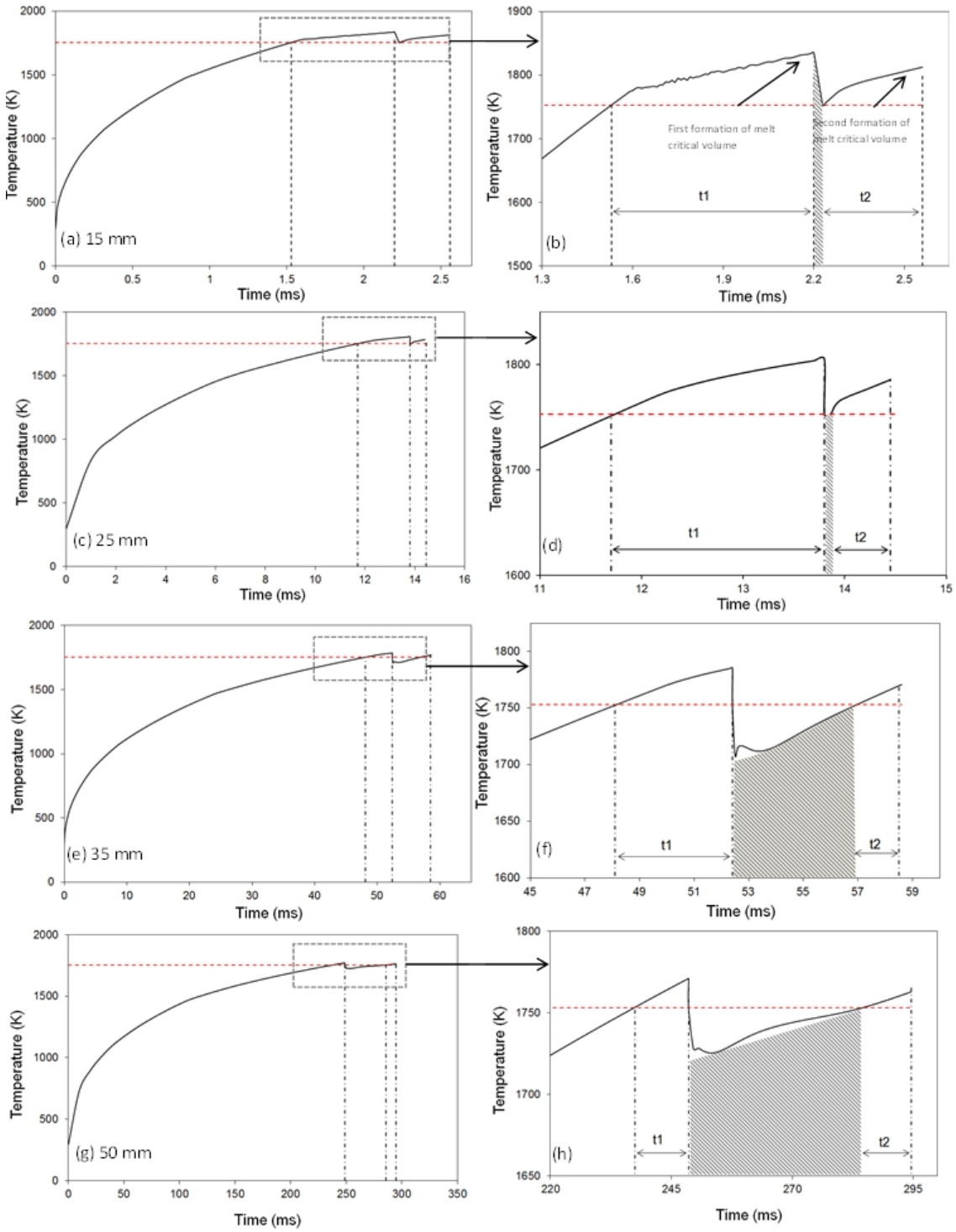

Figure 4.32: Variation of surface temperature with irradiation time showing first and second formations of the critical melt volume for melt expulsion for working distances of: (a-b)15 mm, (c-d) 25 mm, (e-f) 35 mm, and (g-h) 50 mm

after initiation of melting is t_1=0.67 ms. After the geometry is updated to remove of the melt volume, it takes time (i.e. the stabilization time for working distance of 15 mm is 0.035 ms) for the finite element analysis to stabilize the temperature distribution in the updated geometry because initial boundary conditions were added after stopping the simulation and updating the geometry. The stabilization of temperature distribution is indicated by hashed area in the temperature profile. After model stabilization, the new surface (after updating the geometry) temperature increases continuously from melting point (T_m) to new surface temperature (T_s=1813 K) with increasing irradiation time until the critical volume of melt is reached (step II). The stabilization time for temperature distribution in the model was not taken into account in the calculation of time for melt expulsion; the time for melt expulsion after stabilization is t_2=0.325 ms. The temperature distributions indicating initiation of first melting, melt expulsion time in first step (t_1), and melt expulsion time in step 2 (t_2) after stabilization for different working distances are also presented in Fig.5.32. The predicted values of t_1, t_2, and V_h are listed in 4.4.

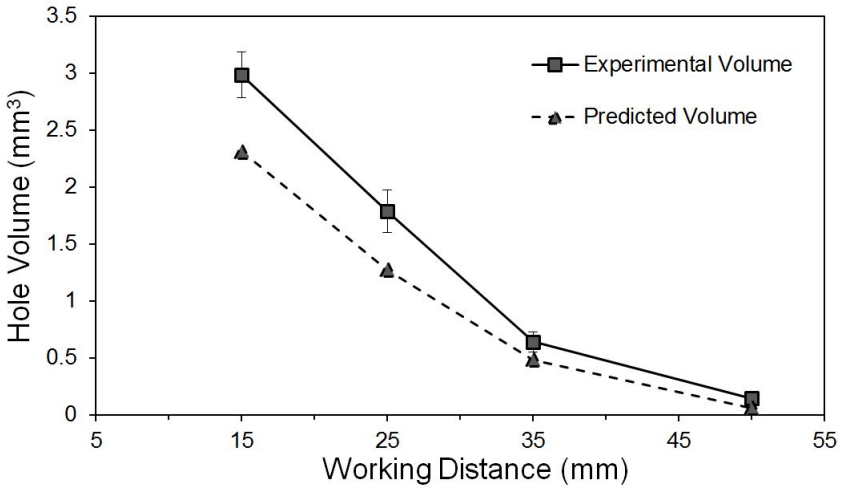

Figure 4.33: Experimental and predicted values of hole volume for working distances of 15 mm, 25 mm, 35 mm, and 50 mm

The experimental and predicted values of the hole volume for the UVLD drilled

Table 4.4: The predicted melt initiation time, melt expulsion time in first step (t_1), and melt expulsion time in step 2 (t_2), and hole volume (V_h) for various working distances. The experimental hole volume is also compared with the model predictions.

Critical melt volume Vc, μm3	Working distance (mm)	Initiation of melting (ms)	Melt expulsion time in first step t_1, (ms)	Melt expulsion time in second step t_2, (ms)	Predicted hole volume, V_h (mm^3)	Experimental hole volume (mm^3)
1.82×10^{-6}	15	1.53	0.67	0.325	2.231	2.985±0.204
	25	11.7	2.1	0.59	1.198	1.786±0.188
	35	48.1	4.3	1.5	0.427	0.639±0.089
	50	237.5	11.1	10	0.0295	0.143±0.042

specimens for the four working distances are presented in Fig.5.33. It can be seen that the hole volume decreases with increasing working distance, and the prediction of hole volume based on step-wise material removal follows the experimental trends very closely. For the given laser power (950 W) and irradiation time (0.4 s), the melt initiation time increases (i.e. surface melting is delayed) with increasing working distance, resulting in fewer steps of material removal and smaller overall volume of the drilled hole. The surface melting initiates at t=1.53 ms and t=237.5 ms for the working distances of 15 and 50 mm, respectively. It should be noted that while the simplified step-wise material removal finite element model gives good prediction of the hole volumes, it neglects several important and most likely competing processes that influence the material removal process. Some of these effects are multiple reflection in the drilling cavity, changes in focusing conditions with increasing hole depth, deposition of droplets on the hole walls, and changes in heat transfer conditions with ultrasonic vibrations. For accurate prediction, these effects need to be taken into account. Also, the proposed finite model uses the experimental melt expulsion time (based on high speed photography) to estimate the critical volume of melt for expulsion from predicted temperature distributions. An accurate condition for melt expulsion based balance of surface tension forces that keeps the melt in place and melt destabilizing forces from ultrasonic vibrations would lead to better predictions

of hole depth.

Conclusions

In this study, a novel ultrasonic vibration-assisted continuous wave laser drilling of AISI 316 stainless steel is reported, and the effect of working distance (15-50 mm) on the geometric features and surface quality of the drilled holes is systematically investigated. For the given laser processing (laser power of 950 W and irradiation time of 0.4 s) and ultrasonic vibration parameters (frequency 20 kHz and vibration displacement of 23 μm), the diameter of the hole does not vary significantly, but the depth of hole increases dramatically with decreasing working distance. The focused laser beams (i.e. shorter working distance) resulted in deeper (up to $\sim$2.5 mm), higher aspect-ratio (up to $\sim$2), and straighter holes. The high speed photography images of the proposed drilling process indicate that the melt expulsion (in the form of sideways melt flow and droplet ejection) under the influence of ultrasonic vibrations initiates after the laser melted pool reaches a critical size/volume. Based on the experimental (high speed photography) observations, the finite element analysis was performed to determine the critical volume of melt for the initiation of melt expulsion under the influence of ultrasonic vibrations. Considering the material removal process as a sequential formation of critical volume of melt pool and subsequent melt expulsion, the finite element analysis showed good prediction of the hole volume for the studied working distances.

4.2.4 Comparative experimental study between Stainless Steel 316 and Ti6Al4V

Introduction

Ultrasonic vibration-assisted continuous wave laser drilling (UVLD) utilizes the mechanical force generated by high frequency ultrasonic vibrations to facilitate the expulsion of the laser melted material. This is in direct contrast to conventional pulsed laser drilling which relies either on expulsion of molten material because of laser-induced recoil pressure (short pulsed laser drilling) and ablation of material (ultra-short pulsed laser drilling) [9, 79]. ULVD has been recently used to drill holes in stainless steel 316 (SS 316) for different irradiation times [101]. It is well established that temperature distribution in the specimen affects the drilling process determining the first droplet ejection time, and hole volumes [79]. For example, high speed camera imaging showed that in UVLD of SS 316 using cw CO_2 laser with 950 W power, 15 mm working distance, and 20 kHz ultrasonic vibration at 20% power out, first droplet was ejected at around 2.2 ms after laser irradiation started and continuous ejection of the molten material, in the form of spherical droplets, was observed till the end. However, variation of thermo-physical properties, such as laser absorption coefficient (A_c) and thermal diffusivity (α), which itself is the product of the thermal conductivity divided by density and specific heat capacity can significantly change conduction heat flow and consequently the temperature distribution in the specimen [15]. Both stainless steel and titanium alloys are competing engineering metallic alloys widely used in diversified structural engineering applications due to their good corrosion resistance, biocompatibility, and excellent mechanical properties [102–105]. These properties favor their widespread aerospace and biomedical applications [106, 107]. Their practical application in the diverse industries requires fabrication of high qual-

ity small holes. Because of high tool wear rate, high heat generation at tool/workpiece spot, low thermal conductivity and low young's modulus, conventional drilling of the Ti-alloy has always been a challenge [108]. Conventional pulse laser drilling, due to its non-contact machining nature and fast machining rate is a promising alternative for drilling holes in Ti-alloys, especially for aerospace engineering applications [22,32]. These two metallic alloys (Ti6Al4V vs. SS 316) have significantly different thermo-physical properties, such as density (4000 vs. 7000 $kg.m^{-3}$), liquidus temperature (1928 vs. 1727 K), and thermal diffusivity (10.7×10^{-6} vs. 5.18×10^{-6} $m^2.s^{-1}$)., thus they can be excellent candidates for a comparative study in which melt expulsion and geometrical properties of the hole drilled with a given laser and ultrasonic vibration parameters can be investigated. The present paper presents the effect of different thermo-physical properties on the hole geometry and mechanism of the hole formation during the ultrasonic vibration-assisted laser surface drilling.

Methods

Laser drilling experiments were performed on 3.5 mm thick Ti6Al4V and stainless steel 316 (SS 316) specimens. Each specimen was polished using 400 grit SiC papers followed by sand blasting to enhance the surface absorption (A_c). Laser surface irradiation was conducted with a continuous wave (cw) CO_2 laser (Ferranti, Manchester, UK) with laser power of 900-1000 W and working distance of 15 mm for the range of laser irradiation times: 30, 50, 100, and 200 ms. The ultrasonic vibration setup consisted of, an ultrasonic power supply, ultrasonic booster, and a 13-mm diameter threaded titanium alloy probe (Sonics & Materials, Inc, Newtown, CT). Specimens were screwed at the top of the ultrasonic probe. The specimens were vibrated vertically (aligned with laser beam) with a frequency of 20 kHz and power output of 20 % (corresponding to displacement of 23 μm) during laser surface irradiation. An scanning electron microscope was used (JEOL Ltd, Tokyo, Japan) to characterize

the surface and cross-sectional features of the laser drilled specimens. An image processing software, Image J, was used to measure the geometric and quality features of the laser drilled holes from the SEM micrographs. Buildup volume was measured with a three-dimensional optical surface profiler (Nanovea, Irvine, CA). A high speed camera (X-StreamVISION; XS-4, IDT) was used to capture the material expulsion during the entire procedure.

Results and Discussion

Surface and cross-sectional scanning electron microscope micrographs of Ti6Al4V and SS 316 specimens, ultrasonic vibration-assisted laser drilled for 30, 50, 100, and 200 ms are presented in Fig.5.34. Surface SEM of both substrates at all 4 laser irradiation

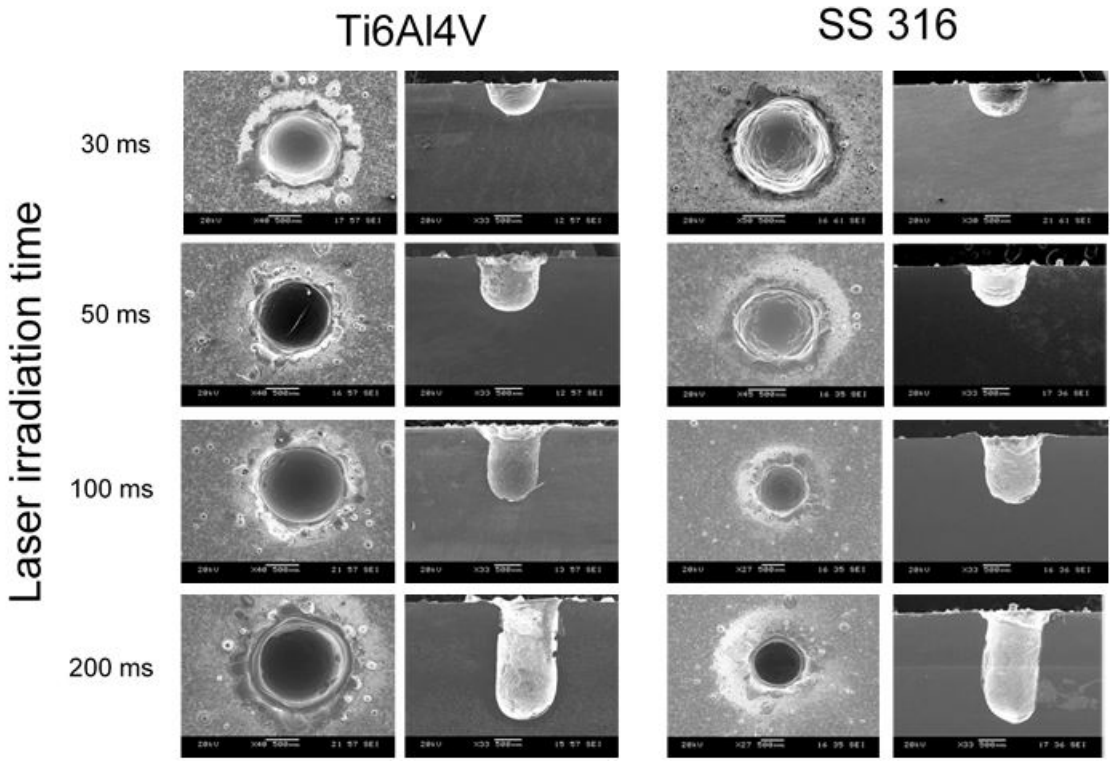

Figure 4.34: Surface and cross-section scanning electron microscopy images of the ultrasonic vibration-assisted laser drilled holes on Ti6Al4V and SS 316 substrates

times show formation of a circular hole entrance, while buildup material and spatters

(as a result of molten material expulsion) are solidified around the rim and periphery of the hole. These images also reveal that buildup around the hole of Ti6Al4V substrate is significantly higher than that in SS 316. Additionally, cross-sectional SEM micrographs also show formation of a semispherical hole shape at shorter laser irradiation time (30 ms). However, as the laser irradiation time increases (in both Ti6Al4V and SS 316 specimens) not only does the depth of the hole increase but also holes exhibit straighter walls (reduction in taper angle). Variation of the hole depth and diameter at laser irradiation times of 30, 50, 100, and 200 ms for Ti6Al4V and SS 316 specimens are plotted in Fig.5.35 (a) and (b), respectively. Except for laser irradiation time of 30 ms, it can be seen that Ti6Al4V shows slightly deeper holes than the SS 316.

Moreover, holes show larges diameter in Ti6Al4V substrate rather than SS 316, especially at larger irradiation times (100 and 200 ms). The higher value of the hole depth and width in Ti6Al4V in comparison to SS 316 can be correlated to their thermo-physical properties differences, specially laser absorption coefficient (Ac) and thermal diffusivity (α). To better understand the heating process during the laser irradiation it is necessary to calculate the temperature profile of the sample over the time. Temperature at the location Z can be calculated using equation below (Eq. 1) [9]:

$$\Delta T_{(z,t)} = \frac{(A_c \times I_0)}{k} \times (4\alpha t)^{\frac{1}{2}} \times ierfc\frac{z}{(4\alpha t)^{\frac{1}{2}}} \tag{4.4}$$

where Δ T, A_c, I_0, k, and α are temperature of the location z, laser absorptivity, laser energy, thermal conductivity, and thermal diffusivity of the specimen, respectively. The variation of the temperature at location Z over the time shows the rate of heating, or in other words, how quickly the temperature at location Z rises. Equation 2 shows the ratio of temperature increase rate (R) at location Z of Ti6Al4V and SS

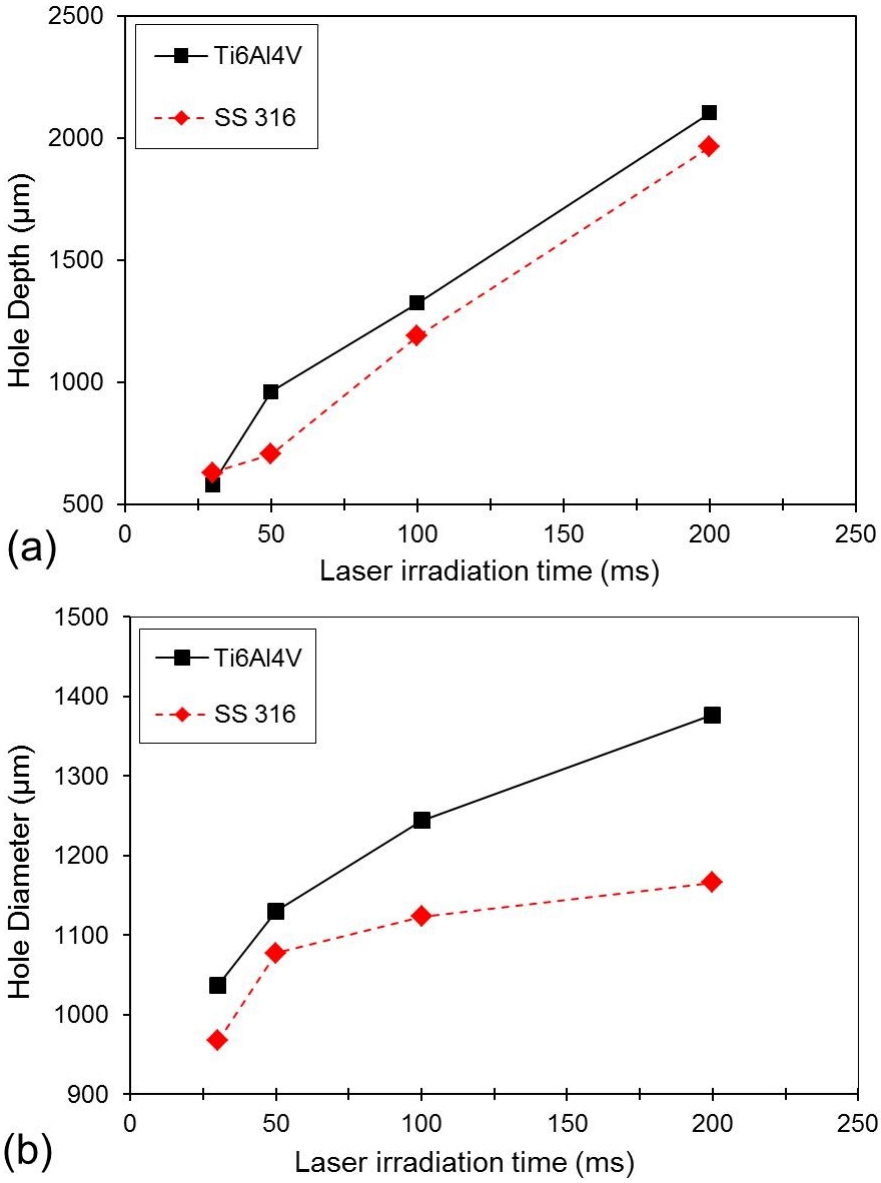

Figure 4.35: Variation of (a) hole depth and (b) hole diameter vs. laser irradiation time drilled by ultrasonic vibration-assisted laser drilling on Ti6Al4V and SS 316 substrates

Table 4.5: Thermo-physical properties of AISI 316 Stainless steel and Ti6Al4V specimen

Parameter	AISI 316 Stainless Steel	Ti6Al4V
Absorption coefficient (%)[1, 15-17]	15	30
Solidus Temp (K) [15]	1697	1878
Liquidus temp (K) [15]	1727	1928
Density of liquid ($kg.m^{-3}$) [15]	7000	4000
Thermal conductivity of solid ($Wm^{-1}\ K^{-1}$) [15]	27	21
Thermal diffusivity ($m^2.s^{-1}$) [15]	5.18×10^{-6}	10.7×10^{-6}

316 specimens.

$$R = \frac{[\partial[\Delta T]_{(z,t)}/\partial t]_{Ti64}}{\partial([\Delta T]_{(z,t)})/\partial t]_{SS316}} = \frac{[A_c]_{Ti64}}{[A_c]_{SS316}} \times (\frac{\alpha_{Ti64}}{\alpha_{SS316}}) \frac{1}{2} \times \frac{k_{SS316}}{k_{Ti64}} \times exp(\frac{z^2}{(4[t\alpha]_{Ti64}}) - \frac{z^2}{(4[t\alpha]_{SS316}})} \tag{4.5}$$

Using the parameters summarized in 4.5, it can be seen that at the laser irradiation time of 30 ms and at the surface of the specimen (Z=0), the ratio of rate of temperature increase (R) is 3.695. Note that R value at the surface (Z=0) is independent of the time. In the proposed mechanism of the molten material ejection in the ultrasonic vibration-assisted laser surface melting, it has been suggested that laser irradiation heats and melts the surface of the specimen, and expulsion occurs when the molten material reaches to the critical volume (V_{Cr}). As it was calculated above, at the given laser parameters, Ti6Al4V experiences higher heating rate than SS 316. However, it should be noted that the critical volume (V_{Cr}) of the Ti6Al4V is higher than the SS 316. Based on the proposed mechanism of droplet expulsion during UVLD, the only driving force for expulsion is the longitudinal vibrational force, generated by ultrasonic vibrator. Since the frequency, power and amplitude of the ultrasonic vibrations (and the acceleration of the ultrasonic tip, consequently) were kept constant in all the experiments, it can be assumed that:

$$F = m_{(SS316)} \times a = m_{Ti64} \times a \rightarrow \rho_{(SS316)} \times V_{Cr(SS316)} = \rho_{(Ti64)} \times V_{Cr(Ti64)}$$
$$\rightarrow V_{CrTi64} = \frac{\rho_{(SS316)}}{\rho_{Ti64}} \times V_{Cr(SS316)} \tag{4.6}$$

Thus, the critical volume (V_{Cr}) of Ti6Al4V for expulsion is about 1.75 times of SS 316. It was previously observed that for the given experimental parameters the the critical volume (V_{Cr}) for SS 316 is 1.82 $\times$ 10^6 μm^3, thus, the critical volume (V_{Cr}) for the Ti6Al4V is 3.18 $\times$ 10^6 μm^3. Fig.5.36 (a) and (b) show the high speed camera images of the UVLD of Ti6Al4V and SS 316, respectively.

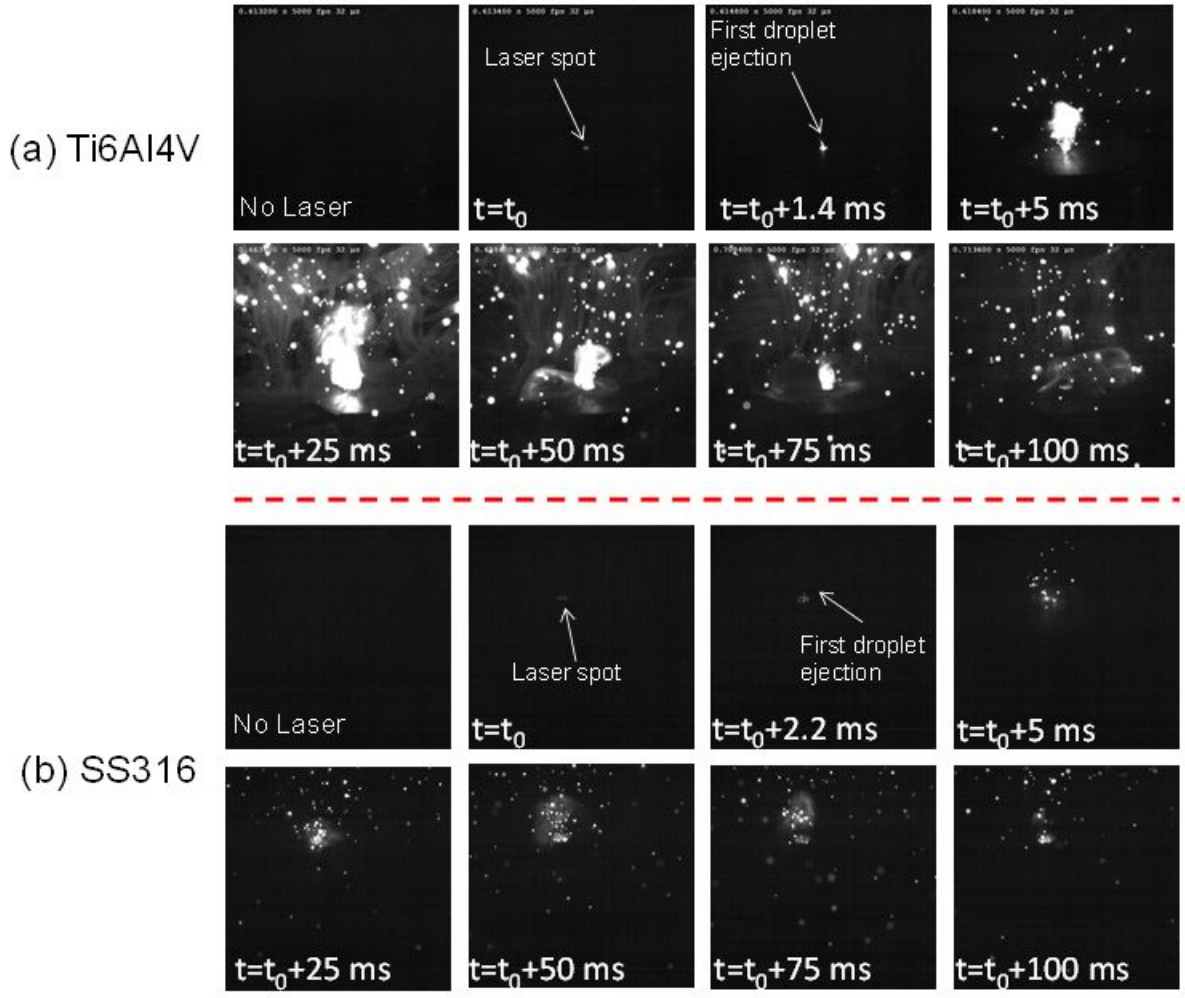

Figure 4.36: High speed camera images of the ultrasonic vibration-assisted laser surface drilling of (a) Ti6Al4V and (b) SS 316 specimens

The selected frames present the surface of the specimen before laser irradiation, starting moment of laser irradiation (t_0), first droplet ejection moment, and 5, 25, 75, and 100 ms after starting the laser irradiation. High speed camera imaging shows a considerable difference in the first droplet ejection time. It can be seen that (Fig.5.37 a) in the Ti6Al4V specimen, first droplet ejects at t_0+1.4 ms (average of all irradiation times: 1.45 ms) while this times increases to t_0+2.2 ms (average of all irradiation times: 2.06 ms) in SS 316 specimen. The significant difference between temperature rise rates explains the earlier ejection of the first molten droplet in Ti6Al4V specimen. Although the liquidus temperature of Ti6Al4V (T_L: 1928 K) [109] is considerably higher than the liquidus temperature of SS 316 (T_L: 1727 K), surface of the Ti6Al4V specimens melts faster and first droplet ejects 0.61 ms (in average) earlier than SS 316 specimens. Captured images at 5, 25, 50, 75, and 100 ms show a continuous expulsion of the molten material as spatters.

However, during the UVLD of Ti6Al4V specimen larger and brighter spatters with higher density of spatters per unit area in each frame in comparison to SS 316 specimen is observed. Formation and expulsion of the larger droplets can be related to the significant difference in the the critical volume (V_{Cr}) of Ti6Al4V and SS 316 specimens. As discussed above, Ti6Al4V has to form larger (1.75 times) the critical volume (V_{Cr}) than SS 316 for ejection which results in expulsion of the larger droplets. Fig.5.37 b presents the volume of the hole for UVLD of Ti6Al4V and SS 316 at laser irradiation times of 30, 50, 100, and 200 ms. It was discussed that Ti6Al4V is heated up faster, this the critical volume (V_{Cr}) is formed sooner than SS 316. Thus, at any given time, more molten material is formed and ejected in Ti6Al4V specimen and results in higher volume of the hole. The Ti6Al4V to SS 316 volume hole ratio for laser irradiation times of 30, 50, 100, and 200 ms is 2.02, 2.13, 2.09, and 1.43, respectively.

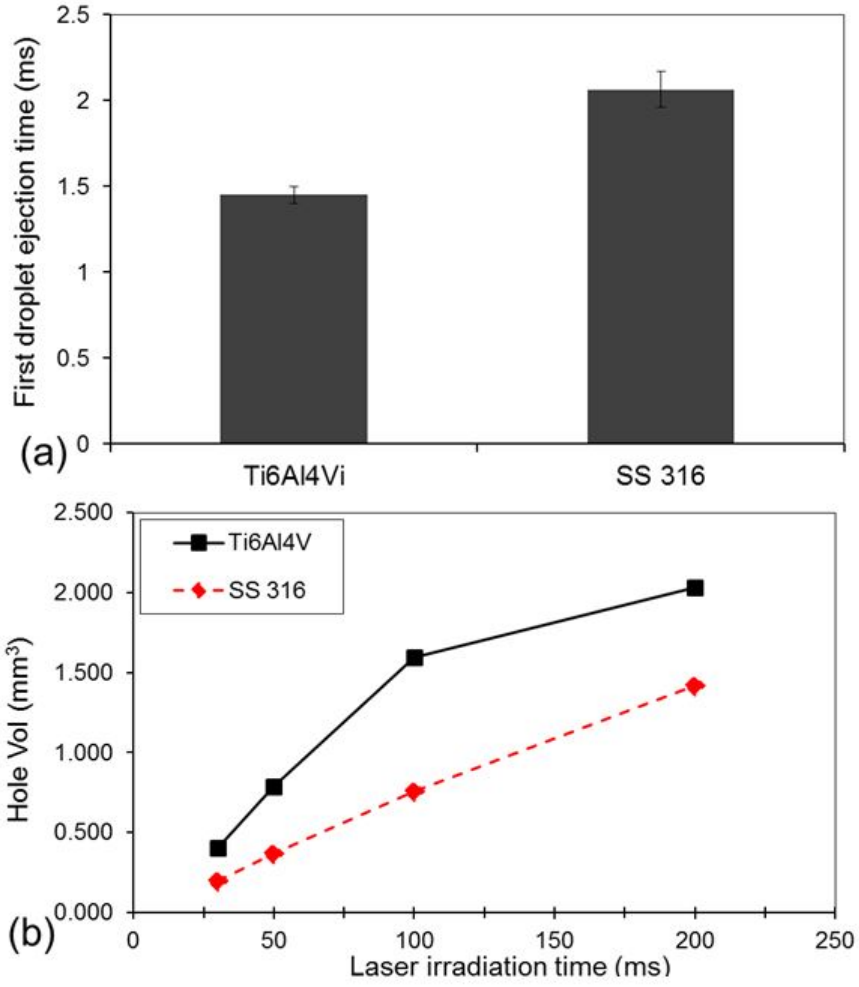

Figure 4.37: Variation of the (a) first droplet ejection and (b) hole volume vs. laser irradiation time drilled by ultrasonic vibration-assisted laser drilling on Ti6Al4V and SS 316 substrates

Conclusion

In this study, ultrasonic vibration-assisted continuous wave laser drilling of stainless steel 316 and Ti4Al4V is reported, and the effect of thermo-physical properties on the geometric features of the drilled holes and expulsion of the molten droplet is investigated. Scanning electron microscopy showed formation of holes with circular entrance. The geometrical features of the hole are significantly affected by thermo-physical properties. For the given laser processing and ultrasonic vibration parameters, Ti6Al4V specimens exhibit deeper, wider, and higher volume of the drilled hole. Furthermore, high speed camera images of the drilling process showed earlier ejection of the first molten droplet in Ti6Al4V specimen.

4.2.5 The influence of ultrasonic frequency (20 kHz vs. 40 kHz) on melt expulsion during ultrasonic vibration-assisted laser drilling of stainless steel

Introduction

Conventional materials processing and manufacturing technologies have undergone continuous improvements and new technologies have been regularly developed to address several challenges related to productivity, process efficiency, part complexity and quality, scalability, materials compatibility, and manufacturing economics. Recently, applications of ultrasonic vibrations in materials processing are rapidly expanding to further improve the outcomes of conventional processes or enable additional manufacturing flexibility [38, 110–113]. While ultrasonic vibrations have established applications in materials cleaning, sonochemistry, liquid metal processing [114], atomization [115], and plastic and metals welding [116, 117], their applications as an assistance or aid to advanced manufacturing processes such as precision machining [118, 119], laser processing [49, 53], and additive manufacturing [120, 121] are rapidly proliferating. These ultrasonic vibration-assisted manufacturing processes offer several advantages over the conventional processes. The outcomes of these processes depend not only on the primary process parameters but also on ultrasonic parameters namely vibration frequency and amplitude. However, the effect of these ultrasonic parameters on the process outcomes is not well investigated for these emerging ultrasonic vibration-assisted manufacturing processes. The effects of ultrasonic vibration assistance to conventional machining processes such as drilling on machining characteristics (machining force, chip morphology, workpiece quality, and tool wear) are widely investigated for difficult-to-machine materials. Liao et al. [39] investigated ultrasonic vibration-assisted drilling of Inconel 718 superalloy with a range of vibration parameters (amplitudes of 4-12 and 8-17 μm at vibration frequencies

of 31.8 and 20.3 kHz, respectively). It was reported that ultrasonic vibration assistance resulted in general reduction in chip size, increase in proportion of segmented chips, reduction in thrust force, and increase in tool life. The effect of vibration amplitude was observed to be more pronounced than the frequency on the machining characteristics, leading to the conclusion that high frequency and small amplitude vibrations give better results for ultrasonic vibration-assisted drilling of the superalloys. Azarhoushang and Akbari [44] also reported that multiple impact interaction between tool and workpiece during ultrasonic vibration-assisted drilling (frequency of 21 kHz and amplitude of 10 μm) resulted in the formation of discontinuous finer chips for Inconel 738-LC alloy, resulting in overall improvement in surface finish and tool life. Kadivar et al. [122] also investigated the effect of ultrasonic parameters (frequency of 22 kHz and amplitudes of 5-15 μm) on the machining characteristics for ultrasonic vibration-assisted drilling of Al/SiCp metal matrix composites. It was observed that the ultrasonic vibrations of lower amplitudes resulted in higher improvements in machining performance measured in terms surface finish and burr height. The effect of ultrasonic parameters (frequency 10-30 kHz and amplitude 5-25 μm) on the chip morphology and machining forces was also investigated for ultrasonic vibration-assisted drilling of cortical bone by Alam et al [123]. The machining force and torque for the ultrasonic vibration-assisted drilling were significantly lower than that for conventional drilling. For the ultrasonic vibration-assisted drilling, the machining force showed continuous reduction with increasing frequency from 10 to 30 kHz (for the constant amplitude of 10 μm) while the significant reduction in force was observed with increasing vibration amplitude from 5 to 15 μm (for the constant frequency of 20 kHz). Further increase in vibration amplitude from 15 to 25 μm did not result in any additional improvement in machining force. Clearly, most of these studies on ultrasonic vibration-assisted drilling reported improved chip removal and reduction in forces for a range of materials. These studies also demonstrated that high frequency

and small amplitude ultrasonic vibrations offer optimum improvements in machining performance for the ultrasonic vibration-assisted drilling. Recently, application of ultrasonic vibration assistance in laser-based manufacturing processes such as additive manufacturing, surface melting, and drilling is attracting significant attention. Cong and Ning [124] investigated the influence of the application of vertical vibrations of frequency 41 kHz to the substrate during direct energy deposition (DED) based laser additive manufacturing of AISI 630 stainless steel. It was observed that the ultrasonic vibration assistance during additive manufacturing improves in powder efficiency, alleviates balling effect, reduces defects (cracks and porosity), and refines grain structure of the built parts. The effects such as cavitation and acoustic streaming due to ultrasonic vibrations, also observed in liquid metal processing, are likely the causes of desired metallurgical effects observed for ultrasonic vibration-assisted additive manufacturing. Biswas et al. [125] also observed similar grain refinement effects due to ultrasonic vibration assistance (frequency of 20 kHz) to laser melting of Ti-6Al-4V. In these studies [124, 125], vertical ultrasonic vibrations are applied directly to substrate while being irradiated with relatively defocused laser beam for melting or deposition. However, Biswas et al. [125][21] also reported that the application of intense ultrasonic vibrations to the substrate during laser melting cause some expulsion of molten material from the melt pool, creating surface craters upon solidification. The melt expulsion characteristics during ultrasonic vibration-assisted laser melting of AISI 316 stainless steel was investigated by Alavi and Harimkar [79]. It was observed that the application of ultrasonic vibrations (frequency of 20 kHz and displacements 23-51 μm) during laser melting delayed the interaction of laser with the material due to enhanced convection effects and caused expulsion of melt from the pool. For the given laser irradiation time, increasing ultrasonic vibration displacements resulted in shallower craters with thinner resolidified layer, indicating higher convection enhancement and effective melt expulsion at higher displacements.

Alavi and Harimkar [80] further investigated the feasibility of utilizing the observations of melt expulsion during ultrasonic vibration-assisted laser melting for designing material removal processes. They reported that the application of ultrasonic vibrations (frequency 20 kHz and displacements 23-51 μm) to the AISI 316 stainless steel substrate during laser surface melting with a focused laser beam results in significant melt expulsion from the substrate, creating deep holes (up to 1.5 mm with aspect ratio of about 3.5). The depth of hole continuously increased with increasing ultrasonic displacement for the proposed ultrasonic vibration-assisted laser drilling (UVLD) of steel. Alavi and Harimkar [101,126] further investigated the effect of laser processing parameters (irradiation time and focusing conditions) on the geometric and quality aspects of the holes drilled in AISI 316 stainless using UVLD. While most of these studies reported beneficial effects of the simultaneous application of ultrasonic vibrations during laser-based manufacturing processes (additive manufacturing, melting, and drilling), systematic investigations on the effects of vibration parameters on the process outcomes were not performed. In this study, systematic effect of ultrasonic vibration frequency (20-40 kHz) and amplitude (16-32 μm) on the melt expulsion characteristics in early stages of UVLD of AISI 316 is investigated using high speed camera imaging. Based on the analysis of initiation of droplet ejection from the melt pool and particle size of ejected droplets, mechanisms of droplet ejection based on capillary wave theory are proposed. Furthermore, the effect of ultrasonic vibration parameters on the development of geometric and quality features of the holes drilled with UVLD is analyzed.

Experimental procedure

Laser drilling experiments were conducted on AISI 316 stainless steel specimens. Specimens were machined to 3.5 mm thickness, followed by sand paper polishing (up to 400 grit size) to remove the machining marks. Surface of the specimens was sand

blasted to improve the laser beam absorption. Specimens were ultrasonically cleaned in Ethanol and distilled water. A continuous wave (cw) CO_2 laser (Ferranti, Manchester, UK) at the laser power of 900 W was used for laser irradiation. Ultrasonic vibration generators (Sonics & Materials, Inc, Newtown, CT) consisted of two power supplies (frequencies of 20 kHz and 40 kHz) with ultrasonic probe of 13 mm diameter were used for vibration the specimens at vibration displacements of 16, 24, and 32 μm. Stainless steel specimens were screwed on top of the ultrasonic probe and ultrasonic vibrations were perpendicular to the surface of the specimen. The schematic of the experimental setup is presented elsewhere [101]. Laser drilling experiments were performed for 100 ms of laser irradiation, working distance of 5 mm and ultrasonic vibrations were maintained during the entire duration of laser irradiation. A shielding gas (Ar) was used to prevent surface oxidation during laser drilling. A three-dimensional optical surface profiler (Nanovea, Irvine, CA) was used to measure the build-up volume of the material around the laser drilled hole periphery. A scanning electron microscope was used (JEOL Ltd, Tokyo, Japan) to characterize the surface and cross-sectional features of the laser drilled specimens. An image processing software, Image J, was used to measure the geometric and quality features of the laser drilled holes from the SEM micrographs. A high speed camera (X-StreamVISION; XS-4, IDT) was used to image the processes in early stages of laser drilling. To capture the illuminated droplets and melt pool (due to laser light irradiation), the images were recorded with 8000 frames/s.

Results and discussion

Analysis of droplet ejection during UVLD

Fig. 4.39 shows the selected sequence of the frames capturing the major incidents during UVLD of stainless steel performed with ultrasonic vibration displacements of 16, 24, and 32 μm at the vibration frequencies of 20 and 40 kHz. The irradiation

of laser on the vibrating surface causes surface heating and eventual melting of the substrate. For all the investigated parameters, the first two frames (Fig. 4.39a-b), captured at the spacing of 0.125 ms, show the first sign of transition to laser-interaction regime, indicated by the appearance of the bright spot on the surface of the substrate. The time corresponding to the second frame was considered the initiation of laser irradiation (t0). This was also confirmed from the fact that the time from this frame to the last frame showing laser interaction corresponds exactly to the irradiation time used in this investigation (100 ms). The continued laser irradiation beyond t0 causes laser heating and melting, and the melt pool size increases and reaches a critical volume before the initiation of droplet ejection from the surface of melt pool (Fig. 4.39c). From the high speed camera images, it is difficult to identify the initiation of melting i.e. the transition from heating to melting. The time corresponding time to the initiation of droplet ejection (t1) for the investigated processing parameters is also indicated on the frames. Depending on the ultrasonic vibration parameters (displacement and frequency), the droplet ejection from the laser melted pool begins at about 0.75-2.5 ms during laser irradiation. The droplet expulsion in the form of a stream continues during the entire duration of remaining laser irradiation time (Fig. 4.39d).

From the observations of the high speed camera images, the proposed sequence of events leading to the formation of hole during UVLD is shown in Fig. 4.40.

The variation of droplet ejection initiation time (t1) with ultrasonic vibration displacements at the vibration frequencies of 20 and 40 kHz is shown in Fig. 4.41. Clearly, for both ultrasonic vibration frequencies, the droplet ejection initiation time decreases with increasing ultrasonic vibration displacement from 16 to 32 μm.

Furthermore, the droplet ejection initiation time at all vibration displacement is much shorter for vibration frequency of 40 kHz when compared to 20 kHz. The effect of vibration displacement is much more dominant than vibration frequency on the

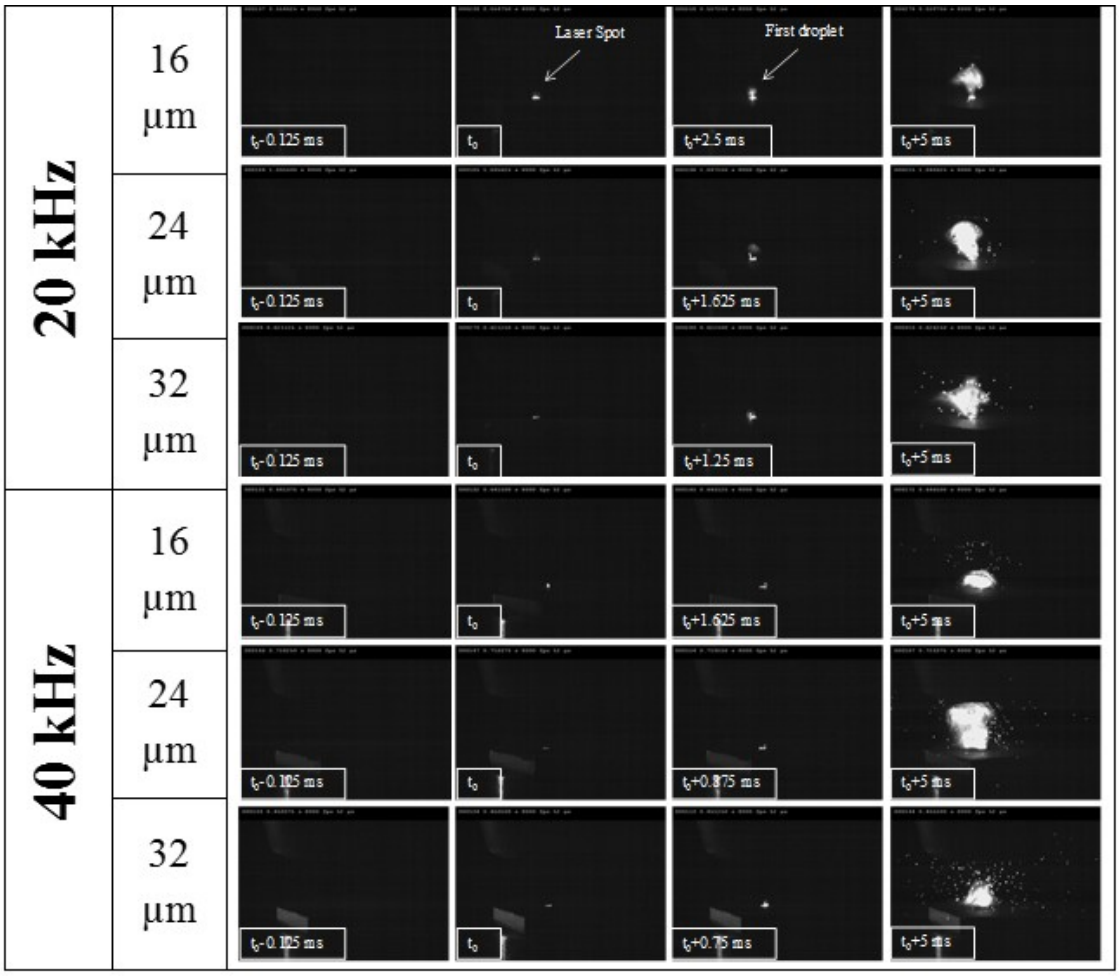

Figure 4.38: High speed camera images showing: (a-b) initiation of laser interaction, (c) first droplet ejection, and (d) continued ejection of droplets during UVLD of AISI 316 steel for ultrasonic vibration displacements of 16, 24, and 32 μm at frequencies of 20 and 40 kHz

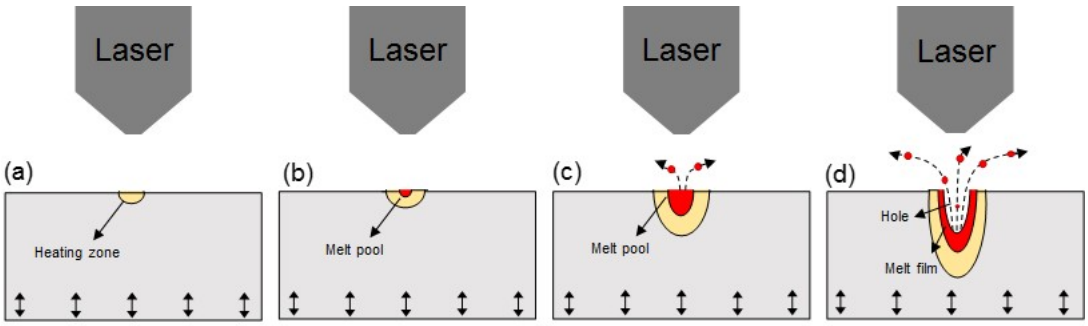

Figure 4.39: Schematic of the sequence of events leading to the formation of hole during UVLD: (a) laser heating, (b) initiation of laser melting, (c) formation of critical volume of melt pool for the initiation of droplet ejection, and (d) continued ejection of a stream droplets during continued laser irradiation.

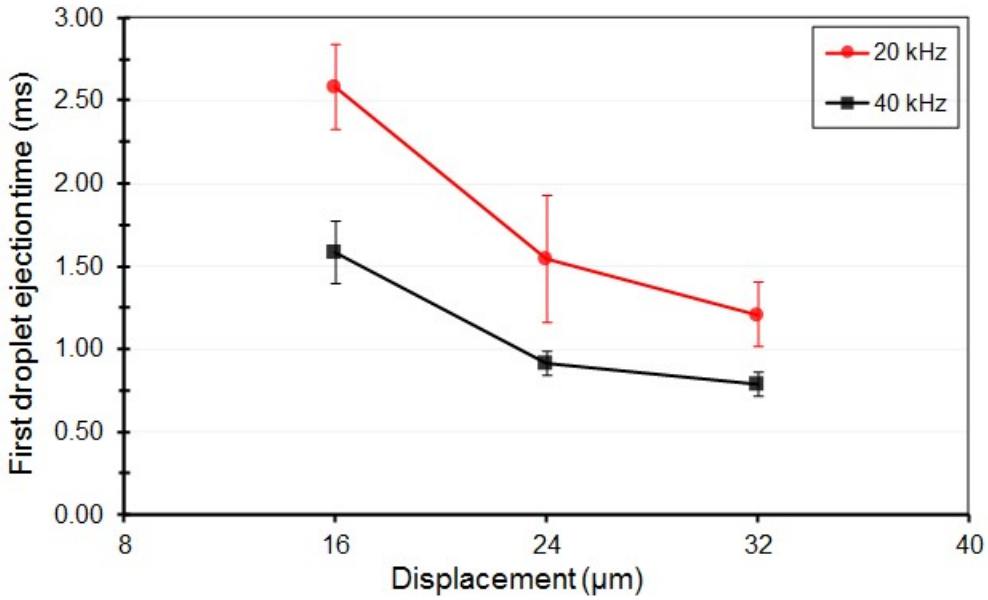

Figure 4.40: Variation of droplet ejection initiation time with ultrasonic vibration displacement for vibration frequencies of 20 and 40 kHz during UVLD of AISI 316 steel.

reduction in droplet ejection initiation time. For example, doubling the ultrasonic vibration displacement from 16 to 32 μm causes about 53% and 50% reduction in droplet ejection initiation time for vibration frequencies of 20 and 40 kHz, respectively. The effect of frequency on the droplet ejection initiation time progressively diminishes with increasing ultrasonic vibration displacement. The doubling of vibration frequency from 20 to 40 kHz results in about 39% and 34% reduction in droplet ejection initiation time for vibration displacements on 16 and 32 μm, respectively. At a given vibration frequency, the higher vibration displacement provides higher vertical speed and consequently higher acceleration to the substrate being laser melted at the surface. Higher vibration frequency at given displacement also means higher number of vibration cycles are applied to the melt pool per unit time. It can be concluded that the ultrasonic vibrations of higher vibration displacement and frequency impart higher destabilizing force on the melt pool causing earlier ejection of the droplets from the melt pool. However, it must be noted that the simultaneous application of ultrasonic vibrations to the substrate significantly modifies the heat transfer processes. It has been reported that the ultrasonic vibrations cause enhancement of surface convection both in air and liquid media [57, 127]. Depending on the ultrasonic vibration parameters and system configuration, an increase in convection coefficients up to 25 times has been reported due to ultrasonic vibration assistance. In laser materials processing, the overall heat balance at the laser irradiated surface is determined by the absorbed laser energy at the surface and convective and radiative heat losses from the surface and is given by the heat transfer equation [9]:

$$-k[(\delta T/\delta x) + (\delta T/\delta y) + (\delta T/\delta z)] = \delta I_0 - \varepsilon\sigma[T^4 - [T_0]^4] - h[T - T_0] \qquad (4.7)$$

where k is the thermal conductivity, δ is the absorptivity, I_0 is the incident laser intensity, ε is the emissivity, σ is the Stefan-Boltzmann constant, and h is the convective heat transfer coefficient. The enhancement of surface convection, and consequent

loss of energy, is also expected during simultaneous application of ultrasonic vibrations during laser irradiation as in early stages of UVLD. It is expected that such enhancement of surface convection effects will increase with increasing severity of the ultrasonic vibrations as defined by higher vibration displacement and frequency. The higher convective losses from the laser irradiated surface during UVLD would then cause delays in laser interactions with the materials. In fact, it was reported [79] that the application of ultrasonic vibrations of frequency 20 kHz to the AISI 316 steel substrate during laser surface irradiation completely eliminates the possibility of surface melting with the similar laser processing parameters (laser power of 900 W, irradiation time of 0.30 s, and laser beam diameter of 7 mm) that cause surface melting of the substrate without the application of ultrasonic vibrations. Only heat affected zone was observed for the samples when they were laser irradiated with simultaneous application of ultrasonic vibrations to the samples. It was also reported that the size of the heat affected zone decreases and the heat affected zone eventually diminishes as the displacement of vibrations increases with the similar laser processing parameters and vibration frequency. Clearly, the enhancement of surface convection during UVLD is likely to cause increasing delays in laser surface interaction effects such as surface melting with increasing ultrasonic vibration displacement and vibration frequency. However, as observed from the high speed camera imaging, the droplet ejection initiation time during UVLD decreases with increasing ultrasonic vibration displacement and vibration frequency. It appears that even with stronger surface convection enhancement effects and consequent delays in surface melting, the higher destabilizing force offered by the higher ultrasonic vibration displacement and vibration frequency to the melt pool eventually causes the early ejection of droplets from the melt pool during UVLD. The critical volume of the melt pool for the initiation of droplet ejection is also likely to be much smaller at higher ultrasonic vibration displacement and frequency during UVLD. To further understand the melt ejection

Table 4.6: Theoritical and experimental particle sizes of expelled droplet during ultrasonic vibration-assisted laser drilling

Frequency	Theoretical particle size	Vibration displacement		
		16 μm	24 μm	32 μm
20 kHz	83.4 μm	90.0±21.3 μm	84.5±24.7 μm	77.2±24.0 μm
40 kHz	52.6 μm	55.2±9.5 μm	66.2±17.6 μm	49.1±13.0 μm

mechanisms during UVLD, the size and distribution of the solidified droplets/particles were analyzed (Fig. 4.42).

The particles ejected during UVLD at all the processing parameters were highly spherical and showed dendritic surface morphology, indicating rapid solidification of droplets in-flight. It was observed that the particle size distribution was relatively narrower for ultrasonic vibration frequency of 40 kHz at all the investigated vibration displacement. Also, the ejected particles were relatively smaller for the 40 kHz at the given ultrasonic vibration displacement. The average particle size for all the processing parameters is listed in Table 4.6.

The average particle size was in the ranges of about 77-90 μm and 49-55 μm for the ultrasonic vibration frequencies of 20 and 40 kHz, respectively. The effect of ultrasonic vibration frequency was much more pronounced on the average particle size. The early stage ejection of droplets during UVLD is likely to be due to mechanisms very similar to capillary wave mechanisms during ultrasonic atomization of materials. In ultrasonic atomization, the liquid film of uniform thickness on the vibrating surface becomes unstable and forms ripples (capillary wave). During atomization, the displacement of the capillary wave increases and the peaks of the wave break from the liquid film forming droplets. Lang [115] proposed that the average particle size during ultrasonic atomization is proportional to the capillary wavelength and is given

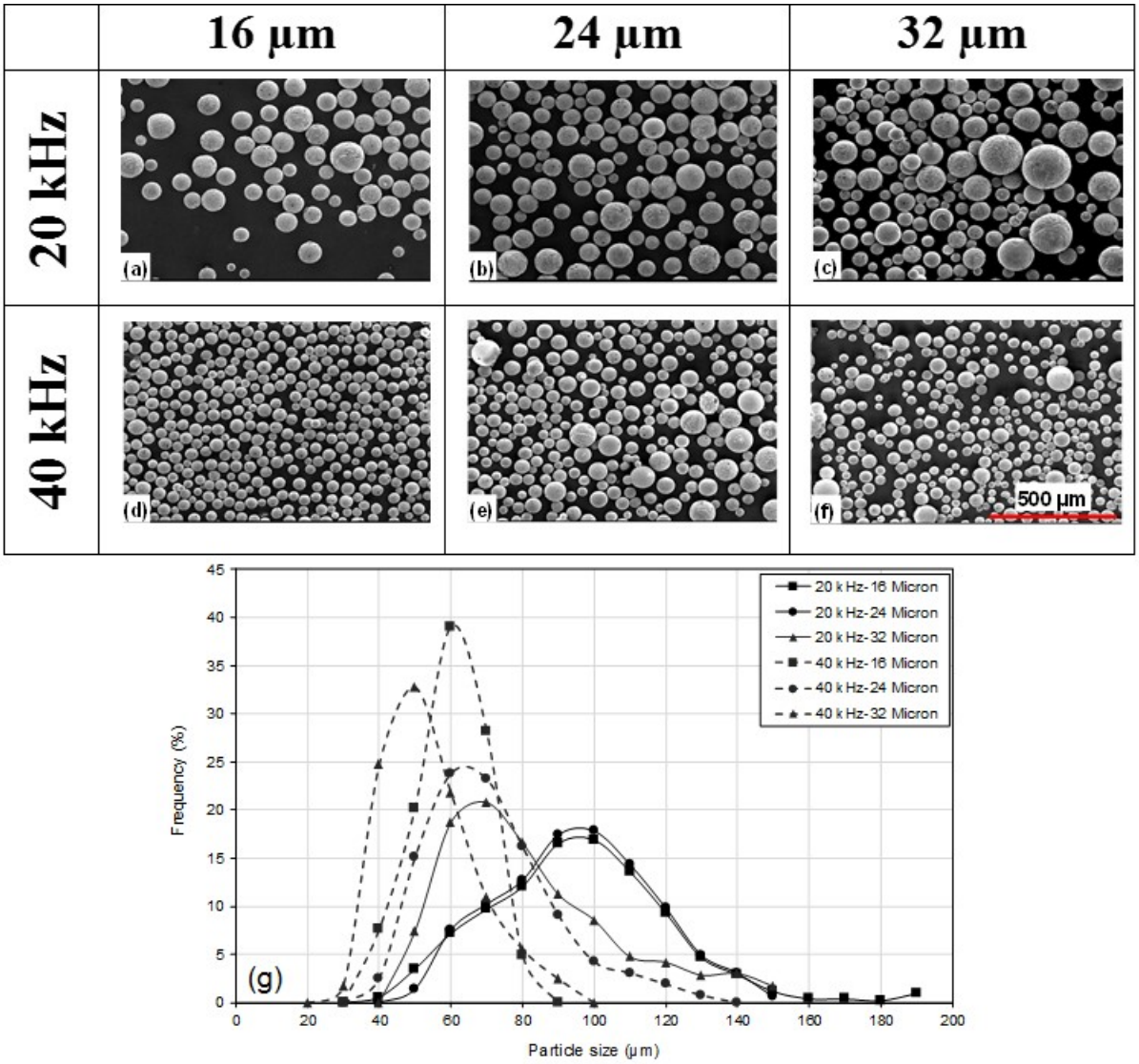

Figure 4.41: (a-f) SEM micrographs of ejected particles and (g) size distributions of particles ejected during UVLD of AISI 316 steel for ultrasonic vibration displacements of 16, 24, and 32 μm at frequencies of 20 and 40 kHz.

by:

$$D = 0.34 \times (\frac{8\pi\sigma}{\rho f^2})\frac{1}{3} \tag{4.8}$$

where σ, ρ, and f are surface tension of the liquid (N/m), density of the liquid (kg/m^3), and frequency of ultrasonic vibrations (Hz), respectively. Assuming that the capillary wave hypothesis is applicable in the case of UVLD, the average particle size could be calculated using thermo-physical properties of AISI 316 stainless steel at melting temperature (σ: 1.77 J/m^2 [128], ρ: 6950 kg/m^3 [82]). The average particle size was calculated to be 83.4 and 52.6 μm for vibration frequencies of 20 and 40 kHz, respectively. It must be noted that the thickness of liquid film in ultrasonic atomization is uniform while the laser irradiation on the surface with Gaussian beam forms semi-ellipsoidal melt pool with highest depth at the center of the pool. Such non-uniform depth of the melt pool is likely to cause capillary waves of varying wavelengths, resulting in ejection of droplets over a wider size distribution as observed. Also, the laser melted pool always exhibits a temperature distribution with highest temperature at the surface, and the surface temperature of the melt pool is often exceeds the melting temperature. Nevertheless, the calculated particle size based on capillary wave hypothesis is in reasonable agreement with the measured particle size, indicating the capillary wave mechanism in early stages of UVLD. The schematic of the capillary wave mechanism for the ejection of droplets from the melt pool in early stages of UVLD is presented in Fig. 4.43.

Geometrical and quality aspect of holes drilled with UVLD The surface and cross-sectional SEM images of the holes drilled using UVLD for ultrasonic vibration displacements of 16, 24, and 32 μm at vibration frequencies of 20 and 40 kHz are presented in Fig 4.44. The holes drilled with all the UVLD parameters exhibited good circularity at the entrance. The heat affected zone, indicated by the brighter contrast around the holes, becomes increasingly larger with increasing vibration dis-

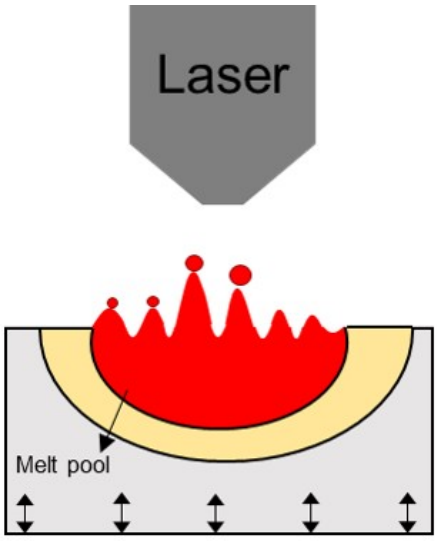

Figure 4.42: Schematic of the capillary wave mechanism for the ejection of droplets from the melt pool in early stages of UVLD.

placement at both 20 and 40 kHz. The width of the heat affected zone was in the range of 400-700 μm. The surface of the specimens also show significant spatter due to deposition of ejected droplets. The spatter droplets are relatively bigger and more closely spaced near the hole rims. The holes drilled with higher vibration displacement (32 μm) also show significant buildup of material around the rim of the holes. The material build up is not uniform along the hole rims. The material build up is relatively distributed for holes drilled with 20 kHz while it is more pronounced on two sides of the hole for 40 kHz. The cross sectional SEM images show that the laser drilled holes were significantly tapered, especially the deeper holes drilled at higher vibration displacements. The ejected droplets during laser drilling also deposited and resolidified on the hole walls, resulting in rougher surface features on the inside walls of the holes.

The variation of hole depth and diameter with ultrasonic vibration displacement for vibration frequencies of 20 and 40 kHz is presented in Fig. 4.45. The results show that depending on laser processing and ultrasonic vibration parameters, the proposed

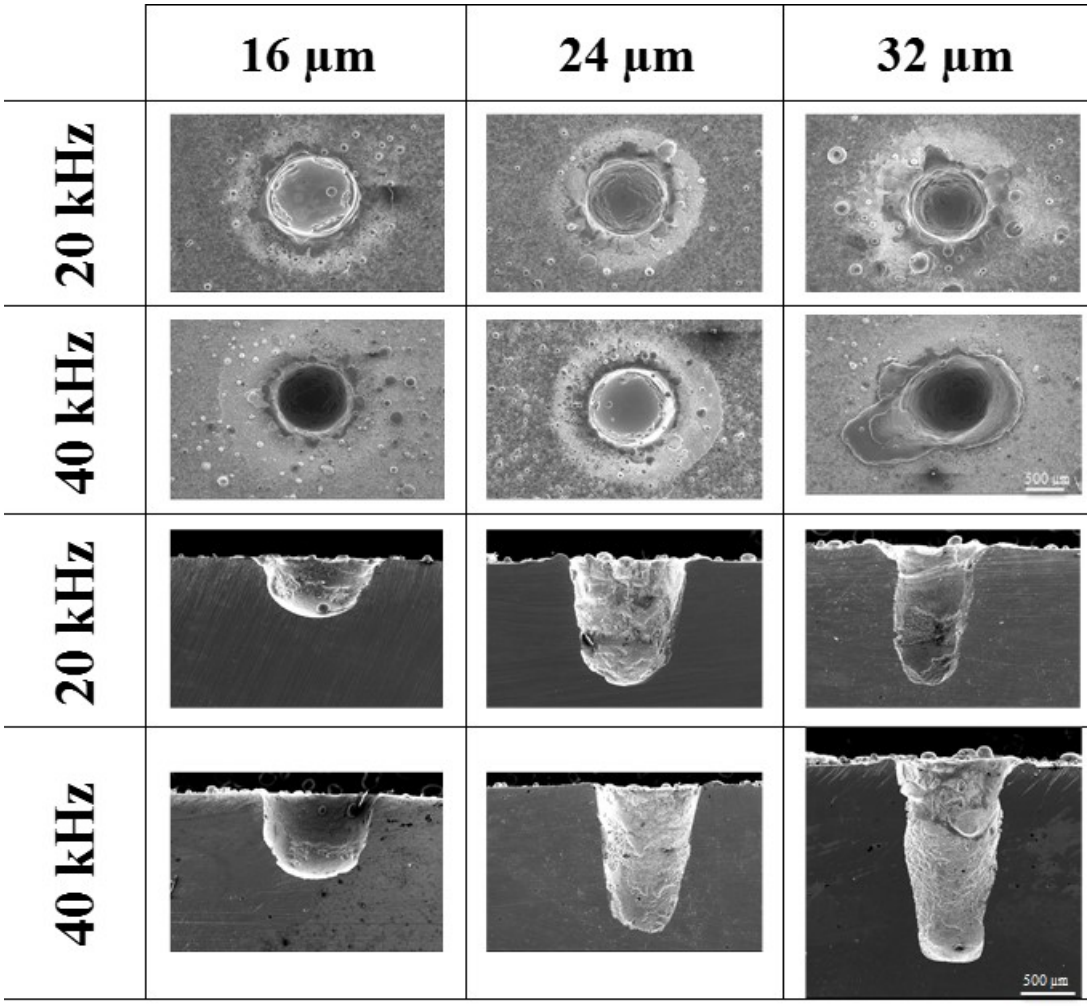

Figure 4.43: Surface and cross-sectional SEM images of the laser drilled holes in AISI 316 steel for ultrasonic vibration displacements of 16, 24, and 32 μm at frequencies of 20 and 40 kHz.

UVLD process is capable of drilling sub-2 mm deep holes with diameter as small as 900 μm. While the diameter of the holes shows general decreasing trend, the depth of the hole increases almost linearly with the increasing ultrasonic vibration displacement for both 20 and 40 kHz. The UVLD with higher ultrasonic vibration frequency (40 kHz) resulted in the formation of deeper and narrower holes. The ultrasonic vibration displacement has more pronounced effect on the geometric aspects (hole depth and diameter) of the drilled holes than the vibration frequency. For example, the doubling of vibration displacement from 16 to 32 μm resulted in about 124 and 143% increase in hole depth for 20 and 40 kHz, respectively. On the other hand, doubling the ultrasonic vibration frequency from 20 to 40 kHz resulted in about 24, 31, and 35% increase in hole depth for ultrasonic vibration displacements of 16, 24, and 32 μm, respectively. The effect of vibration frequency on the variation in diameter is much more pronounced at the lower vibration displacements (16 and 24 μm). The dimeter of the laser drilled hole is about 930 μm for vibration displacement of 32 μm at both 20 and 40 kHz. The aspect ratio of the holes drilled with different ultrasonic parameters is also indicated in the Fig. 4.45. The highest aspect ratio of 2.0 was observed for the holes drilled with highest ultrasonic vibration displacement (32 μm) and vibration frequency (40 kHz) used in this investigation. The increase in hole depth with increasing ultrasonic vibration displacement and frequency could be directly linked with the melt expulsion characteristics in early stages of drilling. Note that the high speed camera imaging showed that higher ultrasonic vibration frequency and displacement resulted in earlier initiation of droplet ejection, resulting in overall longer duration for material removal in the form of stream of ejected droplets and formation of deeper holes. The pronounced effect of ultrasonic vibration displacement is consistent for both the variation of droplet ejection initiation time and the hole depth. It was also observed that the entrance diameter of the holes decreases with increasing ultrasonic displacement and vibration frequency (Fig. 4.45). The SEM images also

showed that holes become narrower, and hence tapered, with increasing depth of the holes (Fig. 4.44). The walls of the holes are also covered with deposited droplets and rims with build-up material for deeper holes. It appears that the reduction in diameter of the holes with increasing ultrasonic vibration displacement and frequency is directly correlated with the depth of the holes. Once the ejection of the droplets is initiated during the early stages of UVLD, the melt front advances downward and hole depth increases with continued laser irradiation. However, the complete ejection of droplets from the holes becomes increasingly difficult with increasing hole depth. The droplets ejected from deeper melt front impinge and re-solidify on the hole walls and near the rim as observed from the SEM images, causing overall reduction in diameter of the holes. While droplet ejection is the dominant mechanisms of material removal during UVLD, it also appears that some vertical flow of molten material also contributes to material removal as observed from the layered build-up of material at the hole rims and deposition of material on the hole walls.

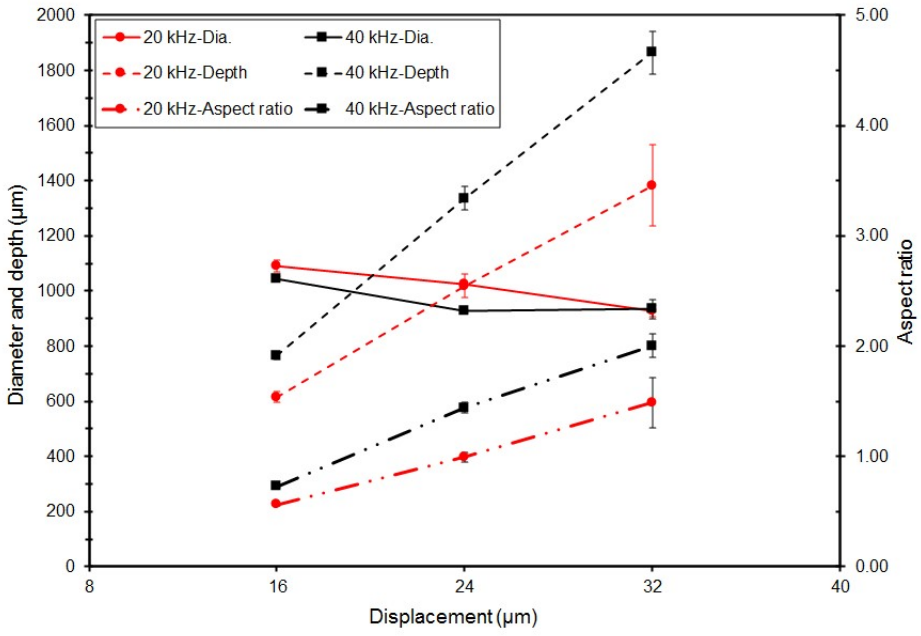

Figure 4.44: Variation of the hole diameter, depth, and aspect ratio with vibration displacement for frequencies of 20 and 40 kHz during UVLD of AISI 316 steel.

The 3D surface profiles of the holes and measured volume of build-up material at the hole rims are presented in Fig. 4.46. In general, the build-up volume increases with increasing ultrasonic vibration displacement consistent with corresponding increase in depth of the holes. The volume of build-up area for holes drilled with lower ultrasonic displacement (16 and 24 μm) at both 20 and 40 kHz was less than $4\times\ 10^{-3}$ mm^3 ($\sim$0.2% of the total hole volume). However, significant difference in build-up volume was observed for holes drilled with higher ultrasonic vibration displacement (32 μm). The volume of the build-up material for holes drilled with the vibration displacement of 32 μm was about $13.7\times\ 10^{-3}$ and $114\times\ 10^{-3}$ mm^3 for ultrasonic vibration frequency of 20 and 40 kHz, respectively. Clearly, the deeper holes are associated with larger build-up material due to difficulty in complete ejection of droplets and consequent deposition of droplets on the hole rims. Also, additional mechanism such as upward flow of molten material on the hole walls, especially for deeper holes, are likely to contribute to the build-up of material at the hole rims.

Conclusions For UVLD of AISI 316 steel, the melt expulsion characteristics and geometric/quality features of the drilled holes were significantly influenced by ultrasonic vibration parameters (investigated frequencies of 20-40 kHz and displacements of 16-32 μm) for the given laser processing parameters. It was observed that increasing both ultrasonic vibration frequency and displacement resulted in earlier initiation of droplet ejection from the melt pool, resulting in the formation of deeper holes for the given laser irradiation time (100 ms). The effect of increasing ultrasonic vibration displacement was much more pronounced than the frequency on the reduction in droplet ejection initiation time and improvement in hole depth. The analysis of the solidified ejected droplets indicated the presence of capillary wave mechanism for droplet formation in the early stages of UVLD. The laser drilled holes, especially the deeper holes drilled with higher vibration frequency and amplitude, were also associated with defects such as material build-up at on the hole walls and rims primarily

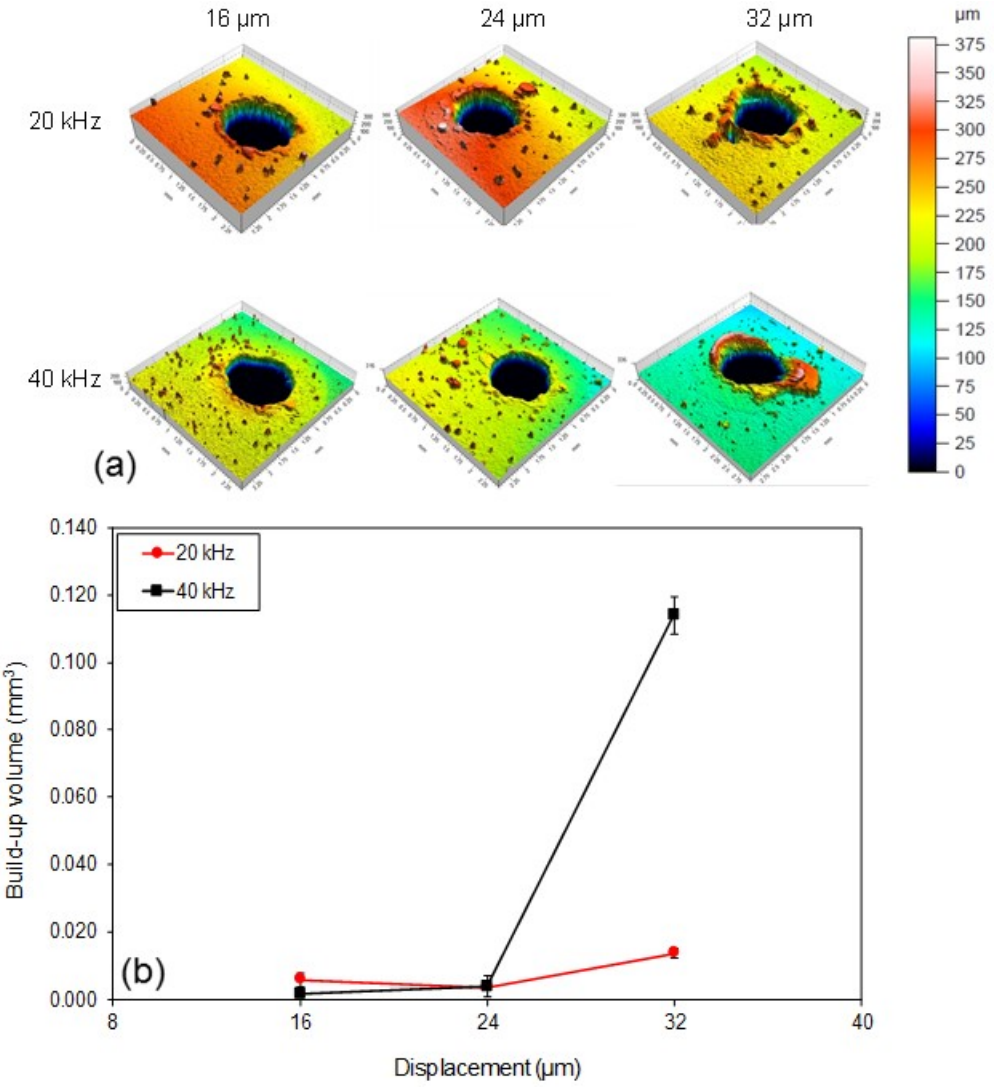

Figure 4.45: (a) Three-dimensional surface profiles, and (b) Variation of volume of build-up material with vibration displacement for frequencies of 20 and 40 kHz during UVLD of AISI 316 steel.

due to incomplete ejection of droplets from deeper melt fronts. Further optimization of both laser processing and ultrasonic vibration parameters is likely to result in further improvements in geometric and quality aspects of the holes drilled using UVLD.

4.3 Ultrasonic vibration-assisted laser atomization

4.3.1 Introduction

Recently, the demand for high quality metal powder has grown rapidly with the development of metal additive manufacturing (AM) technologies [129]. The metal AM technologies are being increasingly adopted for rapid prototyping and series production in diverse industrial sectors. With the established market in powder metallurgy (P/M) and plasma/thermal spraying and the emergence of new applications such as additive manufacturing, the demand for metal powder is projected to grow rapidly in coming years. High-throughput and low-cost production of metal powder with consistent quality and properties for desired applications is a key challenge in the powder manufacturing. Conventional powder preparation techniques such as chemical, mechanical, electrolytic, and atomization (gas, water/oil, vacuum, centrifugal, and ultrasonic capillary wave atomization) processes have been extensively used for the production of metallic powders. Among these techniques, atomization is one of the most versatile techniques for the production of metal powder over a wide range of particle distributions and with high throughput for several metallic materials, including several steels, aluminum alloys, titanium alloys, and superalloys. While average particle size and size distribution of powder particles can be controlled by varying atomization parameters, the atomization processes require high energy to supply water at high pressure (water atomization) or expensive inert gases (gas atomization), resulting in a very low overall energy efficiency ($\sim$3-4%) [130]. The utilization of the water atomization is often restricted as water reacts with the highly reactive metals (titanium and superalloys) and results in formation of undesirable surface oxide layer on powder particles [129]. Also, the conventional atomization processes that take large batch sizes are not very well suited for low volume production of specialized alloy powder for research and development. Metal powder production techniques such

as centrifugal and ultrasonic atomization based on expulsion of molten material/melt film have also been investigated especially for low melting materials [131]. In centrifugal atomization, a stream of molten material is dispensed on a rotating surface and the centrifugal forces cause expulsion of melt into droplets. On the other hand, in the ultrasonic atomization, capillary waves and/or cavitation forces break up the liquid metal film on the surface of the vibrating surface (ultrasonic horn) causing expulsion of fine droplets [68]. Atomized particle size depends on the thermophysical properties of the liquid metal and ultrasonic vibrations parameters. The ultrasonic atomization yields narrower particle size distribution and spherical particles. Due to rapid cooling rates, the particles produced by these techniques also exhibit very good compositional homogeneity and microstructural refinement. In one of the earliest studies on ultrasonic atomization of the metal melts, Lierke and Griesshammer reported particle size of 43 μm and 39 μm for melts of Sn and Pb, respectively, at the ultrasonic vibration frequency of 20 kHz [132]. While the ultrasonic atomization has been mostly investigated for low melting point alloys such as soldering alloys, the processes are also becoming attractive for high melting point alloys with the development of inert rotating/vibrating surface materials. Recently, pulsed laser ablation in liquid media has been used to produce metallic nanoparticles (up to 5 nm in diameter) [133]. However, the laser ablation process is not suitable for the production of micrometer-sized metal particles. In this paper, a novel ultrasonic vibration-assisted laser atomization process is reported for the production of fine metal powder particles. The process involves continuous wave (CW) CO_2 laser irradiation on a consumable metallic substrate vibrating at an ultrasonic frequency (20 kHz). The laser irradiation of the vibrating surface causes surface melting and subsequent expulsion of the melt into fine droplets. Preliminary results on the particle characteristics are presented and discussed for the ultrasonic vibration-assisted laser atomization of AISI 316 stainless steel.

4.3.2 Material and methods

The schematic of the ultrasonic vibration-assisted laser atomization is presented in Fig.5.44. The set-up consisted of an ultrasonic vibration system with a 13-mm diameter threaded Ti-alloy probe (Sonics & Materials, Inc, Newtown, CT) and a continuous wave CO_2 laser (Ferranti, Manchester, UK). For producing powder of AISI 316 stainless steel, a 3-mm thick steel specimen was screwed on the ultrasonic probe. The surfaces of the steel specimens were polished using 400 grit SiC papers followed by sand blasting to increase laser absorption. The steel specimens were vibrated at the frequency of 20 kHz and ultrasonic power outputs of 20, 30, and 40% corresponding to vertical (longitudinal) vibration displacements of 23, 37 and 51 μm, respectively. The laser beam operating with power output of 950 W and beam diameter of 2.15 mm was scanned at the speed of 30 mm/s on the vibrating surface of the steel specimen. The laser irradiation causes surface melting of the vibrating specimen, resulting in droplet ejection in the form of fine metal powder particles. A co-axial argon shroud gas was used to protect the melt pool. The ultrasonic vibration displacements used in this investigation were the optimized parameters resulting in efficient melt expulsion at the given ultrasonic vibration frequency (20 kHz) and the laser power (950 W). A scanning electron microscope equipped with energy-dispersive x-ray spectroscopy (EDS) was used to characterize the microstructural and compositional features of the atomized powder particles. For cross-sectional microstructure analysis, the powder particles were mounted in polymer resin to prevent surface damage during subsequent polishing. The sample preparation consisted of a series of polishing on SiC papers (grit size up to 1200) and final polishing on cloth using alumina solution (particle size up to 0.3 μm). X-ray powder diffractometer (XRD) operating with Cu Kα (λ= 1.54178 Å) radiation was used for identifying the phases in the atomized steel powder.

4.3.3 Results and discussion

In the proposed ultrasonic vibration-assisted laser atomization, a continuous wave CO_2 laser irradiation causes surface melting of the desired consumable metallic substrate that is vibrating at an ultrasonic frequency (Fig.5.44).

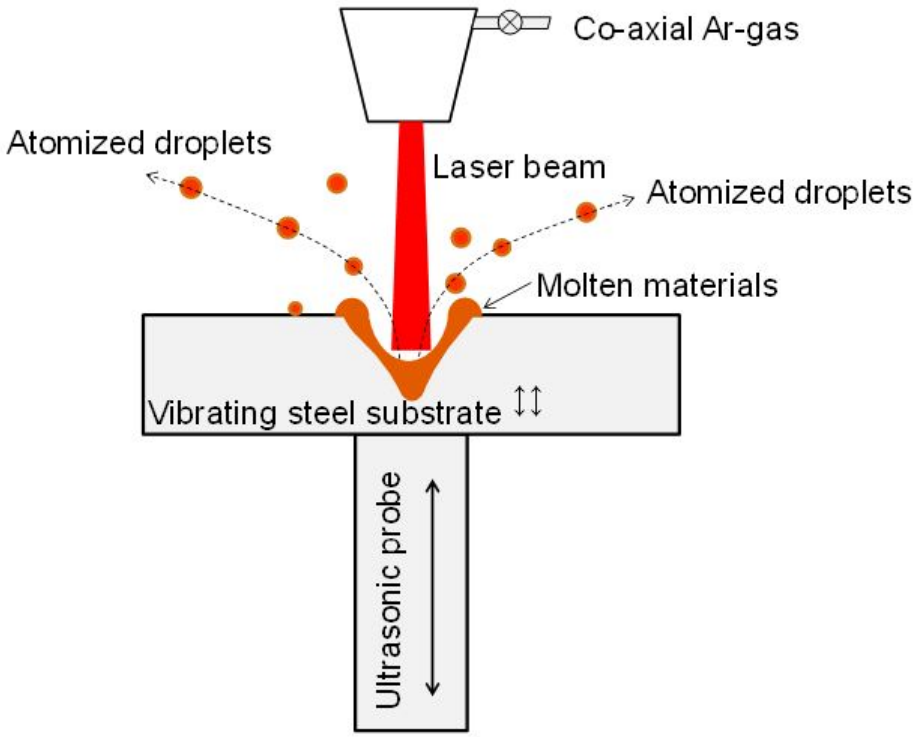

Figure 4.46: Schematic of the ultrasonic vibration-assisted laser atomization setup

While the surface tension effects tend to keep the melt pool in place, the ultrasonic vibrations of the substrate tend to destabilize the melt pool. When the volume of the melt pool reaches a critical size, the ultrasonic vibrations break the surface melt film and causes ejection of the melt into fine droplets. The melt droplets undergo rapid solidification to form solid metal powders. Fig.5.45 shows SEM micrographs of the AISI 316 steel powder particles produced using ultrasonic vibration-assisted laser atomization with laser power of 950 W and vibration displacements of 23, 37, and 51 μm at the ultrasonic frequency of 20 kHz. The metallic powders prepared by ultrasonic vibration-assisted laser atomization have a highly spherical shape. The

high magnification SEM micrographs of the particles show fine dendritic structure on the surface of the particles and interdendritic porosity (Fig.5.45).

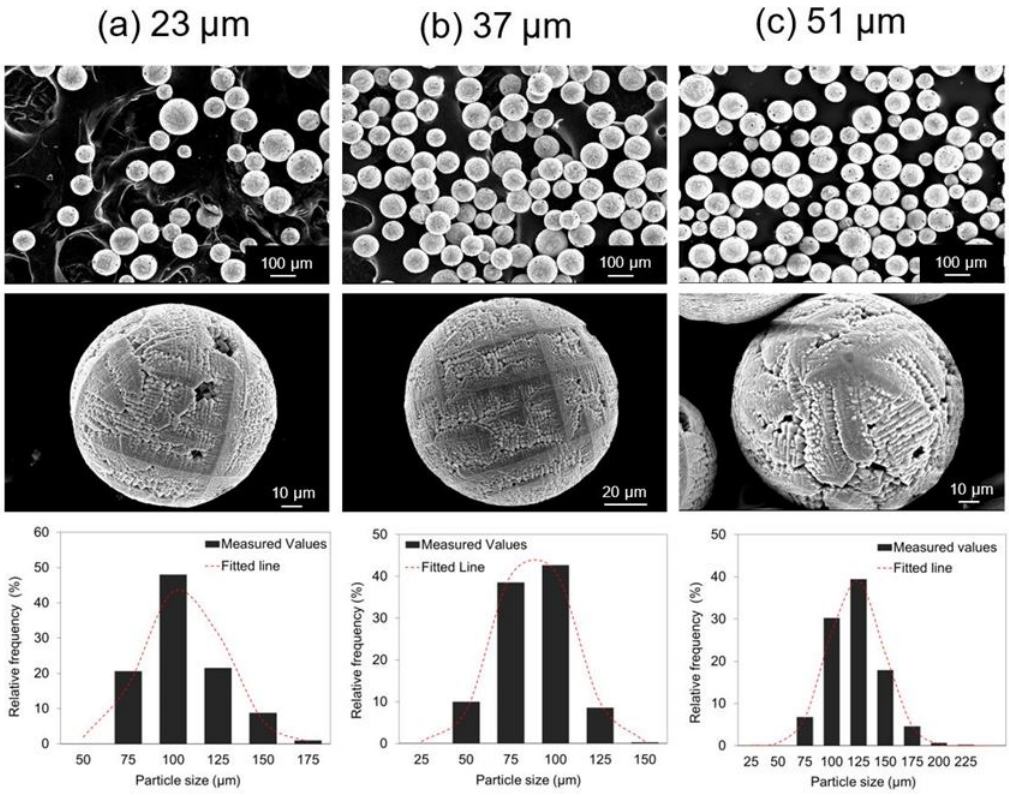

Figure 4.47: SEM micrographs and particle size distribution of steel powder produced by ultrasonic vibration-assisted laser atomization for vibration displacements of (a) 23 μm, (b) 37 μm, and (c) 51 μm.

As it can be seen in Fig.5.45, the particle size distribution peaks at about 100-125 μm for the atomized particles. The average size of the particles were 93$\pm$21 μm, 75$\pm$19 μm, and 84$\pm$24 μm for vibration displacements of 23, 37, and 51 μm, respectively. In general, the intense ultrasonic vibrations with higher displacements resulted in finer atomized particles possibly due to efficient ejection of droplets of smaller volumes. In ultrasonic atomization, several mechanisms such as cavitation wave and capillary wave cause the disintegration of the surface liquid film [134]. In cavitation-wave mechanism, acoustically driven bubble oscillations beneath the liquid surface cause the expulsion of droplets. The cavitation forces can also cause

non-uniform disintegration of the liquid film, ejecting larger chunks of liquid metal. It has been reported that when acoustic cavitation is the main atomization mechanism, irregularity in the shape and size of the atomized droplets is observed [69]. On the other hand, in capillary wave mechanism, the liquid film on the vibrating surface becomes unstable and creates surface capillary wave (ripples) [115]. The amplitude of the capillary wave continuously increases, and eventually the wave peaks break from the liquid film and eject as droplets. Based on Navier-stokes equation, the correlation between wavelength of the capillary waves (λ_s) and atomization parameters is given by [135]

$$\frac{2}{\pi f^2 \lambda_s} \times (4 \times \frac{\sigma \pi^2)}{\rho [\lambda_s]^2} + g) \times tanh(\frac{2\pi l_m}{\lambda_s} + 0.02[\frac{\pi a_0}{\lambda_s} tanh(\frac{2\pi l_m}{\lambda_s}]^{\frac{1}{2}} - 1.04 = 0 \quad (4.9)$$

where g is the acceleration due to gravity (m/s^2), l_m is the film thickness (m), and a_0 is the vibration amplitude (m). It has also been reported that if the liquid film is thin ($tanh(2\pi h/\lambda_s) = 1$) and the impact of gravitational force is negligible compared to the ultrasonic force, Eq. 4.11 reduces to the Lang equation (Eq.4.10)

$$\lambda_s = (\frac{8\pi\sigma}{\rho f^2})^{1/3} \quad (4.10)$$

The capillary wave mechanism results in the formation of highly spherical atomized particles with good correlation between average particle size and wavelength of capillary waves. It has been reported that the average diameter of the ejected droplets (D) during ultrasonic atomization is about 0.34 times of the wavelength of the capillary wave (λ_s) on the liquid film and is given by: [115].

$$D = 0.34 \times \left(\frac{8\pi\sigma}{\rho f^2}\right)^{1/3} \quad (4.11)$$

In the proposed ultrasonic vibration-assisted laser atomization, highly spherical particles were formed indicating presence of capillary wave mechanism for atomization. Assuming capillary wave hypothesis for the proposed ultrasonic-vibration assisted atomization, the capillary wave wavelength and theoretical size of the atomized particles

can be estimated using above equations. The Eq. 4.9 requires the estimation of liquid film thickness to calculate the capillary wave wavelength. In the ultrasonic-vibration assisted laser processing with the similar processing parameters, the melt film thickness of 24 μm was observed from the thermal analysis of laser-material interaction before the expulsion of droplets [126]. Using surface tension (1.77 J/m^2) [128] and density (ρ: 6950 kg/m^3) [82] values at the melting point (Tm: 1750 K) [82] of AISI 316 stainless steel and ultrasonic frequency of 20 kHz, the particle diameter calculated using Eqs. 4.9 and 4.11 is about 72 μm for all three vibration displacements (23, 37, and 51 μm). While the experimental results showed slight reduction in average particle size with increasing vibration displacement, the calculated atomized particle size is not significantly affected by the ultrasonic vibration displacement consistent with the simplified Eq. 4.10. Fig.4.46 compares the measured average diameter of the particles and the calculated particle size. For all vibration displacements, it can be seen that observed particle size is slightly larger than the size calculated based on capillary wave hypothesis.

In contrast to conventional ultrasonic atomization, the laser melting of the material establishes a temperature gradient in the melt film and the surface temperature of the melt film is often much higher than the melting point of the material [79]. The observed larger size of the particles is likely due to the higher melt film temperature. In fact, Eq. 3 predicts larger particle size with higher surface tension and lower density, a result of higher surface temperature. It should also be noted that the thickness of melt film in conventional ultrasonic atomization is relatively uniform. Due to the Gaussian energy distribution in beam and the nature of heat transfer during laser irradiation of a material, the melt pool generally takes the shape of a semi-ellipsoid i.e. the film thickness is maximum at the center of the pool. This is likely to result in non-uniform capillary wavelength on the surface, resulting in wider distribution of particle size as observed in this investigation. Nevertheless, capillary wave hy-

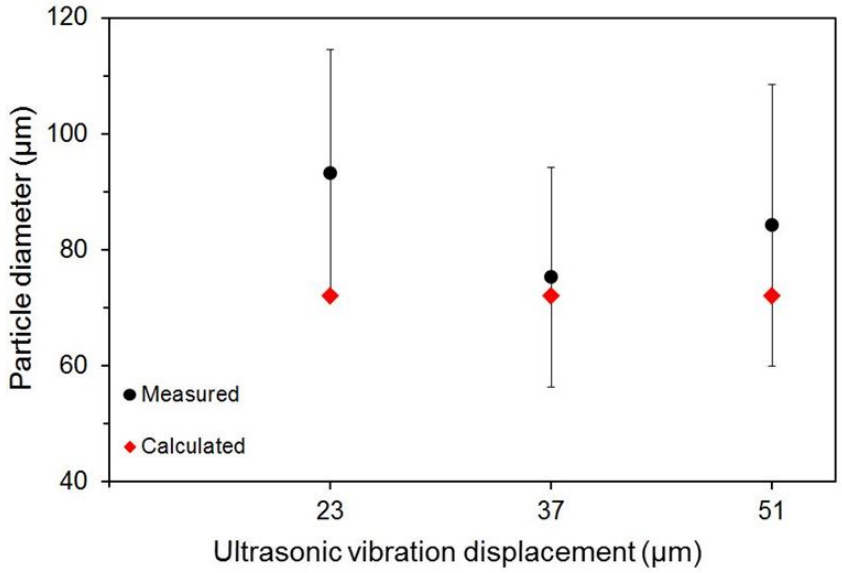

Figure 4.48: Experimental and calculated particle size based on capillary wave hypothesis for ultrasonic vibration-assisted laser atomization of steel for different vibration displacements.

pothesis with material properties (density and surface tension) at melting point gives good estimation of the particle size for the proposed ultrasonic-vibration assisted laser atomization. The development of a fully predictive model for the proposed laser atomization would need careful analysis of laser-material interactions under the influence of ultrasonic vibrations including temperature fields, melt profiles, physical properties of material at observed temperatures, non-uniformity of the melt film thickness, and melt expulsion characteristics. In the capillary wave atomization, the most important parameter that has an effect on the particle size is the vibration frequency. The above equations predict finer average particle size for higher ultrasonic vibration frequency. For example, the calculated average particle size is 49 and 39 μm for the vibration frequencies of 40 and 60 kHz, respectively.

The cross-sectional microstructures of particles produced using proposed ultrasonic vibration-assisted atomization with vibration displacement of 51 μm are presented in Fig.5.47. The finer particles (particle size$<$50 μm) showed relatively uniform

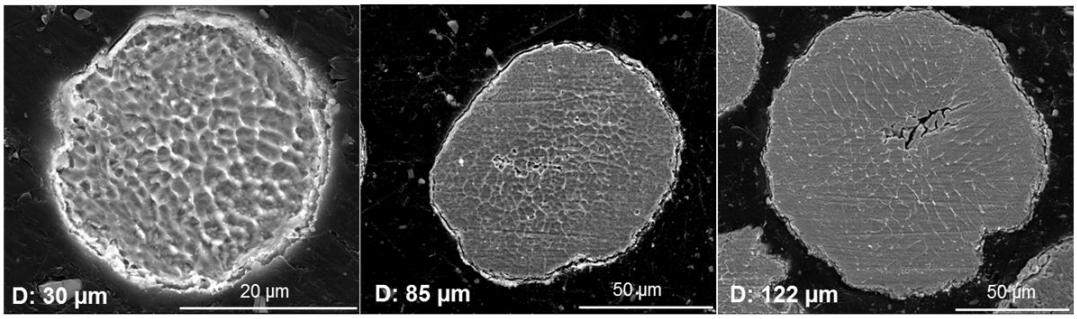

Figure 4.49: Microstructure in cross-section of powder particles of different diameters produced by ultrasonic vibration-assisted laser atomization with vibration displacements of 51 μm.

fine dendritic structure in the microstructure. The grain structure in larger particles showed distinct transitions. The larger particles (particle size>50 μm) showed relatively featureless structure at the outer surface, elongated dendritic structure in the intermediate region, and equiaxed dendritic structure near the center of the particles. The larger particles also exhibited solidification shrinkage at the center of the particles. Similar microstructural observations were made for the powder particles of comparable sizes produced with other vibration displacements (23 and 37 μm). The heat flow during solidification of atomized droplets is controlled by surface convection and radiation while the heat flow inside the droplets occurs by conduction [136]. Most of the analysis of the solidification of the droplet produced by conventional atomization techniques considers nucleation at the center of the particle and microstructure grows radially outward [137]. The liquid metal at the surface feeds for the solidification shrinkage towards the end of solidification [138]. In the proposed ultrasonic vibration-assisted atomization, well defined dendritic structure at the surface of the particles (Fig.5.45) and microstructural transitions leading to solidification shrinkage at the center of the particles indicate that surface of the particles solidify first due to surface nucleation events or rapid growth of surface dendrites [139]. In the proposed atomization, co-axial inert shroud gas was blown on the surface of laser irradiated

material to protect the melt pool. However, the melt droplets from the laser melted pool are ejected outside the cover of shroud gas, leading to surface oxidation. In fact, x-ray diffraction and EDS analysis on the surface and cross section of the particles indicated surface oxidation (Fig.5.48). Such surface oxidation is likely responsible for the observed microstructure evolution in the proposed atomization. It has been well recognized that surface oxides can act as nucleation sites for solidification of atomized droplets [140]. Surface oxidation can be minimized by performing the atomization experiments in the chamber filled with inert gas instead of using co-axial inert shroud gas.

One of the important considerations in the selection of atomization is the cost of the process, which depends on several factors including raw materials, process consumables, throughput, and yield. In the proposed ultrasonic vibration-assisted laser atomization, rate of laser melting and expulsion determines the volume of the atomized powder. Considering relatively smaller melt pool generated by laser melting, the process appears to be well suited for low volume production of specialized powder for alloy development. Obviously, higher power lasers would result in the formation larger melt pool for melt expulsion, potentially improving the throughput to make the process acceptable for production. Also, the proposed ultrasonic vibration-assisted atomization will have larger initial investment (laser and ultrasonic vibration systems), but could lead to significant saving due low consumption of inert gas as the inert gas will be needed only for providing protective cover and not for actual expulsion of melt as in conventional gas atomization.

4.3.4 Conclusions

Production of AISI 316 stainless steel powder from consumable substrate is successfully demonstrated using novel ultrasonic vibration-assisted laser atomization. The atomization is a direct result of surface melting and expulsion of droplets under the

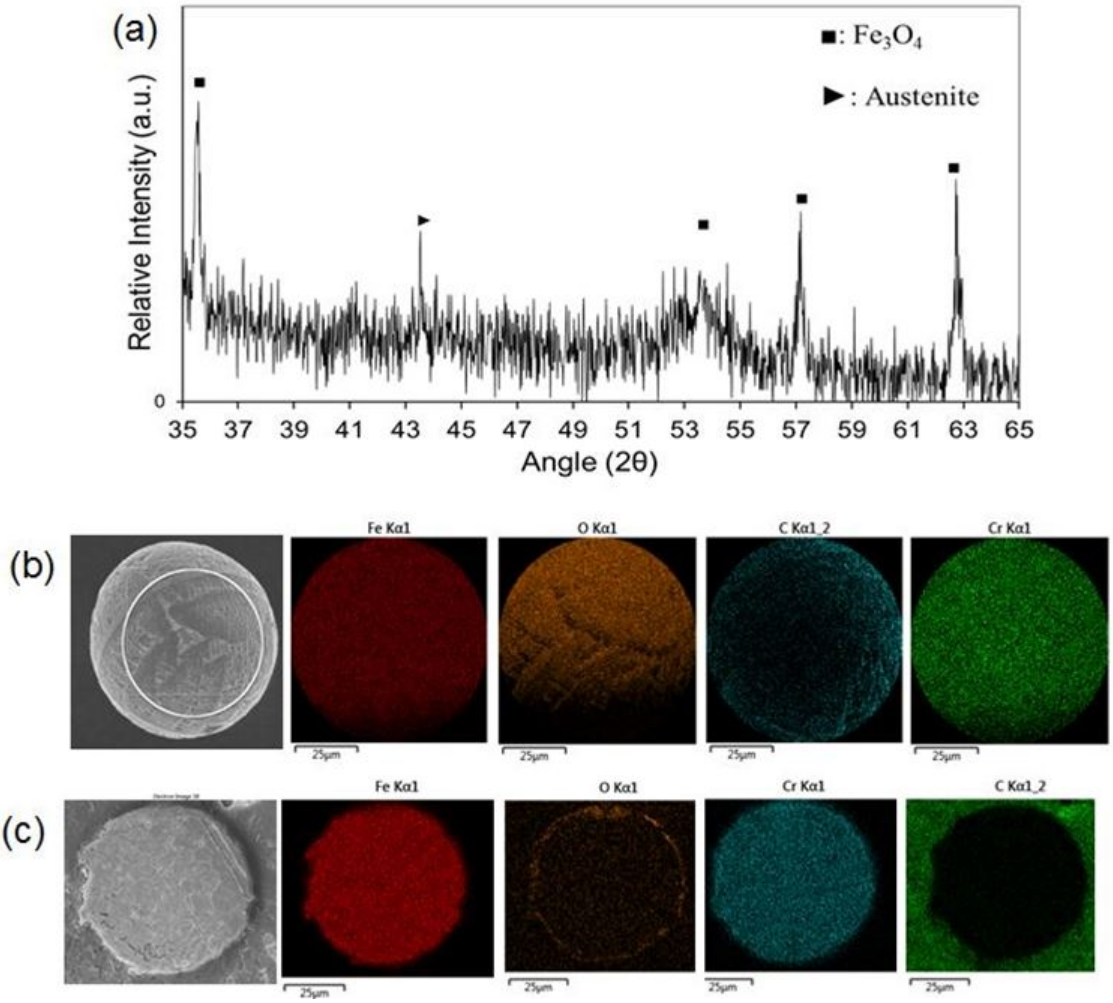

Figure 4.50: (a) X-ray diffraction pattern; (b-c) EDS elemental mapping on surface and cross section, respectively, of powder particles produced by ultrasonic vibration-assisted laser atomization of steel.

simultaneous influence of ultrasonic vibrations and irradiation of laser on the steel substrate. The atomized steel particles were highly spherical with average particle diameter of about 75-95 μm. The average particle diameter and particle size distribution were not significantly influenced by varying vibration displacements, indicating presence of capillary wave-like mechanism of atomization. The microstructure in the cross-section of the larger (particle size>50 μm) solidified particles showed relatively featureless structure near the outer surface, fine dendritic structure at the intermediate region, and shrinkage porosity at the center of particles, indicating that rapid solidification occurs with multiple nucleation at the surface. The proposed ultrasonic vibration-assisted atomization offers an attractive approach of producing metal powder of desired consumable metallic substrate especially for small volume production.

4.4 Ultrasonic vibration-assisted laser surface physical texturing

4.4.1 Introduction

Laser irradiation of the materials can potentially result in various interaction types such as heating, melting, evaporation, and ionization of the matter depending on the intensity of the beam. Laser melting is considered as one the most practical laser processing technique used for microstructural refinement, surface alloying, composite surfacing, and surface modification [9]. Laser texturing as one of the laser surface modification applications, offers interesting surface properties such as enhancement of tribological performance [141–143], hydrophobic surface fabrication [144], coating adhesion improvement [145], biomaterial surface preparation [146, 147], and electrochemical improvement of the materials [148]. Laser surface modification has also been used to tailor the hardness and surface dependent properties such as corrosion and biocompatibility of the metallic materials [3, 149]. In addition to the adjusting the surface chemistry, laser texturing can also tailor the surface topography and affect the surface properties such as biocompatibility of the treated sample [150, 151]. It has been reported that, in pulsed laser texturing, material removal by evaporation (ablation) and surface melting are main mechanisms for micro and nano-scale texture fabrication [151, 152]. In the latter case (surface melting), surface tension displaces/deforms the surface melt pool (Marangoni effect), resulting in controlled texture on the surface of the material. In a recent study, Pfleging *et al.* [151] employed an ArF excimer laser with 5 nm pulse duration and 200 Hz frequency to refine the microstructure and increase the wettability of the Ti6Al4V alloy. They reported that laser surface texturing has marginally decreased the contact angle resulting in higher wettability of the textured surface. In another study, Luo *et al.* [144] prepared the micro-patterned surface on the steel substrate by using an excimer laser with 5-6 ns pulse duration and 150 Hz frequency. They reported that on the surface of pat-

terned steel the water contact angle could reach up to 130∘ that is an improvement on the hydrophobicity of the steel. In this regard, it is worth mentioning, although extensive research investigations have been conducted to optimize the pulsed laser texturing on the different substrate, few studies have used continuous wave lasers (cw) as the heat source. For example, Dong *et al.* [152] used a cw CO_2 laser (2000 W) to melt the surface of the Cu target followed by a pulsed Nd:YAG laser (30 ns pulse duration and 3000 Hz frequency) to fabricated the microtexturing. In recent studies [79, 80, 101, 126], high intensity ultrasonic vibrations were simultaneously applied during the cw-CO_2 laser irradiation. It was observed that application of the high intensity ultrasonic vibrations has two main effects. Firstly, ultrasonic vibrations facilitated the melt expulsion resulting in crater/hole formation on the surface. Secondly, ultrasonic vibrations refined the microstructure at the resolidifed layer in the wall of the drilled holes. In this letter, ultrasonic vibration-assisted continuous wave CO_2 laser surface texturing of stainless steel is presented. The laser beam was irradiated on the surface of the specimens in the melting regime, while low-intensity ultrasonic vibrations (5 and 6.3 μm) with a frequency of 20 kHz were used to prevent the expulsion of the melt and fabricate the laser melted area with enhanced roughness. Preliminary results on the influence of the ultrasonic vibrations on surface roughness, microhardness, phases and corrosion resistance in NaCl solution for ultrasonic vibration-assisted laser textured of stainless steel specimens are presented.

4.4.2 Materials and Methods

The ultrasonic vibration-assisted laser surface patterning setup consisted of a 950 W, continuous wave (cw) CO_2 laser (Ferranti, Manchester, UK) and a 750 W ultrasonic generator (Sonics & Materials, Inc, Newtown, CT) vibrating at 20 kHz frequency. The distance between the laser head and surface of the specimens was 10 mm. The direction of the vibrations was aligned with the laser beam and perpendicular to the surface

of the specimens. Experiments were conducted on 4 mm thick AISI 316 stainless steel specimens (17.45% Cr, 11.81% Ni, 2.5% Mo, 0.05% C, 1.35% Mn, 0.68% Si, 0.011% S, 0.047% P, and balance Fe by weight). Specimens were polished using SiC paper up to 600 mesh size to remove any surface oxide layer followed by sandblasting to enhance their laser absorption coefficient. Specimens were ultrasonically cleaned, before and after processing, in acetone, alcohol, and DI water. Specimens were threaded on the tip of the titanium alloy ultrasonic probe of 25.4 mm diameter, and laser irradiation and ultrasonic vibration were simultaneously applied to the specimens. The laser irradiation speed and ultrasonic power outputs used in this investigation were the optimum parameters that resulted in the laser-material interaction without significant expulsion of the molten material. In this experiments, ultrasonic vibration power outputs were chosen 20% (specimen B1), and 25% (specimen B2). For comparison, one specimen was laser surface melted (LSM) without application of the ultrasonic vibrations (specimen B3) and one specimen was only sandblasted (specimen B4). The corresponding amplitude of 20% and 25 % ultrasonic vibration power output were 5 μm and 6.3 μm, respectively. The surface roughness of the specimens after the ultrasonic vibration-assisted laser patterning were scanned using a three-dimensional surface profilometer (Nanovea, Irvine, CA). A scanning electron microscope was used (JEOL Ltd, Tokyo, Japan) to characterize the surface and cross-sectional features of the specimens. For the cross-sectional SEM imaging, specimens were polished using SiC paper (up to 1200 mesh size) followed by alumina solution mirror polishing. The polished surface of the specimens etched for 10 s using a common etchant for 300 series stainless steels (Carpenters stainless steel etch; 6 mL HNO3, 122 mL HCl, 122 mL Ethanol, 8.5 g FeCl3, and 2.4 g CuCl2). The phase identification of the laser-processed specimens was performed using an x-ray diffractometer (BRUKER AXS, Inc., Madison, WI) operating with Cu K radiation. The diffraction angle (2θ) was varied between 40 and 80 $\circ$. Electrochemical corrosion tests were performed us-

ing a VERSAstat 4 potentiodynamic (AMETEK, Inc., Berwyn, PA). Samples were used as working electrode submerged in 3.5% wt NaCl solution. Counter and reference electrodes were Pt and Ag/AgCl (3 mol.), respectively. Specimens were kept in the solution for 3600 s for potential stabilization before the test. The area of the specimens exposed to the electrolyte during the electrochemical test was 1 cm^2 and specimen potential was raised with 0.5 mV/s rate.

4.4.3 Results and discussion

Fig.5.49 a shows the three-dimensional (3D) surface profile of the sand blasted (specimen B4), laser surface melted (specimen B3) and ultrasonic vibration-assisted laser surface textured specimens with ultrasonic power outputs of 20% (specimen B1) and 25% (specimen B2). It can be seen that the surface profile of specimen B4 consists of very close short peaks formed during the sandblasting. It is worth mentioning that formation of the aforementioned dentate surface decreases the reflectivity of the shiny metallic surface and subsequently increases the absorption of the irradiated laser beam [153].

Laser irradiation melts the surface of the specimen and removes the serrated profile resulting in formation of a very smooth surface profile in specimen B3 (Fig.5.49 a). However, application of the ultrasonic vibrations during the laser surface melting (specimens B1 and B2) significantly reforms the surface profile of the specimens. It appears that ultrasonic vibrations disturb the surface molten layer and result in the development of rugged surface. Using a three-dimensional (3D) profilometery, surface height profile of each specimen were extracted in a direction parallel to the laser melted tracks and plotted in Fig.5.49 b-c exhibits the arithmetic average of the absolute values of the profile height (Ra) for specimens B1, B2, B3 and B4 parallel to the direction to the laser melted tracks. Specimen B4 has only undergone the sand blasting, shows the surface roughness value of Ra=1.81 μm $\pm$ 0.05 μm.

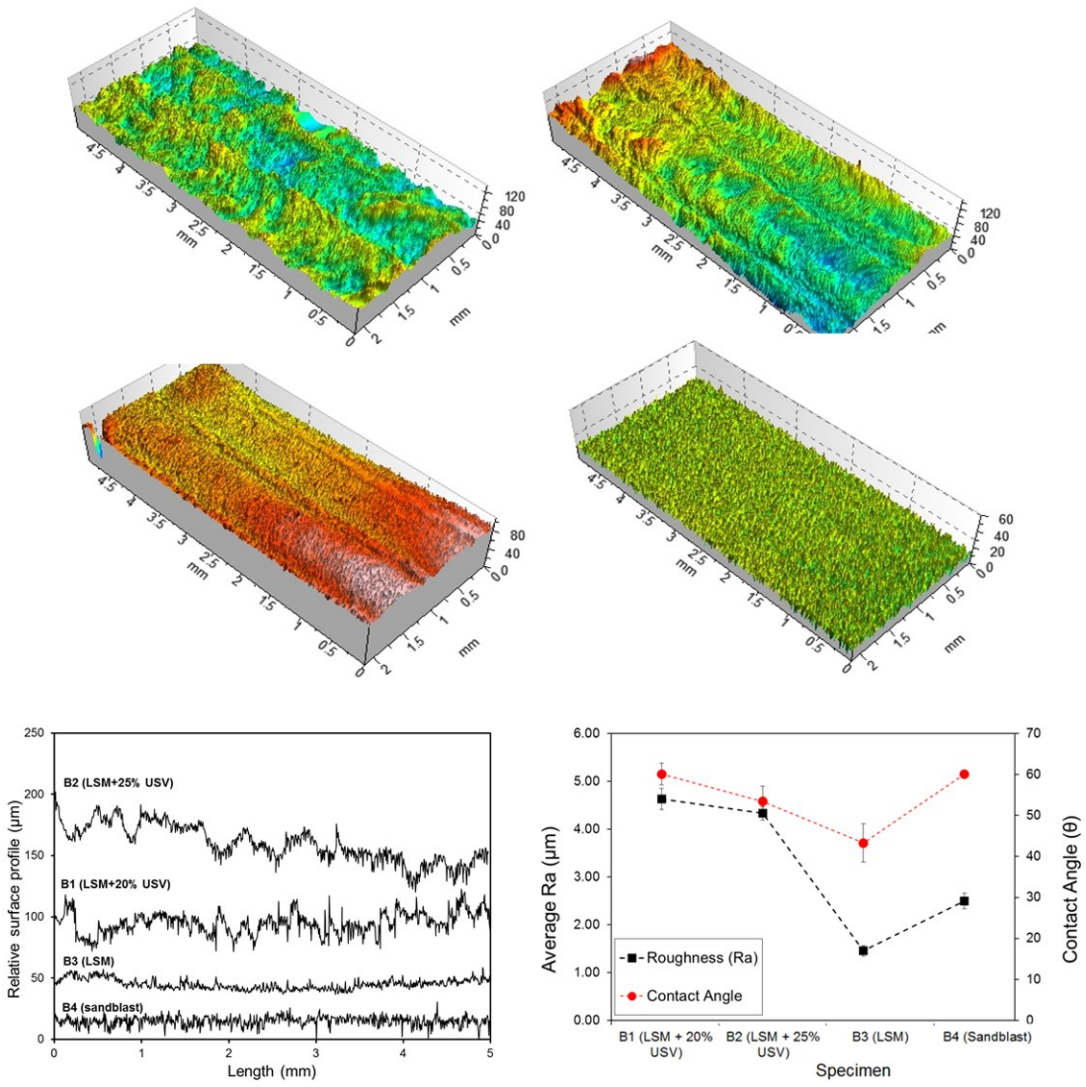

Figure 4.51: (a) Two dimensional surface profile and (b) average roughness values (Ra) for sand blasted, laser melted with and without simultaneous application of ultrasonic vibrations specimens parallel and perpendicular to the laser tracks

However, laser surface irradiation without application of the ultrasonic vibrations (specimen B3) re-melts the surface resulting in very smooth surface with surface roughness of Ra(=0.28 μm $\pm$ 0.06 μm. In contrast, simultaneous application of the ultrasonic vibrations, significantly increases the average roughness values to Ra=1.7 μm $\pm$ 0.06 for specimen B1 and Ra=3.1 μm $\pm$ 0.24 μm for specimen B2. Surface and cross-sectional SEM micrographs of the specimens laser melted with and without simultaneous application of ultrasonic vibrations are presented in Fig.5.50 a-b. Top surface SEM micrographs clearly show the laser melted tracks along with unmelted substrate. The corresponding cross-sectional SEM micrographs show formation of a well-defined resolidified semi-spherical melt pool in the steel specimens. It can be seen that when ultrasonic vibration is not applied (specimen B3), there is a small unmelted region ($\sim$100 μm) between laser melted tracks. However, when ultrasonic vibration with 20% of the power output (specimen B1) is simultaneously applied during the laser melting, the unmelted region between laser tracks decreases in the initial tracks and eventually eliminates. It is worth mentioning that the overall temperature of the substrate increases as the laser surface melting proceeds, which leads to accumulation of the heat. In other words, conduction heat loss plays a critical role in the initial stage of the laser surface melting resulting in formation of the unmelted region. However, after the accumulation of the heat (higher temperature of the substrate), the unmelted region is diminished and eventually leads to overlapping the laser melted track. It has also been reported that the conductivity of the steel is increased under the influence of the ultrasonic vibrations [56]. This phenomenon can also accelerate the heat conduction in the laser irradiated specimen and facilitate the reduction of the unmelted region. The average overlap between laser melted tracks in specimen B1 is 8.8% $\pm$ 4%. Likewise, overlap increases to 23.4% $\pm$ 3% by raising the power output to 25 % (specimen B2). The variation of the melt pool width and depth for specimens B1, B2, and B3 are measured from SEM micrographs and plotted in

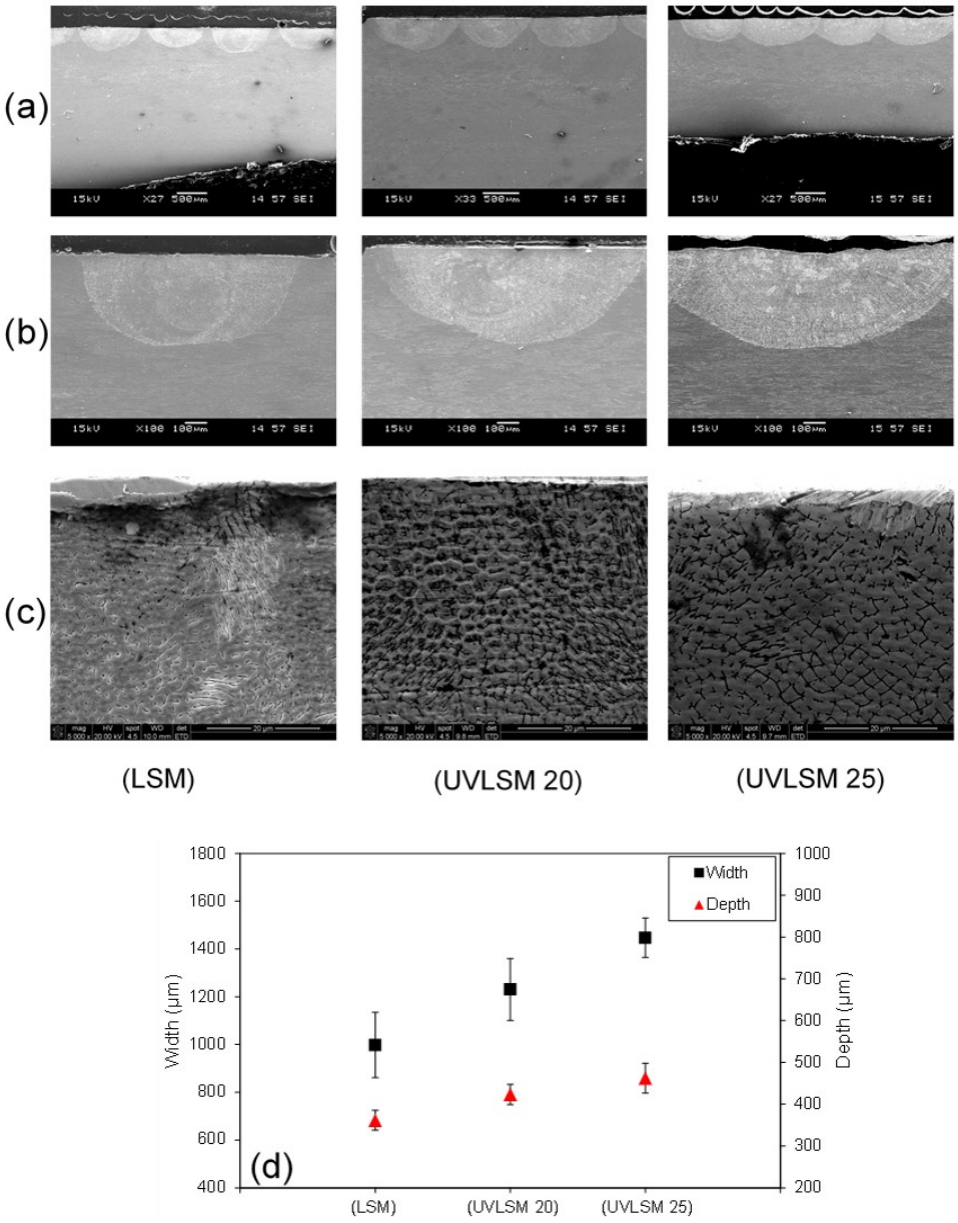

Figure 4.52: (a) Surface and (b, c) cross-sectional SEM micrographs and (d) variation of the melt pool width and depth for specimens laser melted with and without simultaneous application of ultrasonic vibrations

Fig.5.50 d. For specimen B3, width and depth of the melt pool were 998 μm 82 μm and 361 μm $\pm$ 36 μm, respectively. However, for specimen B1 (similar laser irradiation condition and 20% ultrasonic vibration power output), the width and depth of the melt pool significantly increased to 1230 μm $\pm$ 130 μm and 423 μm $\pm$ 24 μm, respectively. In addition, increasing the ultrasonic power output to 25% (specimen B2) further increased the width and depth of the melt pool to 1447 μm $\pm$ 136 μm and 462 μm $\pm$ 24 μm, respectively. It is worth mentioning that, it is claimed that some thermophysical properties of the metallic specimen are influenced ultrasonic vibrations. For example, as mentioned earlier, ultrasonic vibrations enhance both thermal conductivity (k) [56] and convection coefficient (h) [57]. Enhancement of the k, lowers the temperature of the laser incident area while pass more heat to the adjunct non-irradiated area causing temperature increase. On the other hand, enhancement of the h leads to higher convection heat loss decreasing the temperature of the laser-incident and non-irradiated area. Hence, in the case of ultrasonic vibration-assisted laser processing, thermal conduction and convection coefficient have a competitive influence on temperature distribution and accordingly melt pool geometry. The surface XRD patterns of the specimen B1, B2, B3, and B4 are presented in Fig.5.51 a. XRD spectra of specimen B4 consists of dominant characteristic γ-austenite phase (fcc) and low-intensity $\alpha^{'}$-martensite peaks (bcc). It has been reported [154,155] that sandblasting, as a source of severe deformation can facilitate $\lambda \rightarrow \alpha$ phase transformation and results in formation of the strain-induced martensite at the surface of the stainless steel 316 specimen. On the other hand, specimens were commercially available stainless steel 316 bolts, which are commonly fabricated by cold forming process. Hence, the entire specimen has confronted a severe plastic deformation, which further induces martensite formation. This is in a good agreement with the microhardness results presented in Fig.5.51 b in which the specimen B4 shows significantly higher microhardness in all the depths. In other words, the stress-induces martensite exists

at the surface and the bulk. XRD pattern of specimen B3, which has undergone laser surface melting without ultrasonic vibrations, reveals elimination of the -martensite phase.

It has been reported that annealing process (even at a lower temperature than static recrystallization) can revert stress-induced martensite to the austenite phase [156]. Moreover, it can be seen that laser surface melting, with and without application of ultrasonic vibrations, facilitated growing of the austenite phase in the 200 and 220 planes. It is worth mentioning that austenite phases at 200 and 220 planes were also detected in the sandblasted specimen, however, remelting the surface of the stainless steel has significantly increased the intensity of the detected peaks. Mudali and Dayal [62] also reported that laser surface melting of the AISI 316 stainless steel remarkably increased the relative intensity of the $\lambda(200)$ and $\lambda(220)$ peaks. Potentiodynamic polarization curves of the specimen B1-B4 are plotted in Fig.5.52 a. Anodic region of the potentiodynamic curve of the specimen B4 consists of two distinct parts. In the first part, from -212 mV to 300 mV, anodic current is gradually increased by increasing the applied potential. That phenomenon is due to formation of the characteristic protective passive layer at the surface of the stainless steel that limits the anodic dissolution of the stainless steel [157]. In contrast, in the second part of the anodic curve (from 300 to 650 mV), the anodic current increases dramatically with increasing the employed potential. Superior anodic dissolution (or current) in the second part is due to the localized damage/breakdown of the protective passive layer and is commonly identified as pitting corrosion. Chloride (Cl^-) ions attack the thin protective passive layer at the surface of the stainless steel especially at heterogeneities such as grain boundaries, inclusions, and second phase precipitates [158]. Potentiodynamic curves of the laser surface melted (specimen B3) and ultrasonic vibration-assisted laser surface textured specimens with ultrasonic power outputs of 20% (specimen B1) and 25 % (specimen B2) show elimination of the pitting cor-

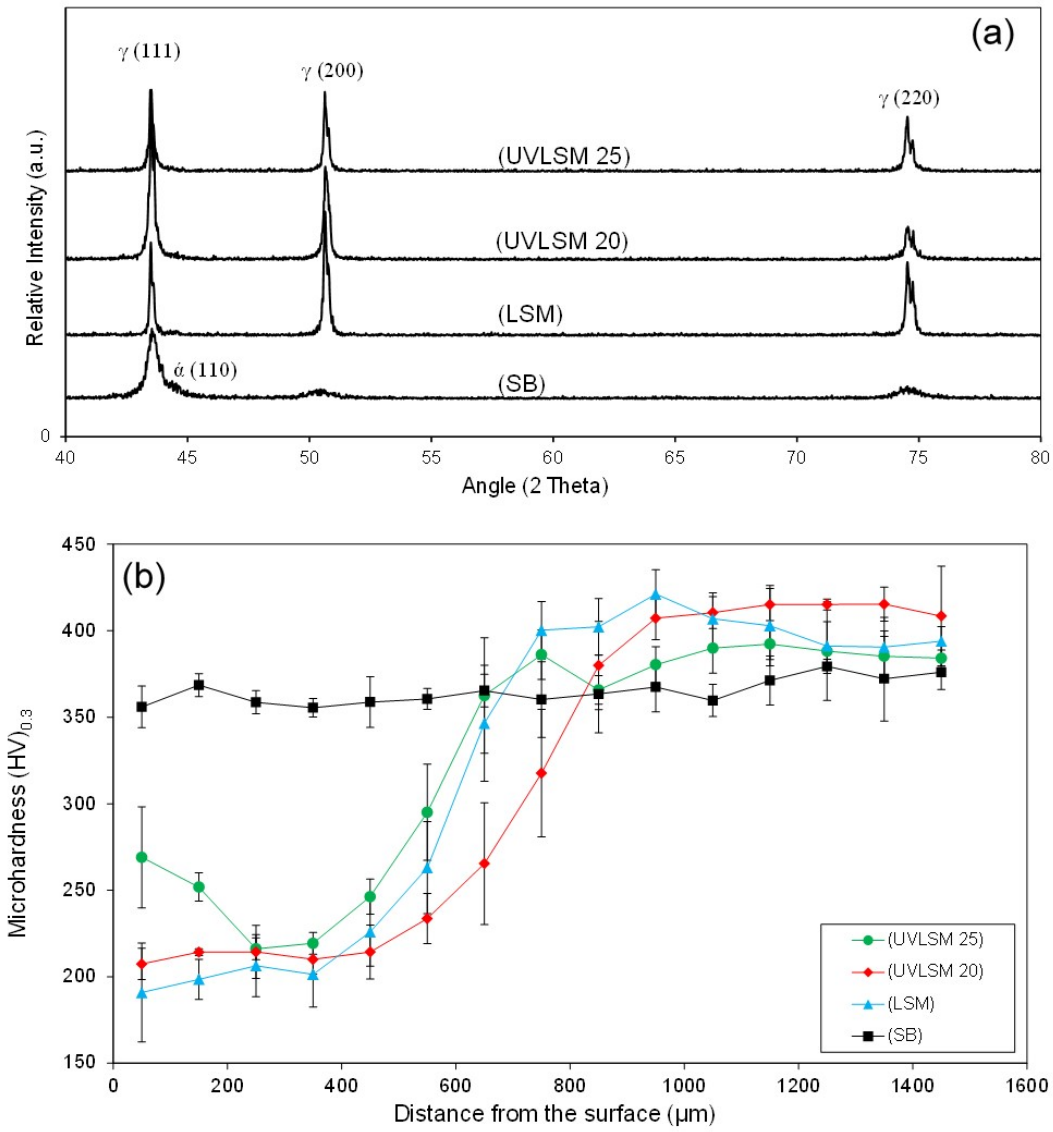

Figure 4.53: (a) Surface XRD patterns and (b) variation of the microhardness along the depth for sand blasted, laser melted with and without simultaneous application of ultrasonic vibrations

rosion. Kwok *et al.* [159] claimed that removal or redistribution of the manganese sulfide inclusions during the laser surface melting led to the improvement of the pitting corrosion resistance in stainless steel. Corrosion potential, corrosion current and corrosion rate of the stainless steel specimen were calculated using potentiodynamic curves through Tafel extrapolation method and the corresponding values are plotted in Fig.5.52 b. Laser irradiated specimen, with and without application of the ultrasonic vibrations, possessing lower corrosion current and potential than sand-blasted specimen, resulting in significantly lower corrosion rates. Homogenization of the microstructure at the melted region is reported to be a cause for corrosion resistance enhancement in laser melted stainless steel specimens. The XRD spectra of sand blasted specimen consisted of dual phases of α' martensite and λ-austenite that showed lower corrosion resistance (higher corrosion rate). However, in laser irradiated specimens in which the α' martensite was eliminated and single gamma phase was detected in the microstructure resulting in lower corrosion rate.

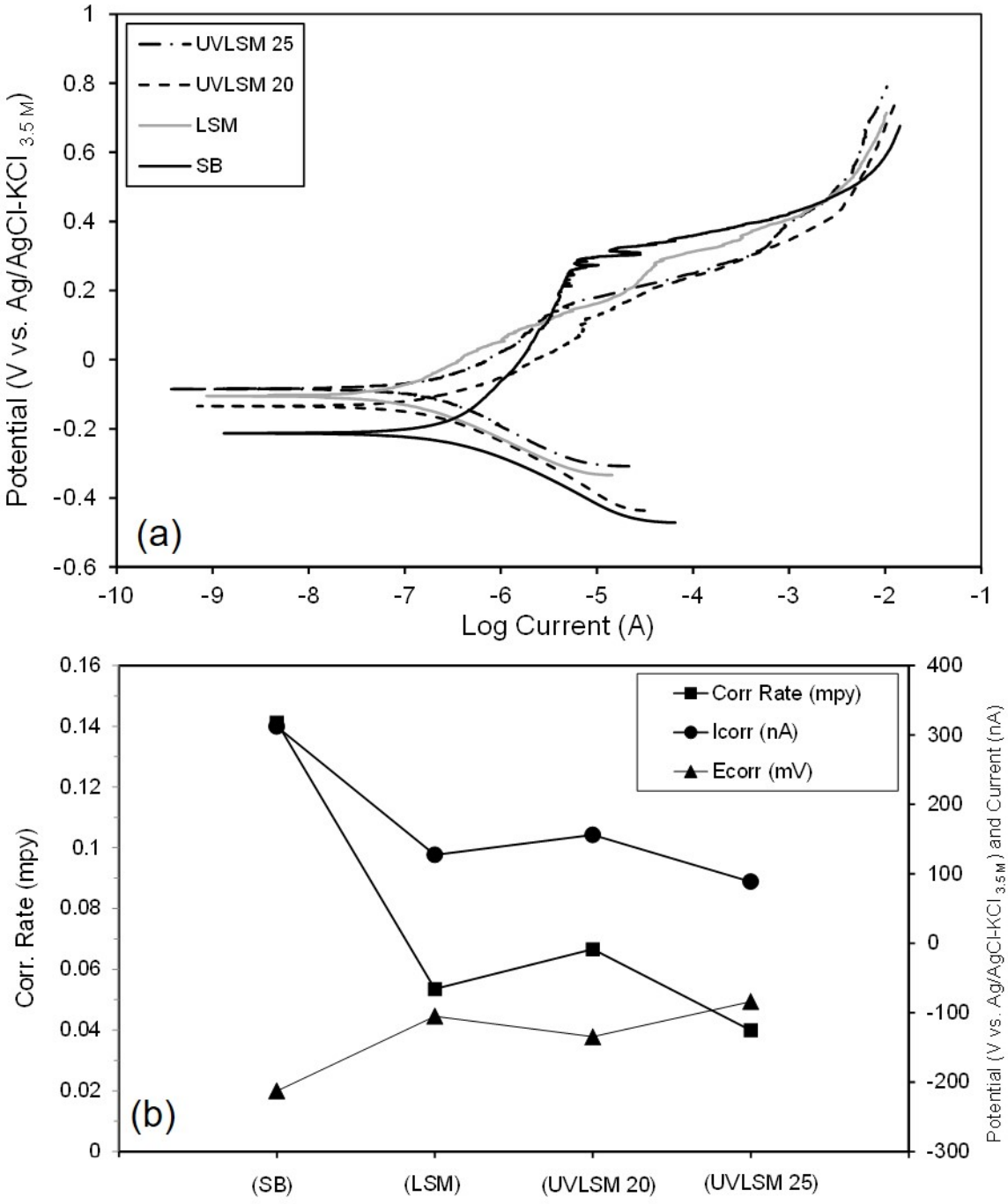

Figure 4.54: (a) Potentiodynamic polarization curves and (b) corrosion test outputs for sand blasted, laser melted with and without simultaneous application of ultrasonic vibrations

CHAPTER 5

FUTURE WORK

Study 1

Modeling of the molten pool critical volume/size formation before initiation of expulsion by balancing the active forces on the surface of the specimen such as surface tension, ultrasonic vibration pressure, and drag force.

As the laser surface irradiation (without application of the ultrasonic vibrations) of the stainless steel specimen has shown, no expulsion of the molten material occurs during the process. So far, our assumption of the formation of the critical volume/size of the molten pool has originated from the experimental results revealed by high speed camera imaging. The assumption below was used as the foundation of the further finite element modeling and prediction of the hole volume. To develop a model needless to any experimental input, it seems necessary to predict the formation/requirement of the critical volume/size of the molten pool for initiation of the expulsion. For this approach, the dynamic flow of the molten pool (fluid) will be considered. For example, the temperature gradient in the surface (from center of the melt pool to the edges of the laser/material interaction area) can form a surface tension difference and facilitates the radial flow of the molten metal. On the other hand, ultrasonic vibration applies a high amount of force (Maximum acceleration for frequency of 20 kHz and displacement of 23 μm is around 160,000 m/s^2) to the specimen (presented in Fig 5.1). The ultrasonic-induced force will affect the flow of the molten metal similar to recoil pressure (shown in Fig 5.2)

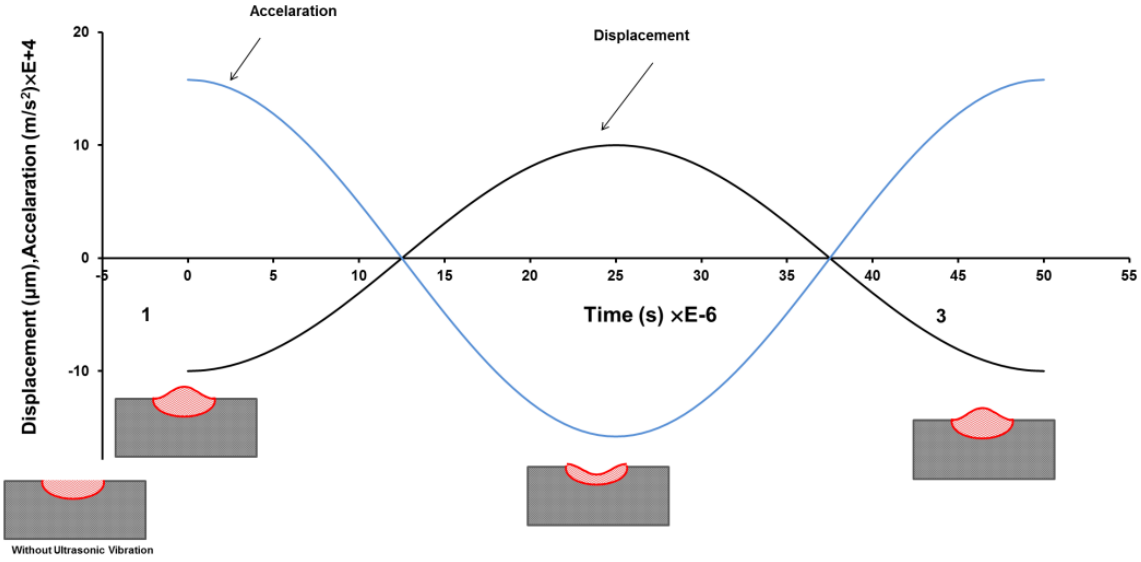

Figure 5.1: Displacement and acceleration of the specimen during one cycle of ultrasonic vibration

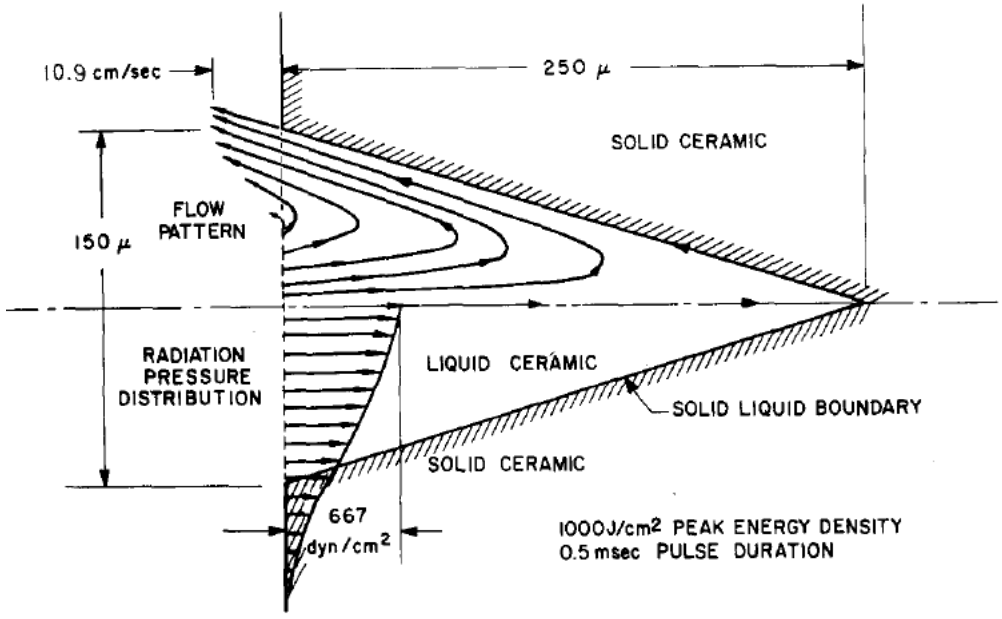

Figure 5.2: Radiation pressure effect on the molten material inside the hole [77]

Study 2

Modeling and prediction of the convection heat transfer coefficient enhanced by 20 kHz frequency and different amplitudes and its impact on surface melting suppression during ultrasonic vibration-assisted laser surface machining

It has been well-reported that application of the ultrasonic vibration results in enhancement of heat transfer, especially solid-fluid convention heat transfer. However, most of studies rely only on experimental data and longer application of the ultrasonic vibration (in the range of minutes). The direct measurement of temperature and calculating the heat transfer coefficient in the short laser irradiation times if is not impossible is complicated. So that, modeling of the air flow and convection enhancement during the process could results in better understanding of the heat transfer phenomena and further melting suppression (as it has been observed in experiments). The preliminary finite element modeling of the specimen displacement and vibration-induced air flow is presented in Fig 5.3

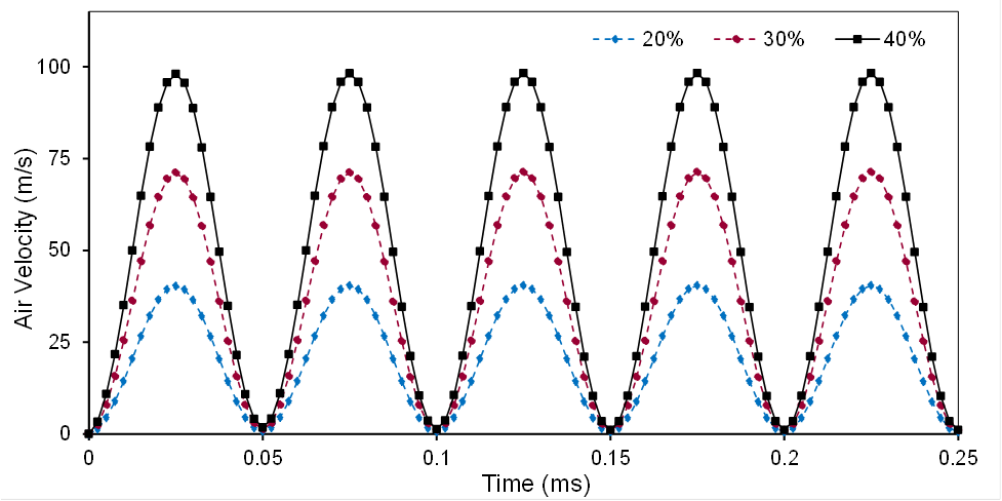

Figure 5.3: Air flow velocity (m/s) at the solid-fluid boundary for ultrasonic outputs of 20, 30, and 40 %

Study 3

Investigate the experimental parameters influence on formation of the recast layer

Formation and expulsion of the molten material film has been proposed as a part of mechanism of the material removal in the ultrasonic vibration-assisted laser surface drilling. However, presence of recast layer in the cross-section SEM micrographs of the holes indicates that part of the molten/heated material remains inside the hole. As it has been mentioned earlier, recast layer is one of the disadvantages of the laser drilling process which affects the quality of the holes. In this study, the effect of ultrasonic vibration frequency (20 and 40 kHz) and different vibration displacements will be investigated to optimize/reduce the formation of the recast layer. XRD and EDS analysis will be performed to determine sensitization of the steel by precipitation of chromium-rich carbides at the grain boundaries and the depletion of chromium in the adjacent regions. Further analysis of the dendrites and their growth direction will determine the influence of the longitudinal ultrasonic vibrations on the fluid (molten steel) flow dynamic. The outcome of the aforementioned analysis will enhance the understanding of the process and strengthen the proposed theoretical mechanism.

BIBLIOGRAPHY

[1] BJ Kooi, YT Pei, and J Th M De Hosson. The evolution of microstructure in a laser clad tib–ti composite coating. *Acta Materialia*, 51(3):831–845, 2003.

[2] Sandip P Harimkar and Narendra B Dahotre. Characterization of microstructure in laser surface modified alumina ceramic. *Materials Characterization*, 59(6):700–707, 2008.

[3] J Dutta Majumdar and I Manna. Laser processing of materials. *Sadhana*, 28(3-4):495–562, 2003.

[4] Karl-Heinz Leitz, Benjamin Redlingshöfer, Yvonne Reg, Andreas Otto, and Michael Schmidt. Metal ablation with short and ultrashort laser pulses. *Physics Procedia*, 12:230–238, 2011.

[5] Robert A Brockman, William R Braisted, Steven E Olson, Richard D Tenaglia, Allan H Clauer, Kristina Langer, and Michael J Shepard. Prediction and characterization of residual stresses from laser shock peening. *International Journal of Fatigue*, 36(1):96–108, 2012.

[6] Dongdong Gu, Yves-Christian Hagedorn, Wilhelm Meiners, Guangbin Meng, Rui João Santos Batista, Konrad Wissenbach, and Reinhart Poprawe. Densification behavior, microstructure evolution, and wear performance of selective laser melting processed commercially pure titanium. *Acta Materialia*, 60(9):3849–3860, 2012.

[7] SP Harimkar, AN Samant, AA Khangar, and Narendra B Dahotre. Prediction of solidification microstructures during laser dressing of alumina-based grinding wheel material. *Journal of Physics D: Applied Physics*, 39(8):1642, 2006.

[8] YT Pei and J Th M De Hosson. Functionally graded materials produced by laser cladding. *Acta materialia*, 48(10):2617–2624, 2000.

[9] Narendra B Dahotre and Sandip Harimkar. *Laser fabrication and machining of materials*. Springer Science & Business Media, 2008.

[10] Evren Yasa, J-P Kruth, and Jan Deckers. Manufacturing by combining selective laser melting and selective laser erosion/laser re-melting. *CIRP Annals-Manufacturing Technology*, 60(1):263–266, 2011.

[11] Hitesh D Vora, Soundarapandian Santhanakrishnan, Sandip P Harimkar, Sandra KS Boetcher, and Narendra B Dahotre. One-dimensional multipulse laser machining of structural alumina: evolution of surface topography. *The International Journal of Advanced Manufacturing Technology*, 68(1-4):69–83, 2013.

[12] CL Chan and J Mazumder. One-dimensional steady-state model for damage by vaporization and liquid expulsion due to laser-material interaction. *Journal of Applied Physics*, 62(11):4579–4586, 1987.

[13] Johan Meijer. Laser beam machining (lbm), state of the art and new opportunities. *Journal of Materials Processing Technology*, 149(1):2–17, 2004.

[14] A Bharatish, HN Narasimha Murthy, B Anand, CD Madhusoodana, GS Praveena, and M Krishna. Characterization of hole circularity and heat affected zone in pulsed co 2 laser drilling of alumina ceramics. *Optics & Laser Technology*, 53:22–32, 2013.

[15] Elijah Kannatey-Asibu Jr. *Principles of laser materials processing*, volume 4. John Wiley & Sons, 2009.

[16] ND Pandey, HS Shan, and A Bharti. Percussion drilling with laser: hole completion criterion. *The International Journal of Advanced Manufacturing Technology*, 28(9-10):863–868, 2006.

[17] A Weck, THR Crawford, DS Wilkinson, HK Haugen, and JS Preston. Laser drilling of high aspect ratio holes in copper with femtosecond, picosecond and nanosecond pulses. *Applied Physics A*, 90(3):537–543, 2008.

[18] Boris N Chichkov, C Momma, Stefan Nolte, F Von Alvensleben, and A Tünnermann. Femtosecond, picosecond and nanosecond laser ablation of solids. *Applied Physics A*, 63(2):109–115, 1996.

[19] G Kamlage, T Bauer, A Ostendorf, and BN Chichkov. Deep drilling of metals by femtosecond laser pulses. *Applied Physics A*, 77(2):307–310, 2003.

[20] X Zhu, DM Villeneuve, A Yu Naumov, S Nikumb, and PB Corkum. Experimental study of drilling sub-10 μm holes in thin metal foils with femtosecond laser pulses. *Applied Surface Science*, 152(3):138–148, 1999.

[21] CY Yeo, SC Tam, S Jana, and Michael WS Lau. A technical review of the laser drilling of aerospace materials. *Journal of Materials Processing Technology*, 42(1):15–49, 1994.

[22] A Corcoran, L Sexton, B Seaman, P Ryan, and G Byrne. The laser drilling of multi-layer aerospace material systems. *Journal of Materials Processing Technology*, 123(1):100–106, 2002.

[23] MM Hanon, E Akman, B Genc Oztoprak, M Gunes, ZA Taha, KI Hajim, E Kacar, O Gundogdu, and A Demir. Experimental and theoretical investiga-

tion of the drilling of alumina ceramic using nd: Yag pulsed laser. *Optics & Laser Technology*, 44(4):913–922, 2012.

[24] WSO Rodden, SS Kudeshia, DP Hand, and JDC Jones. The use of assist gas in the precision laser drilling of titanium. In *Proceedings of the ICALEO*, pages 41–50, 2000.

[25] MRH Knowles, G Rutterford, D Karnakis, and A Ferguson. Micro-machining of metals, ceramics and polymers using nanosecond lasers. *The International Journal of Advanced Manufacturing Technology*, 33(1-2):95–102, 2007.

[26] Wen-Tung Chien and Shiann-Chin Hou. Investigating the recast layer formed during the laser trepan drilling of inconel 718 using the taguchi method. *The International Journal of Advanced Manufacturing Technology*, 33(3-4):308–316, 2007.

[27] HK Sezer, L Li, M Schmidt, AJ Pinkerton, B Anderson, and P Williams. Effect of beam angle on haz, recast and oxide layer characteristics in laser drilling of tbc nickel superalloys. *International Journal of Machine Tools and Manufacture*, 46(15):1972–1982, 2006.

[28] RS Patel and MQ Brewster. Gas-assisted laser-metal drilling-theoretical model. *Journal of thermophysics and heat transfer*, 5(1):32–39, 1991.

[29] RS Patel and MQ Brewster. Gas-assisted laser-metal drilling-experimental results. *Journal of thermophysics and heat transfer*, 5(1):26–31, 1991.

[30] John F Ready. *Industrial applications of lasers*. Academic press, 1997.

[31] DC Hamilton and IR Pashby. Hole drilling studies with a variable pulse length co2 laser. *Optics & Laser Technology*, 11(4):183–188, 1979.

[32] S Bandyopadhyay, JK Sarin Sundar, G Sundararajan, and SV Joshi. Geometrical features and metallurgical characteristics of nd: Yag laser drilled holes in thick in718 and ti–6al–4v sheets. *Journal of Materials Processing Technology*, 127(1):83–95, 2002.

[33] DKY Low, L Li, and PJ Byrd. Hydrodynamic physical modeling of laser drilling. *Journal of manufacturing science and engineering*, 124(4):852–862, 2002.

[34] X Chen, WT Lotshaw, AL Ortiz, PR Staver, CE Erikson, MH McLaughlin, and TJ Rockstroh. Laser drilling of advanced materials: effects of peak power, pulse format, and wavelength. *Journal of laser applications*, 8(5):233–239, 1996.

[35] DKY Low, L Li, and AG Corfe. Effects of assist gas on the physical characteristics of spatter during laser percussion drilling of nimonic 263 alloy. *Applied surface science*, 154:689–695, 2000.

[36] DKY Low, L Li, and PJ Byrd. The influence of temporal pulse train modulation during laser percussion drilling. *Optics and Lasers in Engineering*, 35(3):149–164, 2001.

[37] M Von Allmen. Laser drilling velocity in metals. *Journal of Applied Physics*, 47(12):5460–5463, 1976.

[38] TB Thoe, DK Aspinwall, and MLH Wise. Review on ultrasonic machining. *International Journal of Machine Tools and Manufacture*, 38(4):239–255, 1998.

[39] YS Liao, YC Chen, and HM Lin. Feasibility study of the ultrasonic vibration assisted drilling of inconel superalloy. *International Journal of Machine Tools and Manufacture*, 47(12):1988–1996, 2007.

[40] Ming Zhou, XJ Wang, BKA Ngoi, and JGK Gan. Brittle–ductile transition in the diamond cutting of glasses with the aid of ultrasonic vibration. *Journal of Materials Processing Technology*, 121(2):243–251, 2002.

[41] Rupinder Singh and JS Khamba. Ultrasonic machining of titanium and its alloys: A review. *Journal of Materials Processing Technology*, 173(2):125–135, 2006.

[42] Chandra Nath and M Rahman. Effect of machining parameters in ultrasonic vibration cutting. *International Journal of Machine Tools and Manufacture*, 48(9):965–974, 2008.

[43] SH Yeo and LK Tan. Effects of ultrasonic vibrations in micro electro-discharge machining of microholes. *Journal of Micromechanics and Microengineering*, 9(4):345, 1999.

[44] B Azarhoushang and J Akbari. Ultrasonic-assisted drilling of inconel 738-lc. *International Journal of Machine Tools and Manufacture*, 47(7):1027–1033, 2007.

[45] Xiaogang Jian, T_T Meek, and Q Han. Refinement of eutectic silicon phase of aluminum a356 alloy using high-intensity ultrasonic vibration. *Scripta Materialia*, 54(5):893–896, 2006.

[46] Wilfried Kurz, C Bezencon, and M Gäumann. Columnar to equiaxed transition in solidification processing. *Science and technology of advanced materials*, 2(1):185–191, 2001.

[47] Yan Cui, CL Xu, and Qingyou Han. Effect of ultrasonic vibration on unmixed zone formation. *Scripta Materialia*, 55(11):975–978, 2006.

[48] Yan Cui, Cailu Xu, and Qingyou Han. Microstructure improvement in weld metal using ultrasonic vibrations. *Advanced Engineering Materials*, 9(3):161–163, 2007.

[49] HY Zheng and H Huang. Ultrasonic vibration-assisted femtosecond laser machining of microholes. *Journal of Micromechanics and Microengineering*, 17(8):N58, 2007.

[50] Chi-Cheng Chiu, Chih-Hao Chang, and Yung-Chun Lee. Ultrasound assisted laser machining and surface cleaning. In *Nano/Micro Engineered and Molecular Systems (NEMS), 2010 5th IEEE International Conference on*, pages 872–875. IEEE, 2010.

[51] WS Lau, TM Yue, and M Wang. Ultrasonic-aided laser drilling of aluminium-based metal matrix composites. *CIRP Annals-Manufacturing Technology*, 43(1):177–180, 1994.

[52] TM Yue, TW Chan, HC Man, and WS Lau. Analysis of ultrasonic-aided laser drilling using finite element method. *CIRP Annals-Manufacturing Technology*, 45(1):169–172, 1996.

[53] Bongchul Kang, Gun Woo Kim, Minyang Yang, Sung-Hak Cho, and Jong-Kweon Park. A study on the effect of ultrasonic vibration in nanosecond laser machining. *Optics and lasers in engineering*, 50(12):1817–1822, 2012.

[54] Shinfuku Nomura and Masafumi Nakagawa. Ultrasonic enhancement of heat transfer on narrow surface. *Heat Transfer-Japanese Research;(United States)*, 22(6), 1994.

[55] Sau Wai Wong and WY Chon. Effects of ultrasonic vibrations on heat transfer to liquids by natural convection and by boiling. *AIChE Journal*, 15(2):281–288, 1969.

[56] Harold V Fairbanks. Influence of ultrasound upon heat transfer systems. In *1979 Ultrasonics Symposium*, pages 384–387. IEEE, 1979.

[57] Mathieu Legay, Nicolas Gondrexon, Stéphane Le Person, Primius Boldo, and André Bontemps. Enhancement of heat transfer by ultrasound: review and recent advances. *International Journal of Chemical Engineering*, 2011, 2011.

[58] Lore Thijs, Frederik Verhaeghe, Tom Craeghs, Jan Van Humbeeck, and Jean-Pierre Kruth. A study of the microstructural evolution during selective laser melting of ti–6al–4v. *Acta Materialia*, 58(9):3303–3312, 2010.

[59] M Vedani. Microstructural evolution of tool steels after nd-yag laser repair welding. *Journal of materials science*, 39(1):241–249, 2004.

[60] Byoung-Gook Loh, Sinjae Hyun, Paul I Ro, and Clement Kleinstreuer. Acoustic streaming induced by ultrasonic flexural vibrations and associated enhancement of convective heat transfer. *The Journal of the Acoustical Society of America*, 111(2):875–883, 2002.

[61] M Gäumann, S Henry, F Cleton, J-D Wagniere, and W Kurz. Epitaxial laser metal forming: analysis of microstructure formation. *Materials Science and Engineering: A*, 271(1):232–241, 1999.

[62] U Kamachi Mudali and RK Dayal. Improving intergranular corrosion resistance of sensitized type 316 austenitic stainless steel by laser surface melting. *Journal of Materials Engineering and Performance*, 1(3):341–345, 1992.

[63] C Carboni, P Peyre, G Beranger, and C Lemaitre. Influence of high power diode laser surface melting on the pitting corrosion resistance of type 316l stainless steel. *Journal of materials science*, 37(17):3715–3723, 2002.

[64] RF Wood and GE Giles. Macroscopic theory of pulsed-laser annealing. i. thermal transport and melting. *Physical Review B*, 23(6):2923, 1981.

[65] Pablo Solana and Guillermo Negro. A study of the effect of multiple reflections on the shape of the keyhole in the laser processing of materials. *Journal of Physics D: Applied Physics*, 30(23):3216, 1997.

[66] Chunlei Zhang, Minsherq Wu, and Jinglei Du. Improving weld quality by arc-excited ultrasonic treatment. *Tsinghua Science and Technology*, 6(5):475–478, 2001.

[67] JA Spittle. Columnar to equiaxed grain transition in as solidified alloys. *International Materials Reviews*, 51(4):247–269, 2006.

[68] Balasubrahmanyam Avvaru, Mohan N Patil, Parag R Gogate, and Aniruddha B Pandit. Ultrasonic atomization: effect of liquid phase properties. *Ultrasonics*, 44(2):146–158, 2006.

[69] R Rajan and AB Pandit. Correlations to predict droplet size in ultrasonic atomisation. *Ultrasonics*, 39(4):235–255, 2001.

[70] RodolfoD Morales, Simon Lopez-Ramirez, Jorge Palafox-Ramos, and Donald Zacharias. Numerical and modeling analysis of fluid flow and heat transfer of liquid steel in a tundish with different flow control devices. *ISIJ international*, 39(5):455–462, 1999.

[71] S Ozawa, S Takahashi, H Fukuyama, and M Watanabe. Temperature dependence of surface tension of molten iron under reducing gas atmosphere. In *Journal of Physics: Conference Series*, volume 327, page 012020. IOP Publishing, 2011.

[72] Kiran A Ramisetty, Aniruddha B Pandit, and Parag R Gogate. Investigations into ultrasound induced atomization. *Ultrasonics sonochemistry*, 20(1):254–264, 2013.

[73] JCJ Verhoeven, JKM Jansen, RMM Mattheij, and WR Smith. Modelling laser induced melting. *Mathematical and computer modelling*, 37(3-4):419–437, 2003.

[74] Vladimir Semak and Akira Matsunawa. The role of recoil pressure in energy balance during laser materials processing. *Journal of physics D: Applied physics*, 30(18):2541, 1997.

[75] P French, M Naeem, and K Watkins. Laser percussion drilling of aerospace material using a 10 kw peak power laser using a 400 μm optical fibre delivery system. *ICALEO 2003 proceedings, Jacksonville. LIA, Orlando, paper*, 503, 2003.

[76] Yuwen Zhang and A Faghri. Vaporization, melting and heat conduction in the laser drilling process. *International journal of heat and mass transfer*, 42(10):1775–1790, 1999.

[77] RE Wagner. Laser drilling mechanics. *Journal of Applied Physics*, 45(10):4631–4637, 1974.

[78] John Ion. *Laser processing of engineering materials: principles, procedure and industrial application*. Butterworth-Heinemann, 2005.

[79] S Habib Alavi and Sandip P Harimkar. Melt expulsion during ultrasonic vibration-assisted laser surface processing of austenitic stainless steel. *Ultrasonics*, 59:21–30, 2015.

[80] S Habib Alavi and Sandip P Harimkar. Ultrasonic vibration-assisted continuous wave laser surface drilling of materials. *Manufacturing Letters*, 4:1–5, 2015.

[81] Sven-Olov Roos. Laser drilling with different pulse shapes. *Journal of Applied Physics*, 51(9):5061–5063, 1980.

[82] VP Bobkov, LR Fokin, EE Petrov, VV Popov, VN Rumiantsev, and AI Savvatimsky. Thermophysical properties of materials for nuclear engineering: A tutorial and collection of data. *IAEA, Vienna*, 2008.

[83] Dean Deng and Hidekazu Murakawa. Numerical simulation of temperature field and residual stress in multi-pass welds in stainless steel pipe and comparison with experimental measurements. *Computational materials science*, 37(3):269–277, 2006.

[84] AJ Pinkerton and L Li. An analytical model of energy distribution in laser direct metal deposition. *Proceedings of the Institution of Mechanical Engineers, Part B: Journal of Engineering Manufacture*, 218(4):363–374, 2004.

[85] Tarak Amine, Joseph W Newkirk, and Frank Liou. An investigation of the effect of direct metal deposition parameters on the characteristics of the deposited layers. *Case Studies in Thermal Engineering*, 3:21–34, 2014.

[86] Hitesh D Vora and Narendra B Dahotre. Surface topography in three-dimensional laser machining of structural alumina. *Journal of Manufacturing Processes*, 19:49–58, 2015.

[87] J Mazumder and WM Steen. Heat transfer model for cw laser material processing. *Journal of Applied Physics*, 51(2):941–947, 1980.

[88] L Romoli, F Fischer, and R Kling. A study on uv laser drilling of peek reinforced with carbon fibers. *Optics and lasers in Engineering*, 50(3):449–457, 2012.

[89] Sandip P Harimkar and Narendra B Dahotre. Crystallographic and morphological textures in laser surface modified alumina ceramic. *Journal of applied physics*, 100(2):024901, 2006.

[90] Sanjay Mishra and Vinod Yadava. Modeling and optimization of laser beam percussion drilling of nickel-based superalloy sheet using nd: Yag laser. *Optics and Lasers in Engineering*, 51(6):681–695, 2013.

[91] Rupesh Goyal and Avanish Kumar Dubey. Quality improvement by parameter optimization in laser trepan drilling of superalloy sheet. *Materials and Manufacturing Processes*, 29(11-12):1410–1416, 2014.

[92] P Forget, M Jeandin, P Lechervy, and D Varela. Laser-drilling application to a ceramic-coated alloy. *Material And Manufacturing Process*, 4(2):263–272, 1989.

[93] Sandip P Harimkar, Anoop N Samant, and Narendra B Dahotre. Temporally evolved recoil pressure driven melt infiltration during laser surface modifications of porous alumina ceramic. *Journal of Applied Physics*, 101(5):054911, 2007.

[94] Yiming Zhang, Zhonghua Shen, and Xiaowu Ni. Modeling and simulation on long pulse laser drilling processing. *International Journal of Heat and Mass Transfer*, 73:429–437, 2014.

[95] S Basu and T DebRoy. Liquid metal expulsion during laser irradiation. *Journal of applied physics*, 72(8):3317–3322, 1992.

[96] Sanjay Mishra and Vinod Yadava. Prediction of hole characteristics and hole productivity during pulsed nd: Yag laser beam percussion drilling. *Proceedings of the Institution of Mechanical Engineers, Part B: Journal of Engineering Manufacture*, 227(4):494–507, 2013.

[97] Hongyu Zhang, Jianke Di, Ming Zhou, Yu Yan, and Rong Wang. An investigation on the hole quality during picosecond laser helical drilling of stainless steel 304. *Applied Physics A*, 119(2):745–752, 2015.

[98] BS Yilbas, R Davies, and Z Yilbas. Laser alloying of metal surfaces by injecting titanium carbide powders. *International Journal of Machine Tools and Manufacture*, 29(4):499–503, 1989.

[99] J Dutta Majumdar, R Galun, BL Mordike, and I Manna. Effect of laser surface melting on corrosion and wear resistance of a commercial magnesium alloy. *Materials Science and Engineering: A*, 361(1):119–129, 2003.

[100] Kevin J Major, Catalin M Florea, Menelaos K Poutous, Lynda E Busse, Jasbinder S Sanghera, and Ishwar D Aggarwal. Surface transmission enhancement of zns via continuous-wave laser microstructuring. In *SPIE LASE*, pages 896810–896810. International Society for Optics and Photonics, 2014.

[101] S Habib Alavi and Sandip P Harimkar. Evolution of geometric and quality features during ultrasonic vibration-assisted continuous wave laser surface drilling. *Journal of Materials Processing Technology*, 232:52–62, 2016.

[102] JL Barreda, F Santamarıa, X Azpiroz, AM Irisarri, and JM Varona. Electron beam welded high thickness ti6al4v plates using filler metal of similar and different composition to the base plate. *Vacuum*, 62(2):143–150, 2001.

[103] Christoph Leyens and Manfred Peters. *Titanium and titanium alloys: fundamentals and applications*. John Wiley & Sons, 2003.

[104] J Pan, C Leygraf, D Thierry, and AM Ektessabi. Corrosion resistance for biomaterial applications of tio 2 films deposited on titanium and stainless steel by ion-beam-assisted sputtering. *Journal of biomedical materials research*, 35(3):309–318, 1997.

[105] CC Liu, CL Ou, and RK Shiue. The microstructural observation and wettability study of brazing ti-6al-4v and 304 stainless steel using three braze alloys. *Journal of materials science*, 37(11):2225–2235, 2002.

[106] Rupesh Goyal and Avanish Kumar Dubey. Hybrid approach for modeling and optimization of hole taper during laser trepan drilling of ti-6al-4v alloy sheet. *Procedia Materials Science*, 5:1781–1790, 2014.

[107] Mitsuo Niinomi. Mechanical properties of biomedical titanium alloys. *Materials Science and Engineering: A*, 243(1):231–236, 1998.

[108] Rupesh Goyal and Avanish Dubey. Modeling and optimization of geometrical characteristics in laser trepan drilling of titanium alloy. *Journal of Mechanical Science & Technology*, 30(3), 2016.

[109] R Rai, JW Elmer, TA Palmer, and T DebRoy. Heat transfer and fluid flow during keyhole mode laser welding of tantalum, ti–6al–4v, 304l stainless steel and vanadium. *Journal of physics D: Applied physics*, 40(18):5753, 2007.

[110] Simon SF Chang and Gary M Bone. Thrust force model for vibration-assisted drilling of aluminum 6061-t6. *International Journal of Machine Tools and Manufacture*, 49(14):1070–1076, 2009.

[111] Simon SF Chang and Gary M Bone. Burr height model for vibration assisted drilling of aluminum 6061-t6. *Precision Engineering*, 34(3):369–375, 2010.

[112] J Pujana, A Rivero, A Celaya, and LN López De Lacalle. Analysis of ultrasonic-assisted drilling of ti6al4v. *International Journal of Machine Tools and Manufacture*, 49(6):500–508, 2009.

[113] L Balamuth. Ultrasonic assistance to conventional metal removal. *Ultrasonics*, 4(3):125–130, 1966.

[114] Hanbing Xu, Xiaogang Jian, Thomas T Meek, and Qingyou Han. Degassing of molten aluminum a356 alloy using ultrasonic vibration. *Materials letters*, 58(29):3669–3673, 2004.

[115] Robert J Lang. Ultrasonic atomization of liquids. *The journal of the acoustical society of America*, 34(1):6–8, 1962.

[116] S Amini and MR Amiri. Study of ultrasonic vibrations' effect on friction stir welding. *The International Journal of Advanced Manufacturing Technology*, 73(1-4):127–135, 2014.

[117] XC Liu and CS Wu. Elimination of tunnel defect in ultrasonic vibration enhanced friction stir welding. *Materials & Design*, 90:350–358, 2016.

[118] Toshimichi Moriwaki, Eiji Shamoto, and Kenji Inoue. Ultraprecision ductile cutting of glass by applying ultrasonic vibration. *CIRP annals*, 41(1):141–144, 1992.

[119] DE Brehl and TA Dow. Review of vibration-assisted machining. *Precision engineering*, 32(3):153–172, 2008.

[120] RR Dehoff and SS Babu. Characterization of interfacial microstructures in 3003 aluminum alloy blocks fabricated by ultrasonic additive manufacturing. *Acta Materialia*, 58(13):4305–4315, 2010.

[121] Fuda Ning and Weilong Cong. Microstructures and mechanical properties of fe-cr stainless steel parts fabricated by ultrasonic vibration-assisted laser engineered net shaping process. *Materials Letters*, 179:61–64, 2016.

[122] MA Kadivar, J Akbari, R Yousefi, A Rahi, and M Ghahramani Nick. Investigating the effects of vibration method on ultrasonic-assisted drilling of al/sicp

metal matrix composites. *Robotics and Computer-Integrated Manufacturing*, 30(3):344–350, 2014.

[123] Khurshid Alam, AV Mitrofanov, and Vadim V Silberschmidt. Experimental investigations of forces and torque in conventional and ultrasonically-assisted drilling of cortical bone. *Medical Engineering and Physics*, 33(2):234–239, 2011.

[124] Weilong Cong and Fuda Ning. A fundamental investigation on ultrasonic vibration-assisted laser engineered net shaping of stainless steel. *International Journal of Machine Tools and Manufacture*, 121:61–69, 2017.

[125] Sourabh Biswas, S Habib Alavi, and Sandip P Harimkar. Laser surface melting of ti–6al–4v under the influence of ultrasonic vibrations. *Materials Letters*, 159:470–473, 2015.

[126] S Habib Alavi, Cody Cowell, and Sandip P Harimkar. Experimental and finite element analysis of ultrasonic vibration- assisted continuous-wave laser surface drilling. *Materials and Manufacturing Processes*, 32(2):216–225, 2017.

[127] Ho-Young Kim, Yi Gu Kim, and Byung Ha Kang. Enhancement of natural convection and pool boiling heat transfer via ultrasonic vibration. *International Journal of Heat and Mass Transfer*, 47(12-13):2831–2840, 2004.

[128] B Vinet, J-P Garandet, B Marie, L Domergue, and B Drevet. Surface tension measurements on industrial alloys by the drop-weight method. *International journal of thermophysics*, 25(3):869–883, 2004.

[129] Dirk Herzog, Vanessa Seyda, Eric Wycisk, and Claus Emmelmann. Additive manufacturing of metals. *Acta Materialia*, 117:371–392, 2016.

[130] Alan Lawley. Preparation of metal powders. *Annual Review of Materials Science*, 8(1):49–71, 1978.

[131] Leo VM Antony and Ramana G Reddy. Processes for production of high-purity metal powders. *JOM*, 55(3):14, 2003.

[132] E.G. Lierke and G. Grießhammer. The formation of metal powders by ultrasonic atomization of molten metals. *Ultrasonics*, 5(4):224 – 228, 1967.

[133] RM Tilaki, A Iraji Zad, and SM Mahdavi. Stability, size and optical properties of silver nanoparticles prepared by laser ablation in different carrier media. *Applied Physics A: Materials Science & Processing*, 84(1):215–219, 2006.

[134] Michael N Topp. Ultrasonic atomization-a photographic study of the mechanism of disintegration. *Journal of Aerosol Science*, 4(1):17IN121–20IN725, 1973.

[135] D Sindayihebura, M Dobre, and L Bolle. Experimental study of thin liquid film ultrasonic atomization. *Proc ExHFT-97*, pages 1249–1256, 1997.

[136] CG Levi and R Mehrabian. Heat flow during rapid solidification of undercooled metal droplets. *Metallurgical Transactions A*, 13(2):221–234, 1982.

[137] Arvind Prasad, Salem Mosbah, Hani Henein, and Charles-André Gandin. A solidification model for atomization. *ISIJ international*, 49(7):992–999, 2009.

[138] PA Joly and R Mehrabian. Complex alloy powders produced by different atomization techniques: relationship between heat flow and structure. *Journal of Materials Science*, 9(9):1446–1455, 1974.

[139] GM Janowski, FS Biancaniello, and SD Ridder. Beneficial effects of nitrogen atomization on an austenitic stainless steel. *Metallurgical Transactions A*, 23(12):3263–3272, 1992.

[140] Yunzhong Liu, Zhenhua Chen, and Jian N Wang. Large undercooling, rapid solidification and nucleation mechanism in multi-stage atomization. *Science and Technology of Advanced Materials*, 2(1):181–184, 2001.

[141] Andriy Kovalchenko, Oyelayo Ajayi, Ali Erdemir, George Fenske, and Izhak Etsion. The effect of laser texturing of steel surfaces and speed-load parameters on the transition of lubrication regime from boundary to hydrodynamic. *Tribology Transactions*, 47(2):299–307, 2004.

[142] Manabu Wakuda, Yukihiko Yamauchi, Shuzo Kanzaki, and Yoshiteru Yasuda. Effect of surface texturing on friction reduction between ceramic and steel materials under lubricated sliding contact. *Wear*, 254(3):356–363, 2003.

[143] P Andersson, J Koskinen, S etc Varjus, Y Gerbig, H Haefke, S Georgiou, B Zhmud, and W Buss. Microlubrication effect by laser-textured steel surfaces. *Wear*, 262(3):369–379, 2007.

[144] BH Luo, Po Wan Shum, ZF Zhou, and KY Li. Preparation of hydrophobic surface on steel by patterning using laser ablation process. *Surface and Coatings Technology*, 204(8):1180–1185, 2010.

[145] Davi Neves, Anselmo Eduardo Diniz, and Milton Sergio Fernandes de Lima. Efficiency of the laser texturing on the adhesion of the coated twist drills. *Journal of Materials Processing Technology*, 179(1):139–145, 2006.

[146] Yong-Hoon Jeong, Won-Gi Kim, and Han-Cheol Choe. Electrochemical behavior of nano and femtosecond laser textured titanium alloy for implant surface modification. *Journal of nanoscience and nanotechnology*, 11(2):1581–1584, 2011.

[147] Yong-Hoon Jeong, Han-Cheol Choe, William A Brantley, and Ik-Bu Sohn. Hydroxyapatite thin film coatings on nanotube-formed ti–35nb–10zr alloys after femtosecond laser texturing. *Surface and Coatings Technology*, 217:13–22, 2013.

[148] Ludmila B Boinovich, Alexandre M Emelyanenko, Alexander D Modestov, Alexandr G Domantovsky, and Kirill A Emelyanenko. Synergistic effect of superhydrophobicity and oxidized layers on corrosion resistance of aluminum alloy surface textured by nanosecond laser treatment. *ACS applied materials & interfaces*, 7(34):19500–19508, 2015.

[149] A Biswas, Lin Li, TK Maity, UK Chatterjee, BL Mordike, I Manna, and J Dutta Majumdar. Laser surface treatment of ti-6al-4v for bio-implant application. *Lasers in Engineering*, 17(1-2):59–73, 2007.

[150] Anil Kurella and Narendra B Dahotre. Review paper: surface modification for bioimplants: the role of laser surface engineering. *Journal of biomaterials applications*, 20(1):5–50, 2005.

[151] Wilhelm Pfleging, Renu Kumari, Heino Besser, Tim Scharnweber, and Jyotsna Dutta Majumdar. Laser surface textured titanium alloy (ti–6al–4v): Part 1–surface characterization. *Applied Surface Science*, 355:104–111, 2015.

[152] Changsheng Dong, Yu Gu, Minlin Zhong, Lin Li, Kursad Sezer, Mingxing Ma, and Wenjin Liu. Fabrication of superhydrophobic cu surfaces with tunable regular micro and random nano-scale structures by hybrid laser texture and chemical etching. *Journal of Materials Processing Technology*, 211(7):1234–1240, 2011.

[153] P AA Khan and T Debroy. Absorption of co 2 laser beam by aisi 4340 steel. *Metallurgical and Materials Transactions B*, 16(4):853–856, 1985.

[154] M Multigner, E Frutos, José Luis González-Carrasco, José Antonio Jiménez, P Marín, and Joaquín Ibáñez. Influence of the sandblasting on the subsurface microstructure of 316lvm stainless steel: Implications on the magnetic and mechanical properties. *Materials Science and Engineering: C*, 29(4):1357–1360, 2009.

[155] TS Wang, B Lu, M Zhang, RJ Hou, and FC Zhang. Nanocrystallization and α martensite formation in the surface layer of medium-manganese austenitic wear-resistant steel caused by shot peening. *Materials Science and Engineering: A*, 458(1):249–252, 2007.

[156] Ronald Lesley Plaut, Clara Herrera, Doris Maribel Escriba, Paulo Rangel Rios, and Angelo Fernando Padilha. A short review on wrought austenitic stainless steels at high temperatures: processing, microstructure, properties and performance. *Materials Research*, 10(4):453–460, 2007.

[157] Linda Gil, Sonia Brühl, Lorena Jiménez, Ovídio Leon, Rafael Guevara, and Mariana H Staia. Corrosion performance of the plasma nitrided 316l stainless steel. *Surface and Coatings Technology*, 201(7):4424–4429, 2006.

[158] TM Yue, JK Yu, and HC Man. The effect of excimer laser surface treatment on pitting corrosion resistance of 316ls stainless steel. *Surface and Coatings Technology*, 137(1):65–71, 2001.

[159] CT Kwok, KH Lo, FT Cheng, and HC Man. Effect of processing conditions on the corrosion performance of laser surface-melted aisi 440c martensitic stainless steel. *Surface and Coatings Technology*, 166(2):221–230, 2003.

[160] Volker Uhlenwinkel, Rongxiang Meng, and Klaus Bauckhage. Investigation of heat transfer from circular cylinders in high power 10 khz and 20 khz acoustic resonant fields. *International journal of thermal sciences*, 39(8):771–779, 2000.

[161] PW Fuerschbach and GR Eisler. Effect of laser spot weld energy and duration on melting and absorption. *Science and Technology of Welding and Joining*, 7(4):241–246, 2002.

VITA

Seyyed Habib Alavi

Candidate for the Degree of

Doctor of Philosophy

Dissertation: ANALYSIS AND APPLICATIONS OF MELT EXPULSION DURING ULTRASONIC VIBRATION-ASSISTED LASER SURFACE PROCESSING

Major Field: Mechanical and Aerospace Engineering

Biographical:

Personal Data: Born in Ajabshir, Eastern Azerbayjan, Iran on April 14, 1984.

Education:

Received the B.S. degree from Imam Khomeini International University, Qazvin, Qazvin, Iran, 2006, in Materials Science and Engineering

Received the M.S. degree from University of Tehran, Tehran, Tehran, Iran, 2009, in Metallurgy and Materials Engineering

Completed the requirements for the degree of Doctor of Philosophy with a major in Mechanical and Aerospace Engineering, Oklahoma State University in May, 2018.